FAKULTÄT FÜR
ELEKTROTECHNIK UND
INFORMATIONSTECHNIK
Faculty of Electrical Engineering and Information Technology

Advanced processes for controlled transfer of metal oxide nanowires to CMOS chips

DISSERTATION

submitted in partial fulfillment of the requirements for the degree of

Doktorin der Technischen Wissenschaften

by

Mag. Florentyna Lidia Sosada-Ludwikowska

Registration Number 01576091

to the Faculty of Electrical Engineering and IT

at the TU Wien

Advisor: Ao.Univ.-Prof.Dr. DI Alois Lugstein
Second advisor: Univ.-Doz. Mag. Dr. Anton Köck

The dissertation has been reviewed by:

_____
Forename Surname

_____
Forename Surname

Vienna, 1st November, 2024

_____
Florentyna Lidia
Sosada-Ludwikowska

Declaration of Authorship

Mag. Florentyna Lidia Sosada-Ludwikowska
Vienna

I hereby declare that I have written this Doctoral Thesis independently, that I have completely specified the utilized sources and resources and that I have definitely marked all parts of the work - including tables, maps and figures - which belong to other works or to the internet, literally or extracted, by referencing the source as borrowed.

Vienna, 1st November, 2024

Florentyna Lidia
Sosada-Ludwikowska

Acknowledgements

*Nanotechnology will let us build computers
that are incredibly powerful. We'll have more
power in the volume of a sugar cube than exists
in the entire world today.*

— *Ralph Merkle*

Andrew Jones from the Institute of Solid State Chemistry at Graz University of Technology for providing the XRD measurements. Thank you for sharing your knowledge and experience with me.

Martin Sagmeister from ams AG for the support regarding APPS chips and bonding, also Karl Popovic from Joanneum Research for his support in APPS chips bonding.

Austrian Institute of Technology for the possibility to use their cleanroom facilities, especially Thomas Maier for his introduction and help in semiconductor technologies.

My partents
Withouth them my scientific adventure would not even start.

My husband
For all - "C'mon, of course you can do it!"

Contents

Abstract

In microelectronics, the main reasons for reducing macrostructures into micro- or even nanostructures are to increase economic efficiency and device performance. On the one hand, more structures integrated on a silicon wafer result in lower fabrication costs, and on the other hand, this provides the possibility to implement more functionalities into a microchip. Over the years this has resulted in highly functional and miniaturized electronic devices, which can be implemented into mobile devices such as smartphones or smart watches. Besides many fields in microelectronics, where miniaturisation was key for tremendous technological progress, one is important for this work - gas sensing devices. Today's commercially available gas sensors are rather bulky and power consuming devices that need to be significantly miniaturised to enable their implementation into mobile devices like smartphones or smart watches. Using gas sensors like consumer electronic devices would be a breakthrough for their applications in everyday life, because this would enable individual air quality monitoring or breath analysis for Smart Living, Smart Home, or Smart Health. Nanostructures, and especially one-dimensional nanowires, have many advantages for gas sensor applications. Nanowires provide a large surface-to-volume ratio and the movement of electrons is confined in two dimensions, which makes them superior nanochannels for chemoresistive gas sensors, where the interaction with gas molecules in the environment is immediately transformed in a change of the electrical resistance of the nanowires. Metal oxides are the materials of choice for this type of gas sensor due to the fact, that the electrical conduction of such a material can be relatively easily changed by surface reactions with gases. In this thesis, specific metal oxide nanowires growth methods (bottom-up) are presented, which in principle can be upscaled and used for production methods on a wafer-scale. The synthesis and integration processes of the nanowires are discussed, and transfer print methodologies are presented. In particular, the stamp/tape-based transfer process has been successfully applied to integrate the nanowires onto the silicon-based (SB) sensors, on commercial SiN-based microhotplate platform chips (APPS, from ams AG) and CMOS-integrated micro-hotplate chips (MPW4, from ams AG). This transfer method is simple, scalable, cheap, and fast, and, in principle, if the NWs are regularly arranged on the growth substrate, the arrangement would be preserved on the final substrate. Both a manual transfer as well as a machine-supported approach using a bond tester have been successfully employed for the transfer of the metal oxide nanowires on SB and APPS sensors, and on APPS and MPW4 sensors, respectively. The gas sensing characterisation of the SB, APPS, and MPW4 sensors chips towards

hydrogen sulfide, carbon monoxide, toluene, HCMix, and carbon dioxide is presented. The sensors' performance has been measured at three different humidity levels (25%, 50% and 75%) and in the operation temperature range of 250-400°C. The resistance measurements for each gas sensor have been analysed in detail, and the sensor response, response times and recovery times have been calculated and discussed. As an outlook for future R&D on nanowire-based gas sensors, possible improvements of the presented transfer technique and gas sensing materials choice are proposed.

Kurzfassung

In der Mikroelektronik sind die Hauptgründe für die Reduzierung von Makrostrukturen auf Mikro- oder sogar Nanostrukturen die Erhöhung der Wirtschaftlichkeit und der Leistungsfähigkeit der Bauelemente. Einerseits führen mehr Strukturen, die auf einem Silizium-Wafer integriert sind zu niedrigeren Herstellungskosten, andererseits bietet dies die Möglichkeit mehr Funktionalitäten in einen Mikrochip zu implementieren. Im Laufe der Jahre hat dies zu hochfunktionalen und miniaturisierten elektronischen Bauelementen geführt, die in mobilen Geräten wie Smartphones oder intelligenten Uhren eingesetzt werden können. Neben vielen anderen Bereichen der Mikroelektronik, in denen die Miniaturisierung der Grund für den enormen technologischen Fortschritt war, ist einer davon für diese Arbeit besonders wichtig - die Gassensorik. Die heute im Handel erhältlichen Gassensoren sind ziemlich groß und verbrauchen viel Strom. Sie müssen erheblich verkleinert werden, damit sie in mobilen Geräten wie Smartphones oder Smartwatches eingesetzt werden können. Wenn Gassensoren wie andere Geräte der Unterhaltungselektronik verwendet würden, wäre dies ein Durchbruch für deren Anwendungen im Alltag, da dies eine individuelle Überwachung der Luftqualität oder eine Atemanalyse für Smart Living, Smart Home oder Smart Health ermöglichen würde. Nanostrukturen, und insbesondere eindimensionale Nanodrähte, haben viele Vorteile für Gassensoranwendungen. Nanodrähte bieten ein großes Verhältnis von Oberfläche zu Volumen und die Bewegung der Elektronen ist auf eine Dimension beschränkt. Dies macht sie zu hervorragenden Nanokanälen für chemoresistive Gassensoren, bei denen die Wechselwirkung mit Gasmolekülen in der Umgebung unmittelbar in eine Änderung des elektrischen Widerstands des Nanodrahts umgesetzt wird. Metalloxide sind die Materialien der Wahl für diese Art von Gassensoren, da die elektrische Leitfähigkeit eines solchen Materials relativ leicht durch Oberflächenreaktionen mit Gasen verändert werden kann. In dieser Arbeit werden spezifische Metalloxid-Nanodraht-Wachstumsmethoden (bottom-up) vorgestellt, die prinzipiell hochskaliert und für die Produktion auf großen Substraten („wafer-scale") verwendet werden können. Die Verfahren zur Synthese und Integration der Nanodrähte wird diskutiert, und es werden Transferdruckverfahren vorgestellt. Insbesondere wurde der auf Stempeln und Klebebändern basierende Transferprozess erfolgreich angewendet, um die Nanodrähte auf Silizium-basierte (SB) Sensoren, auf kommerzielle SiN-basierten Mikroheizplatten-Chips (APPS, von ams AG) und CMOS-integrierten Mikroheizplatten-Chips (MPW4, von ams AG) zu integrieren. Diese Transfermethode ist einfach, skalierbar, kostengünstig und schnell. Wenn die Nanodrähte auf dem Wachs-

tumssubstrat regulär angeordnet sind, bleibt diese Anordnung prinzipiell auch auf dem endgültigen Substrat erhalten. Für den Transfer der Metalloxid-Nanodrähte auf SB- und APPS-Sensoren bzw. auf APPS- und MPW4-Sensoren wurden sowohl ein manueller Transfer als auch ein maschinengestützter Prozess mit einem Bondtester erfolgreich eingesetzt. Die Ergebnisse der Charakterisierung der SB-, APPS- und MPW4-Sensorchips gegen Schwefelwasserstoff, Kohlenmonoxid, Toluol, HCMix und Kohlendioxid werden vorgestellt. Die Sensoreigenschaften wurden bei drei verschiedenen Feuchtigkeitsgraden (25%, 50% und 75%) und in einem Betriebstemperaturbereich von 250-400°C gemessen. Die Widerstandsmessungen für jeden Gassensor wurden im Detail analysiert, und die Sensorreaktion sowie die Ansprech- und Erholungszeiten wurden berechnet und diskutiert. Als Ausblick auf künftige Forschungs- und Entwicklungsarbeiten zu Gassensoren auf Nanodrahtbasis werden mögliche Verbesserungen der hier präsentierten Transfermethode und der Wahl des Gassensormaterials vorgeschlagen.

Streszczenie

W dziedzinie mikroelektroniki kluczowym powodem przejścia od makro-struktur do mikro-i nanostruktur jest dążenie do zwiększenia efektywności ekonomicznej oraz poprawy wydajności urządzeń. Z jednej strony, większa liczba zintegrowanych struktur na chipie krzemowym pozwala na obniżenie kosztów produkcji, a z drugiej - otwiera możliwość wprowadzenia większej liczby funkcji w mikroczipie. W miarę upływu lat doprowadziło to do powstania wysoko funkcjonalnych i zminiaturyzowanych urządzeń elektronicznych, które można zastosować w rozwiązaniach mobilnych, takich jak smartfony czy smartwatche. Wśród różnych obszarów mikroelektroniki, w których miniaturyzacja odegrała kluczową rolę w rozwoju technologicznym, istotne dla niniejszej pracy jest zagadnienie czujników gazu. Obecnie dostępne na rynku czujniki gazu mają tendencję do bycia dużymi i energochłonnymi urządzeniami, co wymaga ich znacznej miniaturyzacji, aby mogły być z powodzeniem integrowane w urządzeniach mobilnych, takich jak smartfony i smartwatche. Integracja czujników gazu w elektronice użytkowej mogłaby zrewolucjonizować ich codzienne zastosowania, umożliwiając indywidualne monitorowanie jakości powietrza oraz analizę oddechu w kontekście Smart Living, Smart Home czy Smart Health. Nanostruktury, w szczególności jednowymiarowe nanodruty, oferują liczne korzyści w zastosowaniach czujników gazu. Nanodruty charakteryzują się dużym współczynnikiem powierzchni do objętości, co skutkuje ograniczeniem ruchu elektronów w dwóch płaszczyznach (nanokanały - nanochannels). Dzięki temu stają się one idealne dla czujników gazu opartych na chemorezystywności, w których interakcje z cząsteczkami gazu prowadzą do natychmiastowych zmian w oporze elektrycznym nanodrutów. Tlenki metali są preferowanymi materiałami dla takich czujników, ponieważ ich przewodnictwo elektryczne można relatywnie łatwo zmieniać w wyniku reakcji powierzchniowych z gazami. W tej pracy przedstawiono konkretne metody wzrostu nanodrutów z tlenków metali w procesach typu bottom-up, które można łatwo skalować do produkcji na poziomie płytek krzemowych (wafer-scale). Omówiono także procesy syntezy oraz integracji nanodrutów, a także zaprezentowano metody transferu. Szczególnie zwrócono uwagę na transfer oparty na stemplach i taśmach, który skutecznie zastosowano do integracji nanodrutów w czujnikach opartych na krzemie (SB, Silicon-Based), komercyjnych mikroheaterach opartych na SiN (APPS, ams AG) oraz mikroheaterach zintegrowanych z technologią CMOS (MPW4, ams AG). Ta metoda transferu odznacza się prostotą, skalowalnością, niskim kosztem oraz szybkością, a w przypadku regularnego rozmieszczenia nanodrutów na podłożu wzrostu, ich układ jest zachowywany na końcowym podłożu (tam, gdzie nanodruty zostały przeniesione).

5

Zarówno ręczny transfer, jak i metoda wykorzystująca urządzenie do testowania wiązań (bondtester), zostały z powodzeniem zastosowane do transferu nanodrutów różnych tlenków metali, odpowiednio na czujniki SB i APPS (transfer manualny) oraz na czujniki APPS i MPW4 (transfer poprzez bondtester). Przedstawiono właściwości czujników SB, APPS i MPW4 w zakresie wykrywania siarkowodoru, tlenku węgla, toluenu, HCMix (mieszanina węglowodorów) i dwutlenku węgla. Wydajność czujników została zmierzona przy trzech różnych poziomach wilgotności (25\%, 50\% i 75\%) oraz w zakresie temperatur pracy 250-400°C. Pomiary rezystancji dla każdego czujnika gazu zostały szczegółowo przeanalizowane, a odpowiedź czujnika, czas reakcji i czas regeneracji zostały obliczone i omówione. Jako perspektywę dla przyszłych badań nad czujnikami gazu opartymi na nanodrutach, zaproponowano możliwe ulepszenia przedstawionej techniki transferu i doboru materiałów do wykrywania gazu.

CHAPTER 1

Motivation

Sensing is the basic interaction of humans and environment. People can interact with the world with 5 senses they possess: hearing, touch, sight (physical senses), smell and taste (chemical senses). One of those chemical sensors humans have is smell - which allows not only to smell fresh air or some delicious cookies, but also can help to distinguish between fresh and rotten food, or even that the air has some dangerous component (i.e. ammonia or gasoline). There is a significantly increasing awareness in society concerning the negative impact of pollution on human health. Living healthier is a global trend, which will trigger the use of devices capable of monitoring the individual environment. Also, global environmental change is activating the development of such devices, which are capable of area-wide pollution monitoring. According to a study by Siemens AG, indoor air quality regulated HVAC building management has the potential to save ~ 25% of buildings' energy needs worldwide, and to significantly reduce CO_2 emissions. [1] Chemical sensors are key for the EU Green Deal to enable monitoring and control of air quality (AQ) to improve human health. Expected new directives (EU, WHO) on air quality for meeting the EU Zero Pollution Plan (Directive (EU) 2016/2284, target of reducing premature deaths from air pollution [2]) will trigger the need for innovative air quality monitoring devices. Chemical sensing of gas molecules is essential for monitoring air quality (indoors and outdoors), estimating environmental pollution, ensuring industrial workplace safety, and tracking fitness and health. Chemical sensing of gas molecules has become a vital necessity for ensuring high air quality both indoors as well as outdoors. Since people in Europe or US spend 90% of their time indoors, air quality monitoring is of tremendous importance for private homes, offices, vehicles and transportation. Air pollution is considered a "silent killer" (Fig. 1.1) causing an estimated 7 million premature deaths every year. [3–5]

Despite extensive efforts for decades, miniaturised gas sensors, enabling identification and quantification of a variety of different gases, remain elusive due to major cross-sensitivity

1

Figure 1.1: Air pollution is considered a "silent killer" causing an estimated 7 million premature deaths every year. Copied from: World Health Organization (who.int).

issues of conventional sensor devices. Many future environmental monitoring applications, however, will require miniaturised and inexpensive chemical sensor solutions which are capable for detection of potentially harmful gas components, such as CO, formaldehyde, or toluene, out of the environmental air. Unfortunately some harmful gases in the air are not recognizable by human nose - i.e. carbon monoxide - dangerous residue of incomplete combustion, odourless and colourless. According to statistics - in Austria almost 50% of warming energy (in terms of Gigajoules of warming energy) is produced by combustion sources (wood, oil, gas, coal) [6], where CO can be produced due to damaged installation or insufficient ventilation. Hence, detection of a variety of target gases is essential.

Most commercially available gas sensing devices are bulky and require a lot of energy. They are based on thick or thin film resistors, and have to be thermally activated

2

up to temperatures of typically 400°C or higher. Thus, such devices have to employ heating elements based on alumina substrates and Pt-coils, where the gas sensitive materials are implemented. These gas sensors exhibit high power consumption (50 mW – 100 mW or more). Due to the necessity of heating one of the ways to decrease the power consumption is miniaturisation of the device itself or/and the sensing material. Their miniaturisation could further result in the implementation of the gas sensors into mobile devices, like smartphones or smart watches, and a possibility of monitoring air quality in all rooms where those mobile devices will be present (and, most probably, their owners). Basic concept behind reducing macrostructures into micro- or even nanostructures is also economy - lower fabrication cost due to more structures on a wafer and higher functionality. [7] Although there are considerable improvements in terms of miniaturization and power consumption with thermally activated commercial devices, the commercial MOx gas sensors cannot fulfill the requirements for smart gas sensor applications: they have slow response time, high power consumption, exhibit cross sensitivities and are primarily dedicated to industrial applications. Over the past decades, many variants of electric gas sensors, which rely on changes of electrical conductance due to the surrounding gas, have been developed. Among those, conductometric sensors based on metal oxide (MOx) semiconductors such as SnO_2, ZnO, CuO, TiO_2 and WO_x are the most promising candidates for inexpensive compact implementations with industrial relevance. [8–10] Metal oxide based gas sensors can detect various gases with high sensitivity and the detection principle is simple - the resistance change is easy to measure.

Considerable progress has been made in implementing gas-sensitive materials with Complementary Metal-Oxide-Semiconductor (CMOS)-integrated micro-hotplate (µhp) devices, which allow for a lower power consumption (e.g. ~10 mW at 400°C). Here, in terms of device integration and miniaturization, we have set new standards within the FP7-Project MSP. [11, 12]

The implementation of nanomaterials, such as nanocrystalline thin films, nanowires or nanoparticles, is the most powerful strategy to improve sensor performance by maximizing the surface to volume ratio. One dimensional nanostructures have been thoroughly investigated due to their advantages such as enhanced surface-to-volume ratio and improved stability due to high crystallinity. Therefore, with respect to device stability, single crystalline nanowires are favourable. From our measurements we conclude that single crystalline SnO_2 nanowire sensors provide a higher sensing effectiveness and an improved cross-sensitivity than their nanocrystalline counterpart. [13]

Tailoring the response of MOx gas sensors by surface functionalization with metallic nanoparticles is a most promising approach to achieve a high degree of selectivity. Recently, we have demonstrated, that functionalization of SnO_2 ultrathin films with Pt-NPs significantly improves the CO-response with minimized humidity interference. [14] In general, however, low selectivity remains the biggest disadvantage also of nanomaterial-based conductometric gas sensors, because MOx materials react with multiple target gases and the resulting changes in conductivity are not specific for a certain analyte species. As a result, the sensors are not capable to clearly measure a single gas component

out of a gas mixture. A wide range of nanostructures production methods is known from literature and will be presented in this thesis - but the implementation of the nanostructures on the devices is still an issue. For gas sensing the nanostructures in wire shape are suitable due to their large surface-to-volume ratio and their structure - they are natural conduction channels and as such are a perfect choice for conductometric gas sensors. Metal oxide nanowires are widely used in gas sensing and their transfer process on actual devices mostly involves organic liquids which, from experience in our laboratory, can poison the gas sensing material and is connected with the coffee-ring effect (most nanowires are present on the edges of the droplet formed on the surface of the device). In this thesis a simple, fast, reproducible and cost-effective method of nanowires transfer was used - transfer printing. This transfer process can be performed manually (by hand) and, with more precision, by a wire bonder. Both of those methods were used in this work.

Theoretical part

2.1 Metal oxide semiconductor gas sensors

First semiconductor metal oxide reaction with gas was described by Heiland in 1954 [15], where a change of conductivity of zinc oxide in presence of hydrogen and oxygen was presented. The effect of conductivity change in presence of gas was used in a commercial device for the first time in 1971 by Taguchi [16], where an alarm was starting to ring in presence of "hydrogen, carbon monoxide, or a vapour of an organic fuel such as alcohol or gasoline or if the air becomes contaminated with smoke at a specific concentration".

The main usage of gas sensors is to monitor and notify, if necessary, about appearance of dangerous concentration of specific gases in the environment. For such responsible role as protection of human beings all gas sensors have to fulfill specific requirements, usually called the "5S rule" [17]:

- Sensitivity,

- Selectivity,

- Speed of response/recovery,

- Stability and

- Sales (cost of production, mass, power consumption).

Two of those requirements are automatically satisfied for metal oxides - sensitivity and sales. Sensitivity - due to the wide range of gas molecules which can be sensed due to adsorption and desorption processes, and sales - due to the simplicity of production and numerous available processes for metal oxide fabrication. The MOx also are stable in wide range of temperatures in presence of oxygen and other atmospheric gases [18]. Producing

metal oxide as a sensing material can be easily introduced into a production line of small devices, like Micro-Electro-Mechanical Systems (MEMS) as well as Complementary Metal-Oxide-Semiconductor (CMOS) platforms. The smaller the device is - the lower the power consumption and cost per device can be achieved. Stability and ease of production are not the only advantages of using metal oxides as gas sensing devices - the main reason of using metal oxides for environmental air monitoring is that they are conductive sensors and resistance can be measured by easy and cheap electronic circuits.

Several institutions, which provide market research, have shown that new markets of air quality monitoring in mobile devices or wearables will be extensively used in the future. One of them, IDTechEx, expect a large increase of sales in those new markets, which can be shown in Fig. 2.1. Miniaturisation is the key to achieve sensors implementable in mobile devices - and that could be achieved with CMOS integrated chemical sensors based on metal oxide nanomaterials.
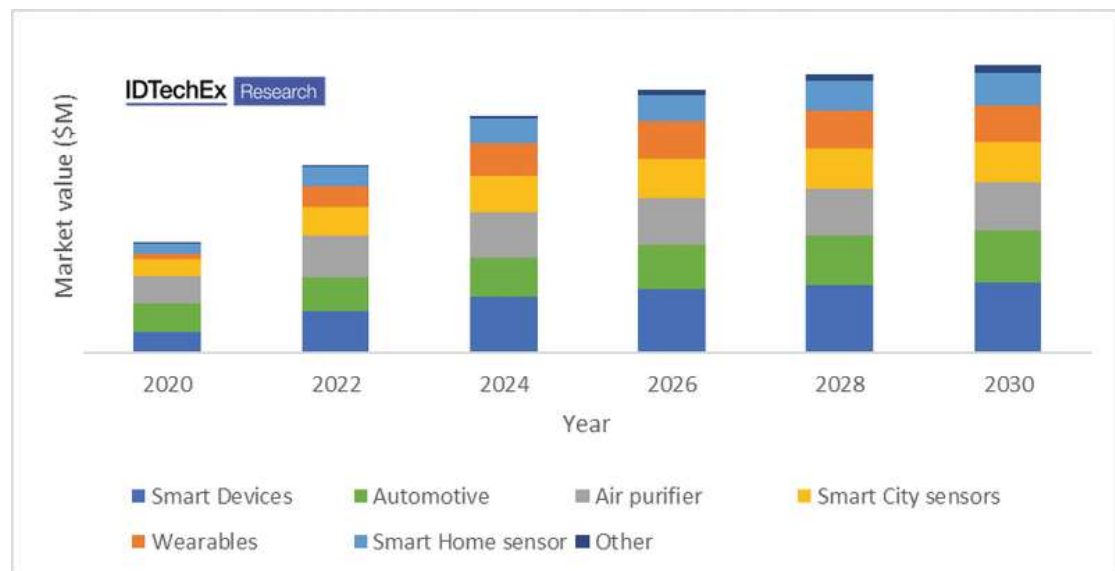

Figure 2.1: Prediction of market value of air quality monitoring devices in smart devices, automotive, air purifiers, smart city sensors, wearables, smart home sensors and other applications. (from [19]).

2.1.1 Types of gas sensors

Commercially available, low cost and portable gas sensors can be categorized in 5 types, which are listed in Tab. 2.1), including their different working principle:

1. Electrochemical sensors

2. Catalytic sensors

3. Non-dispersive infrared (NDIR) optical sensors

4. Photo-ionization based sensors and

5. Solid-state sensors (typically metal oxide based).

Table 2.1: Gas sensors - types and working principle on basis of [20][21]

Types of gas sensors	Working principle
Electrochemical (amperometric)	Gas molecules diffuse through a membrane, electrochemical reaction happens on working electrode, electrical charges flow through a wire and ions through ion conductor (solid or liquid) towards a counter electrode, electrochemical reaction occurs on the counter electrode, the induced current of a redox reaction is proportional to gas concentration [22]
Catalytic	Gas molecules burn on a detector cell (with a catalyst), resistance of detector cell increases and the current flows between detector and reference cell, current is proportional to gas concentration [23]
Non-dispersive infrared (NDIR)	Gas molecules absorb IR radiation inside a measurement chamber, intensity of the light decreases between light source and detector (Beers Law), reduction of transmittivity is proportional to gas concentration [24]
Photo-ionization	UV-light ionizes the gas molecules, then the ions are collected by electrodes and the generated current is proportional to gas concentration [25]
Solid-state (metal oxide based)	Adsorbed oxygen on MOx surface captures free electrons, gas molecules react with adsorbed oxygen and release the electrons, change of resistance is proportional to gas concentration [26]

The electro-chemical sensors has a great advantage of working in room temperature and due to that has lowest power consumption [20]. The disadvantages are i.e. short life

time (in comparison to others) and aging of the membrane causing signal deterioration with time [27]. Next type is catalytic sensor, which is used to detect combustible gases and their leaks in different applications [21], but it needs high power to heat up to 400°C- 600°C and experience poisoning and burning out of the catalyst on the detector cell [20]. Other type of gas sensing device is non-dispersive infrared (NDIR), which offer high stability, sensitivity and selectivity due to optical "fingerprints" which can be obtained for single compounds, but still suffer from high power consumption of the light sources and miniaturising path length is still a challenge [28]. Next type of gas sensor is photo-ionization type, which has very low detection limit and response time, the problems are miniaturising the ionization chamber and high power consumption due to UV lamp [29]. The last type, also used in this work, are solid-state (metal oxide based) sensors which can detect various gases; the metal oxides are stable in oxygen-containing atmosphere and have a long life time. However, stability can be an issue if polycrystalline materials are employed due to potential poisoning at the grain boundaries. Highly crystalline structures (i.e. nanowires) should be superior due to the lack of grain boundaries. Moreover, as demonstrated in [13] the nanowires should offer a higher sensing efficiency as compared to their polycrystalline thin film counterparts. The disadvantages of solid-state sensors are high power consumption due to the necessary heating of the sensitive element, long response time and lack of selectivity due to high sensitivity to large group of chemical molecules. There are many ideas how to overcome those disadvantages - for high power consumption, nanomaterials and heater miniaturisation can be implemented, nanomaterials experience also shorter response time due to shorter way for electrons. Selectivity can be achieved by optimization of sensing material with nanoparticles, doping or parallel implementation of different metal oxides into single device [30].

2.1.2   Commercially available sensors and applications

Commercial gas sensors can be divided into two groups:

1. Sensor systems, which are more bulky devices and are usually employed for professional applications. These sensor systems are more precise and are used in industry, home safety and "handy" devices - i.e. for gas leaks detection. A lot of companies are producing bulky devices, i.e. Honeywell, Dräger, Industrial Scientific, MSA Safety and Aeroqual. Some examples of such professional sensor systems are presented in Fig. 2.2.

2. Miniaturized sensor devices, which are basically forseen for consumer electronic applications, such as smartphones or smartwatches with lower power requirements. Commercial miniaturized gas sensors are produced by several companies, such as Sensirion, Figaro, E+E etc. Some examples of such miniaturized commercial sensors are presented in Fig. 2.3.

Figure 2.2: Industrial gas sensors systems. Directly copied from producent/distributors webpages: `https://www.rockallsafety.co.uk/product/honeywell-analy tics-sensepoint-xrl-fixed-gas-detector/`, `https://www.indsci.com /en/gas-detectors/single/tango-tx1`, `https://www.draeger.com/en_s eeur/Products/PointGard-3700` .
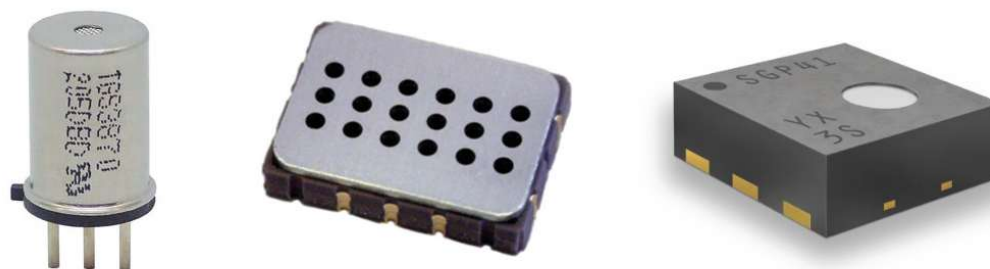
Figure 2.3: Miniaturized commercial gas sensors. Directly copied from producent/distributors webpages: `https://www.figarosensor.com/product/e ntry/tgs3870.html`, `www.sgxsensortech.com/sensor/mics-5524`, `https://www.sensirion.com/products/catalog/SGP41` .

In this work the focus is on miniaturised devices - and there are a few examples of those in Tab. 2.2. The list consists carbon monoxide miniaturised gas sensors and VOC (volatile organic compounds) sensors. The VOC gases are hard to define and almost every company uses its own list of substances for checking the VOC presence, but the EU Commision definition is "any organic compound as well as the fraction of creosote, having at 293,15 K a vapour pressure of 0,01 kPa or more, or having a corresponding volatility under the particular conditions of use", and VOC gases are classified as air pollutants. [31]

9

Table 2.2: Commercial miniaturized gas sensors.

Sensor name	Type of sensor	Size	Source
CARBON MONOXIDE			
DD-Scientific P/N: S+4 2ECO	electrochemical	20x20x16.5mm	[32]
Alphasense AP-0005	electrochemical	25x40x29mm	[33]
SPEC Sensors UL 2034	electrochemical	15x15x3mm	[34]
Figaro TGS5141-P00	electrochemical	14.6x13.9x6.8mm	[35]
CO 500 Satellix	electrochemical	Ø18.1x42mm	[36]
Draeger XXS Sensors, H2S-LC/CO-LC Dual Sensor	electrochemical	not available	[37]
Aeroqual SH CO	MOS	not available	[38]
Figaro TGS3870	MOS	9.2x9.2x18mm	[39]
Zhengzhou Winsen Electronics Technology Co., LTD MQ-7B	MOS	21.4x21.4x31mm	[40]
Alphasense CO-D4X	MOS	Ø14.5x12.3mm	[41]
Winsen MC227D	catalytic	Ø12x15mm	[42]
Euro Gasman B-1	non-dispersive infrared (NDIR)	306x48x43mm	[43]
VOLATILE ORGANIC COMPOUNDS			
iAQ-2000 AppliedSensor	MOS	29x56x14mm	[44]
ams AG AS-MLV-P2	MOS	Ø9.1x4.53mm	[45]
CCS801 Cambridge CMOS Sensors	MOS	3x2x1mm	[46]
SGX Sensortech MiCS-5524	MOS	5x7x1.55mm	[47]
piD-TECH VOC-TRAQ II	photoionization	20.4x17.6x4.78mm	[48]
PID-AR Alphasense	photoionization	Ø20.4x22.38mm	[49]
VOC-A4 Alphasense	electrochemical	Ø20x20.8mm	[50]
VOC-P31 Alphasense	MOS	Ø218x16.6mm	[51]
4R-PID Winsen	photoionization	Ø20.4x21.1mm	[52]
TGS2620 Figaro	MOS	Ø9.2x17.8mm	[53]
GGS 10530 T Umweltsensortechnik	MOS	Ø8.1x22.6mm	[54]
VOC Gas Sensor VM-1001	MOS	not available	[55]
SENS-IT UNITEC	electrochemical	not available	[56]
P/N 707 Synkera	MOS	Ø3.8x5.9mm	[57]

Once performance of the chemical sensors reaches a satisfactory level, they will serve as catalysts for a wide range of applications, resulting in significant positive transformations for our economy, environment, and society. Chemical sensors open a huge variety of applications, which improve our lives, address global challenges (e.g., greenhouse gases), create new market opportunities for European players, and, thus, have significant societal and economic impact:

- Smart Home & Smart Living: chemical sensors might be implemented in a smart phone or as a separate device for individual monitoring of environmental conditions, for detection of potentially harmful situations, and for alerting people with health predisposition of upcoming dangerous environmental conditions (specific target gases as listed in Tab. 2.3). Monitoring the exposure to harmful air polluting gases is presently beyond the control of individuals. A reliable, miniaturized device would enable air quality monitoring in private homes, office buildings, hospitals or vehicle/airplane cabins.

- Environmental monitoring: chemical sensors can be employed for setting up IoT-capable sensor networks for area-wide real-time monitoring of air pollutants (NO_x, CO, CO_2, O_3 etc.) and greenhouse gas emissions. Such a sensor network would provide real-time pollution information for individuals e.g. on a smart phone and would enable individuals to set precautions in case of high ozone concentrations (e.g. no jogging, staying inside).

- Smart Health & Smart Medicine: chemical sensors would generate a tremendous impact for medicine and health by analysing the exhaled breath and identifying bio markers (specific target gases as listed in Tab. 2.3) for screening of potential upcoming diseases (e.g. lung infections). Breath analysis will enable monitoring of patients with chronical illness (e.g. diabetes, chronic obstructive pulmonary disease) and will assist medical doctors in patient treatment. Application in smart phones could support individual training and fitness monitoring.

- Agriculture and Food: chemical sensors device would generate an impact in food production. The device can be employed for monitoring gas conditions in green houses and for optimizing the growth conditions and the crop yield. The device can be used for monitoring the freshness of fruits and taking preventive actions when conditions potentially endanger crops.

All these potential applications have positive impact on human health, the Green Deal, sustainable production, economy, and ecology. As result, miniaturized gas sensors have a substantial importance for European citizens and industry.

Table 2.3: Target gases, their concentration requirements, state-of-the-art sensors and their future applications. [3, 58, 59]

Target gases	Concentration requirement	State-of-the-Art sensors	Application
Carbon dioxide (CO_2)	< 1000 ppm (OEL)	400-2000 ppm	Smart Home & Smart Living
Carbon monoxide (CO)	< 30 ppm (OEL)	100 ppb - 10 ppm	
Ammonia (NH_3)	< 20 ppm (OEL)	no	Environmental Monitoring
Nitric dioxide (NO_2)	< 5 ppb (WHO)	no	
Ozone (O_3)	< 30 ppb (WHO)	no	OEL - Occupational Exposure Level
Benzene (C_6H_6)	< 1 ppb (WHO)	no	PEL - Permissible Exposure Level
Formaldehyde (HCHO)	< 81 ppb (WHO)	50 ppb - 1 ppm	
Acetone (($CH_3)_2CO$)	200 ppb - 1 ppm [60]	no	Smart Health & Smart Medicine
Isoprene ($CH_2 = C(CH3) - CH = CH_2$)	50 ppb - 1 ppm [61]	no	
Acetaldehyde (CH_3CHO)	10 ppb - 10 ppm [62]	no	Training & Fitness
Butyric acid ($CH_3CH_2CH_2COOH$)	5 ppb - 100 ppb	no	
Dimethylsulfide (($CH_3)_2S$)	5 ppb - 100 ppb	no	State-of-the-Art sensors*: conductometric, photoacoustic, electrolyte, optical NDIR, and thermal conductivity based sensors from market leaders BoschSensorTec, Sensirion, Alphasense, Figaro, and TDK
Ethanol (C_2H_5OH)	10 ppb - 100 ppm	500 ppb - 10 ppm	
Pentane (C_5H_{12})	10 ppb - 50 ppb	no	
Toluene ($C_6H_5CH_3$)	5 ppb - 250 ppb	no	
Butane (C_4H_{10})	1 ppb - 50 ppb	no	

The above-mentioned applications require reliable detection of a variety of target gases. Table 2.3 list target gases which are relevant for AQ monitoring indoors and outdoors according to recommendations of WHO. The target gases for Clinic and Home Care, and Metabolic and Fitness – also referred to as biomarkers – are those who are characteristic for upcoming diseases etc. The column State-of-the Art sensors shows that available sensors are not capable for measuring those gases. The commercially available sensor devices are not there yet to fulfill the requirements of many applications. This is also obvious from Table 2.4, which lists the most advanced and miniaturized chemical sensors based on conductometric, photoacoustic, electrolyte, optical NDIR, and thermal conductivity-based gas sensors. Hence, there is still a long way to go until the sensors can detect all required target gases.

Table 2.4: Comparison of different commercial gas sensors.

	Bosch BME 680	Sensirion SFA30	Sensirion SCD42	Alphasense	Sensirion SCD30	TDK ICE 11101
Detection principle	Conductometric	Conductometric	Photoacoustic	Electrolyte	Optical NDIR	Thermal conductivity
Size [mm x mm x mm]	3 x 3 x 1	17 x 17 x 1,5	10 x 10 x 6.5	32,3 x 32,3 x 16,5	37 x 15 x 7	5 x 5 x 1.1
Power consumption [mW]	11.9	10	50	not specified	9,5	53
Response time [sec]	not specified	120	60	30	20	60
TARGET GASES:						
"Air contaminants"	no	no	no	no	no	0-30 ppm
VOCs / Ethanol	only quality	no	no	no	no	no
CO_2	no	no	400-2000 ppm	no	400-10000 ppm	400-5000 ppm
NO_x	no	no	no	no	no	no
Formaldehyde	no	0-1000 ppb	no	no	no	no
CO	no	no	no	100 ppb - 10 ppm	no	no
NO_x, benzene, toluene, ammonia, ozone, SO_2, H_2S	no	no	no	no	no	no

2.1.3 Conduction model of chemoresistive gas sensor - grain model, multi-NW model

The simplest description of the chemoresistive reaction is that a gas molecule (e.g. CO) is chemically reacting with surface atoms of the gas sensitive film (e.g. O_2 on a metal oxide). Electrons are either transferred from the gas molecule to the sensing films or inverse. For the case of CO and SnO_2, an electron is transferred from the CO molecule (or, to be more precise, from the pre-adsorbed oxygen ion that is reacting with the CO) to the SnO_2 film. For the case of NO_2 and SnO_2, an electron is transferred from the SnO_2 film to the NO_2 molecule. Hence, in both cases, the number of the electrons in the sensing film is changed and can then be detected by measuring the electrical resistance change.

In free space electrons can propagate freely and their energy can be expressed as:

$$E = \frac{\hbar \mathbf{k^2}}{2m} \tag{2.1}$$

In the crystal lattice though the electrons are disturbed by atoms inside the crystals, and the perturbation can be described by a periodic potential (nearly-free electron approximation by Peierls). Due to the wave character of electrons this periodic potential causes a Bragg reflection close to Brillouin zone boundaries and forms forbidden energy gaps. [63] Those forbidden energy gaps form band gaps (band structure), which are different for different materials - conductors, semiconductors or insulators. The main difference between the different types can be described in terms of electronic states occupation. For conductors the energy bands are partly filled with electrons (the conduction and valence bands overlap) and due to that electronic states can be occupied and material can be conductive (see Fig. 2.4a - band structure for gold, no band gap). For insulators the energy bands are completely filled and due to that change of velocities of those electrons cannot be changed - which implies no conductivity (see Fig. 2.4c - band structure for silicon oxide, large band gap). For semiconductors the empty bands (conduction band) are close to the top of filled energy bands (valence band) and the electrons can be transferred there with i.e. thermal excitation - after the excitation the material can be conductive (see Fig. 2.4b - band structure for tin oxide, the band gap is in the range of violet/UV).

Semiconducting metal oxides are the basic materials used for chemoresistive gas sensors due to the fact, that the conduction of such a material can be changed relatively easily by outer conditions, i.e. radiation, temperature or surface reactions. Semiconducting metal oxides are the material of choice for this type of sensors due to their high stability and high sensitivity towards gas molecules. [64] This high sensitivity can be explained by the grain structure and, due to that, high surface-to-volume ratio. The high surface-to-volume ratio can be also achieved by implementing nanostructured metal oxides, such as nanowires and nanoparticles. Historically, the first metal oxide gas sensors were grainy films of metal oxides; the working mechanism of such structures is explained as follows.
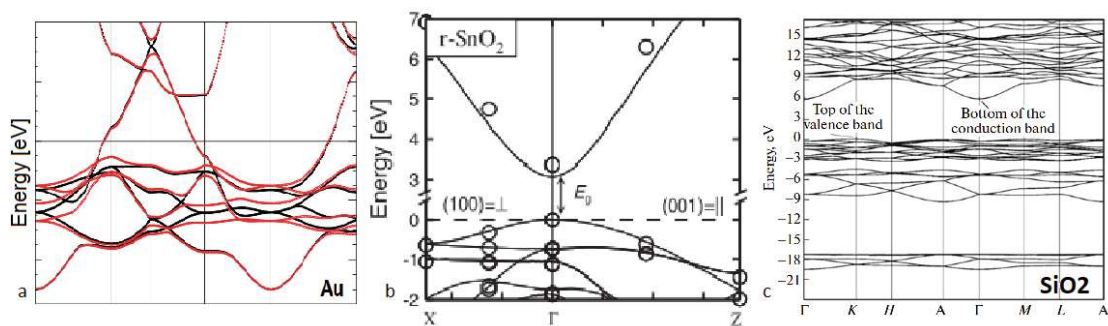
Figure 2.4: Band structures of: insulator (silicon dioxide) [19], semiconductor (tin dioxide) [65], and metal (gold) [19].

Grain model

The electrical properties of granular semiconductors can change dramatically due to the high surface-to-volume ratio and the chemical and physical reactions occuring on the surface and interfaces of the grains. The surface electronic states can be divided into two groups - intrinsic surface states and extrinsic surface states [66, 67]:

- Intrinsic surface states are connected to the relaxation or reconstruction of the surface itself - due to the lack of atomic bonds above the surface.

- Extrinsic surface states are related to defects in the crystal lattice (i.e. missing atom) or adsorption of molecules on the surface. [67]

Adsorption of charged molecules leads to confining electrons at the surface, which results in band bending and change of resistivity of the whole semiconductor. [64] In case of numerous reactions with gas molecules on the surface, this change in resistivity will be detectable as direct electrical signal by a simple resistance measurement. These measurements are performed in environmental conditions (ambient air) - which means that oxygen molecules are present. The oxygen molecules can be adsorbed on the surface of the gas sensitive semiconductor and form – depending on the temperature of the surface - different oxygen ion species, which are crucial for the further reactions with other gases (e.g. CO). [68] Fig. 2.5 shows that below 150°C the molecular-ionic species (O_2^-) dominate on the surface, above 150°C - atomic-ionic species (O^-).

As already mentioned - adsorption of oxygen on the surface leads to extraction of negatively charged electrons from the conduction band (for an n-type semiconductor, such as SnO_2). As shown in Fig. 2.6, this charge movement leads to band bending and the formation of a depletion region near to the surface. The ionized donor states
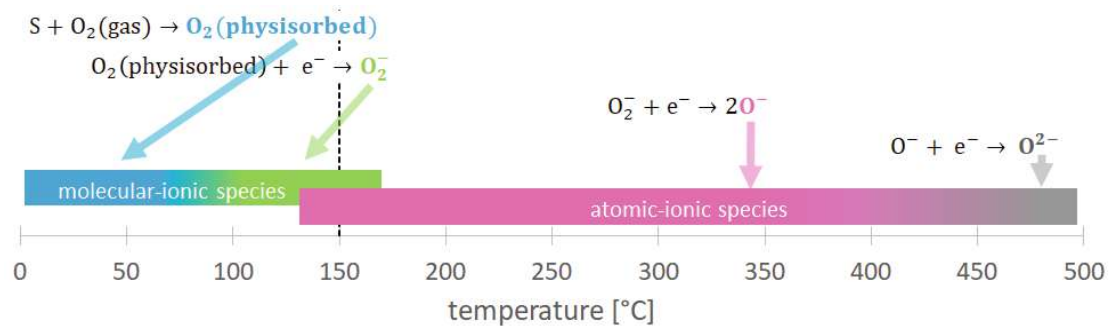
15

Figure 2.5: Oxygen ion species adsorbed on the surface of the semiconductor (here - tin dioxide, data from [68]) - temperature dependence.

are created after "donating" electrons to the acceptor states of the ionosorbed oxygen molecule on the surface. [69] The band bending can be described by the potential barrier V_s and the thickness of the depletion region z_0. Those two parameters are connected to the changes of conductance of the gas sensing material. The height of the potential barrier has a direct influence on the conductance due to the number of electrons trapped on the surface states. The resulting conductance can be described as follows:

$$G = G_0 \exp\left(\frac{-eV_s}{kT}\right) \tag{2.2}$$

where G_0 is the electrical conductance before absorption of oxygen, k_B - Boltzmann constant and T - temperature [70].
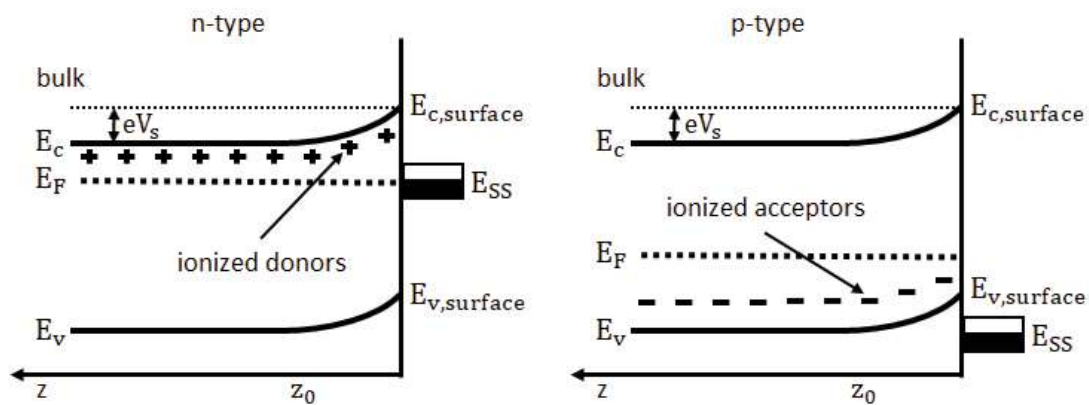

Figure 2.6: Band bending formed by ionosorption of oxygen on the surface of n-type (left) [64, 68, 69] and p-type (right) [71] semiconductor .

16

The width z_0 of the depletion region has a strong influence on the conductance due to the gas sensitive material properties - if the granular semiconductor has large or small grains (see Fig. 2.7). The grains are called "large" if their size is larger than the Debye length λ_D of the gas sensing material. In this case, Debye length means the penetration depth of the field into the material, which depends on temperature and density of donors/acceptors. Accordingly - small grains are "small" if their diameter is smaller than the Debye length. The Debye length can be described as follows:

$$\lambda_D = \sqrt{\frac{\varepsilon kT}{q^2 n_c}} \tag{2.3}$$

where ε is the static dielectric constant, k_B - the Boltzmann constant, T - the temperature in K, q - the electrical charge, and n_c - the carrier concentration. [72]

For large grains the conduction is influenced not only by the difference between the surface and the bulk conduction (depletion layer), but also by grain boundaries. [68] Between grains, the electrons have to overcome an energy barrier to move from one grain to the other. This barrier has a different height for different oxygen accumulation levels on the surface (see Fig. 2.7 upper part). For small grains the conductance is mostly influenced by the surface states. The depletion regions start to overlap and the difference between "surface" and "bulk" disappears. The overlapping leads to the overlap of the energy barriers and thus the bands are flat-like (see Fig. 2.7 lower part). [73]
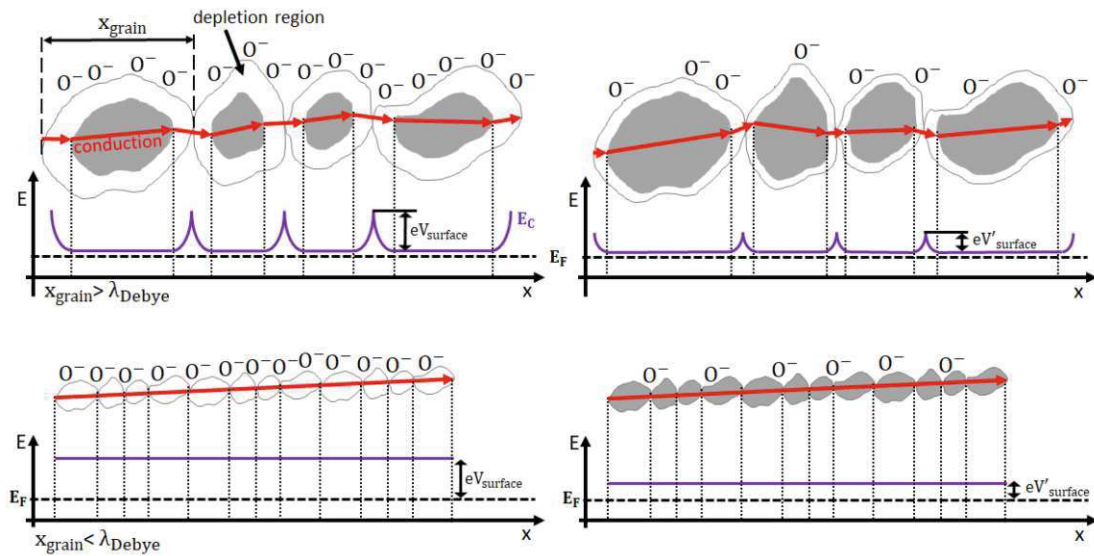

Figure 2.7: Conduction through large grains (upper part) and small grains (lower part) in an n-type semiconductor. Also, different oxygen adsorption coverage is shown (left and right). [64, 68, 73]

17

All the above analysis is valid for an n-type semiconductor.

For the p-type semiconducting metal oxide, the adsorption of oxygen from the ambient air also leads to the band bending - but here the electrons are extracted from the valence band. In contrast to the depletion layer of an n-type semiconductor, the oxygen adsorption leads to the accumulation of holes (major carriers in a p-type semiconductor) near to the surface - a so called accumulation layer. [71] Both types of semiconductors can be described by a kind of "core-shell" structures: for an n-type semiconductor the conductance path goes through the cores, while for the p-type semiconductor the conductance path goes through the shells due to the high concentration of carriers (holes). [74] For the granular semiconductors there is a significant technological problem - there is no possibility to precisely control the size of the intergranular regions (so called "necks" of conduction). [69] Therefore the crystalline nanostructures (nanoparticles, nanowires or nanosheets) may offer better control over their dimensions and hence the electrical properties of the material. In the next chapter, the model of multi-nanowire gas sensor is discussed. [75]

Multi-nanowire model

Nanotechnology allows to create enormous number of various nanostructures - quantum dots, nanowires, nanobelts, nanotubes etc. Especially metal oxide nanowires are interesting for gas sensing applications due to their high surface-to-volume ratio and high stability due to their high crystallinity. [76] A big advantage of single-crystalline nanowires is the absence of grain boundaries: sensor poisoning by elements such as sulfur, usually occurs due to diffusion of molecules along grain boundaries into the material. Multi-nanowire devices consist of a network of aligned or randomly distributed nanowires. The oxygen adsorbs on the surface of those nanowires and creates, similarly to the grains, a core-shell structure with a depleted shell and a conductive core (see Chapter 2.1.3). Due to the fact that nanowires are (basically) single crystalline - the conduction through the nanowire itself does not encounter any grain boundaries and potential barriers. The conduction from one nanowire to the other is similar to the conduction from one grain to the other. Also on the nanowire-to-nanowire junction there exists a potential barrier which electrons have to overcome to move from one nanowire to the other (see Fig. 2.8). The potential barrier height depends on the amount of oxygen species adsorbed on the surface of a nanowire network. [77] The resistance of the nanowire (R_{NW}) can be calculated as follows:

$$R_{NW} = \frac{\rho L}{(\frac{D_{channel}}{2})^2 \pi} \tag{2.4}$$

where ρ is the resistivity of the metal oxide, L - the nanowire length and $D_{channel}$ - the diameter of the conductive channel (without adsorbed species - equal to nanowire diameter, with adsorbed oxygen species - decreases by the formation of a depletion zone). [78] The resistance of the entire nanowire network depends strongly on the potential barriers at the nanowire-to-nanowire junctions.
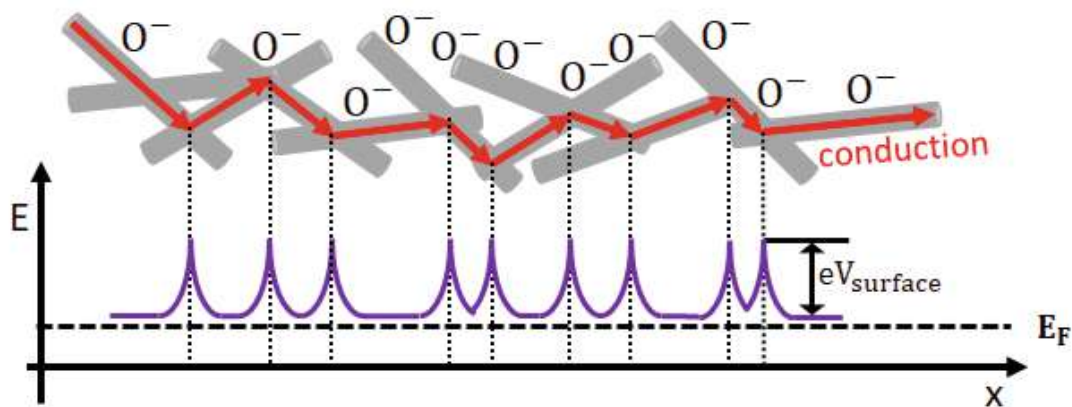
18

Figure 2.8: Conduction through nanowires in a multi-nanowire gas sensor system. [75, 77]

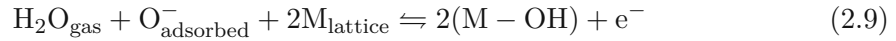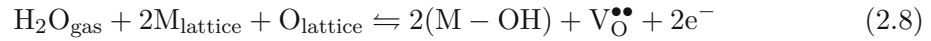### 2.1.4 Reactions with gases on the metal oxide surface

Ambient air

The conduction model of chemoresistive gas sensors would not be complete without an explanation how actually gases are reacting with the surface. Ambient air consists of 78% nitrogen, 21% of oxygen and 1% of various other gases (e.g. argon, hydrogen, CO_2, water vapor etc.). [79] Nitrogen is an inert gas - so the metal oxide gas sensor will not react with it. Oxygen, on the other hand, is different - it adsorbs on the surface, extracts the electrons from the metal oxide, can react with other gases, and releases the electrons again into the bulk. The reactions on the surface of metal oxide and their dependence on the temperature has been already shown in Fig. 2.5. The number of oxygen species adsorbed on the surface is directly proportional to the oxygen pressure. [69] At elevated temperatures, the oxygen reaction with the surface can be written as follows:

$$\frac{1}{2}O_2^{gas} + e_{surface}^- \rightleftharpoons O_{surface}^-\tag{2.5}$$
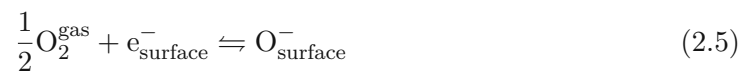
There is one more reaction which can take place at the surface of metal oxides: if there exists an oxygen vacancy ($V_O^{\bullet\bullet}$) in the lattice, oxygen from air can diffuse into the metal oxide and chemisorbs inside the lattice. This process leads to electron extraction due to the need of electrons to create the bond between oxygen and metal ions. [80]

$$V_O^{\bullet\bullet} + 2e_{bulk}^- + \frac{1}{2}O_2^{gas} \rightleftharpoons O_{lattice}\tag{2.6}$$

19
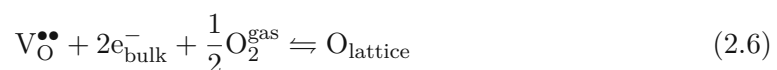
Another gas species present in the ambient atmosphere is water vapor. Reaction between water and the metal oxide surface depends on the temperature. For SnO_2 the water molecules absorption can occur below a temperature of 200°C - by physisorption or hydrogen bonding. Above that temperature, which corresponds to practical sensor operation temperatures, water molecules are not present at the surface. [68] The water molecules can react with the metal oxide surface by chemisorption in three different ways:

$$H_2O_{gas} + M_{lattice} + O_{lattice} \rightleftharpoons M - OH + (O_{lattice}H)^+ + e^- \tag{2.7}$$

$$H_2O_{gas} + 2M_{lattice} + O_{lattice} \rightleftharpoons 2(M - OH) + V_O^{\bullet\bullet} + 2e^- \tag{2.8}$$

$$H_2O_{gas} + O_{adsorbed}^- + 2M_{lattice} \rightleftharpoons 2(M - OH) + e^- \tag{2.9}$$

where $M_{lattice}$ is a metal atom inside the lattice (first layer on the surface), $O_{lattice}$ is an oxygen atom inside the lattice (first layer on the surface), $O_{adsorbed}^-$ is a pre-adsorbed oxygen ion and $V_O^{\bullet\bullet}$ is an oxygen vacancy inside the lattice (first layer on the surface). The water molecule dissociates into two species - negatively charged hydroxyl group (OH^-) and positively charged hydrogen (H^+).

In the first case (Eq. 2.7) a water molecule reacts with one metal atom and one oxygen atom inside the lattice. On the surface oxygen from water molecule bonds with metal atom from the lattice and one of the hydrogen atoms from the water molecule diffuses into the lattice and creates a bond with the oxygen atom next to the metal atom. After this process, the metal atom has two hydroxyl groups (one from the water molecule and one from its oxygen partner inside the lattice). Then the hydroxyl group inside the lattice is positively charged and releases one electron into the metal oxide (increases conductivity).

In the second case (Eq. 2.8) one water molecule reacts with two neighbouring metal atoms (M1 and M2). The water molecule dissociates into one hydroxyl group which connects with one metal atom M1, and the remaining hydrogen bonds with an oxygen atom which was located between the metal atoms (M1 and M2). The bond between oxygen and M1 breaks and another hydroxyl group is formed and connects with M2. On the site where the oxygen atom was bound in the lattice there is now a vaccancy - which means that two electrons are released into the bulk. [18, 80, 81]

In the third case (Eq. 2.9) one water molecule reacts with a pre-adsorbed oxygen ion. The mechanism is similar to that from Eq. 2.8 - the only difference is that the pre-adsorbed oxygen is used to form the second hydroxyl group - so there is no vacancy formed in the lattice, and an electron from the pre-adsorbed oxygen ion is released into the metal oxide. All the above reactions with water molecules were described in the literature for SnO_2. [68] Experiments for SnO_2 showed that at elevated temperatures the third mechanism dominates on the surface of metal oxide. [18] This suggests that if the water molecules

are present in ambient air, the number of oxygen species pre-adsorbed on the surface decreases. This will be very important later, for discussion about various types of gases interacting with the surface of the metal oxide.

Reducing and oxidizing gases

The gases detectable by metal oxides can be divided into two main groups: reducing and oxidizing gases.

When a reducing gas reaches the surface of the metal oxide it reacts with pre-adsorbed oxygen species and releases the electron into the bulk of the sensor material. This leads to a decrease of potential barrier (between grains/nanowires) and increase of conductivity (decrease the resistivity) of the gas sensitive material. The reactions can be written as follows:

$$R + O_2^- \overset{k_1}{\to} RO_2 + e^- \tag{2.10}$$

$$R + O^- \overset{k_2}{\to} RO + e^- \tag{2.11}$$

where k_1 and k_2 are rate constants for those reactions. The reactivity of a molecular oxygen ion (O_2^-) is smaller than the reactivity of an atomic ion (O^-) - which allows to neglect Eq. 2.10. [69, 81]

Oxidizing gases on the other hand act as electron acceptors and, if adsorbed on the surface, extract the electrons from the bulk metal oxide. This leads to a decrease of the electrical conductivity of the gas sensitive material. The main example of oxidizing gases is of course oxygen - which reactions with the metal oxide surface were shown in Chapter 2.1.3. Other oxidizing gases are ozone or nitrogen dioxide. The gas measurements performed in this thesis were mostly focused on reducing gases - and those test gases will be described now in detail.
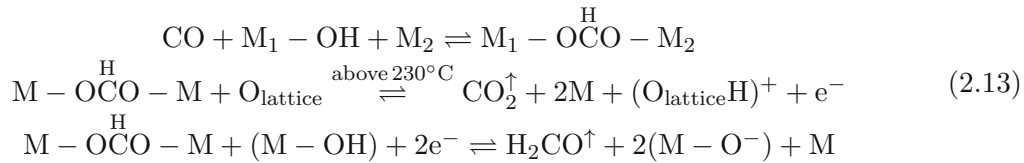
Carbon monoxide Carbon monoxide (CO) is an odorless and colorless gas, mostly generated by incomplete combustion of solid (carbon), liquid (heating oil) or gaseous fuels (heating gas or cooking gas). CO is also part of ambient air in concentrations up to 200 ppb. In higher concentrations it is highly toxic due to the ability to bind to hemoglobin (200 times higher affinity than binding to oxygen). Red blood cells are then transporting CO instead of oxygen into all cells in the body, which can lead to nausea, confusion, vomiting or even death. [82] The maximum allowed concentration at the workplace in Germany is 30 ppm [59], which should be detectable by gas sensors if one would like to use them for safety application.

CO is a reducing gas and, due to that, the reaction with metal oxide surface leads to an increase of the electrical conductivity for the gas sensitive material (for an n-type semiconductor). In absence of water molecules and presence of oxygen, CO reacts with

pre-adsorbed oxygen ion species and forms carbon dioxide molecules. This reaction is irreversible. [80, 83]

$$CO + O_{adsorbed}^- \rightarrow CO_2^\uparrow + e^- \tag{2.12}$$
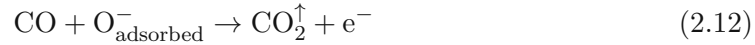
In presence of water CO can react with the hydroxyl groups on the surface:

$$CO + M_1 - OH + M_2 \rightleftharpoons M_1 - O\overset{H}{C}O - M_2$$
$$M - O\overset{H}{C}O - M + O_{lattice} \overset{above\,230°C}{\rightleftharpoons} CO_2^\uparrow + 2M + (O_{lattice}H)^+ + e^-$$
$$M - O\overset{H}{C}O - M + (M - OH) + 2e^- \rightleftharpoons H_2CO^\uparrow + 2(M - O^-) + M \tag{2.13}$$

where $O\overset{H}{C}O$ is a formate group connected to two metal atoms inside the lattice, and H_2CO is formaldehyde. Hence, carbon monoxide first reacts with a hydroxyl group bonded to metal atom and creates a formate group (connected to the two neighbouring metal atoms) which is stable up to 230°C (for SnO_2). Above this temperature, which is a temperature range used for gas sensing, two chemical reactions can occur:

- The formate group can decompose to carbon dioxide, the remaining hydrogen adsorbs on the oxygen inside the lattice and creates another hydroxyl group. An electron is released into the bulk - the electrical conductivity increases.

- The formate group can react with different hydroxyl groups and creates formaldehyde; remaining oxygen atoms adsorb on the surface. Electrons are extracted from the bulk - the electrical conductivity decreases. [84]

The most important conclusion from those reactions is as follows:

The CO and water molecules compete for reactions with the pre-adsorbed oxygen ion species. This leads to lower sensor signal in the presence of humidity, which agrees with experiments - and will be shown later in the experimental part of this thesis. [18]

Hydrogen sulfide Hydrogen sulfide (H_2S) is a colorless gas, with a specific smell of rotten eggs. It is used in textile production, drilling/refining fuels, wastewater treatment or in agriculture (landfills). Exposure to this gas may cause eyes irritation, dizziness, headaches or even coma. [85] H_2S is a gas, which is highly dangerous for humans: the human nose is extremely sensitive and can smell H_2S concentrations lower than 1 ppm. Higher concentrations (higher than 100 ppm), however, lead to immediate olfactory fatigue, and then the human nose cannot smell this gas anymore, which can lead to life-threatening situations. [86] The maximum allowed concentration at the workplace in Germany is 5 ppm [59], which should be detectable by gas sensors if one would like to use them for safety application.

H$_2$S is a reducing gas and, like CO, the chemical reaction with the metal oxide surface leads to an increase of the electrical conduction of the gas sensitive material (for an n-type semiconductor). In presence of oxygen the reaction of H$_2$S with the metal oxide is as follows: [87]

$$H_2S + 3O_{adsorbed}^- \rightarrow SO_2^\uparrow + H_2O + 3e^- \tag{2.14}$$
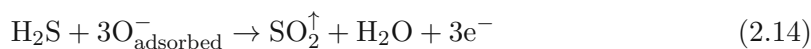
After complete desorption of oxygen ion species by H$_2$S molecules a direct interaction with lattice oxygen is possible, and sulfur is able to replace oxygen in the lattice: [80]

$$MO + H_2S \rightarrow MS + H_2O \tag{2.15}$$

In the presence of water, the conclusion is similar to the one made for CO - H$_2$S molecules and water molecules compete for reaction with pre-adsorbed oxygen ion species. Hydrogen sulfide reactions with hydroxyl groups adsorbed on the metal oxide were not found and have not been reported. This should lead to lower sensor signal in the presence of humidity.

Hydrocarbon mixture   Hydrocarbon mixture (HCMix) is a representative mixture of Volatile Organic Compounds (VOCs), which are a group of organics "having an initial boiling point less than or equal to 250°C measured at a standard pressure of 101,3 kPa" [88] The relatively low boiling point leads to possible evaporation of organic molecules into the air. Some of VOCs molecules are highly reactive with NO$_x$ and CO gases in presence of sun light and the resulting product is ozone (O$_3$). Hence, it is important to monitor and reduce the amount of emitted VOCs into the atmosphere. VOCs are emitted by a wide range of sources, not only human-related. The natural VOCs (NVOCs) are produced by plants in an amount of 1150 Tg of carbon per year (1150 Tg = 1150 Teragrams = $1,15 * 10^6$ tons) [89], and the anthropogenic sources (fossil fuels, solvents, biomass burning) is around 150 Tg of carbon per year. [90] Due to the huge variety of different gases, which belong to the group of VOCs, the health effects are very wide: from irritation and allergic effects to respiratory issues and even increase the risk of cancer. [91] The wide range of gases makes it also difficult to measure and calculate the total amount of VOCs in the air.
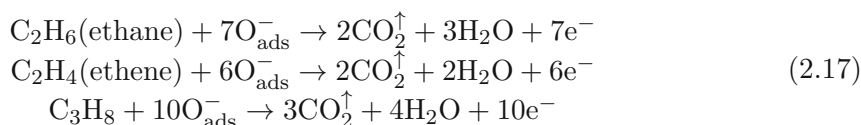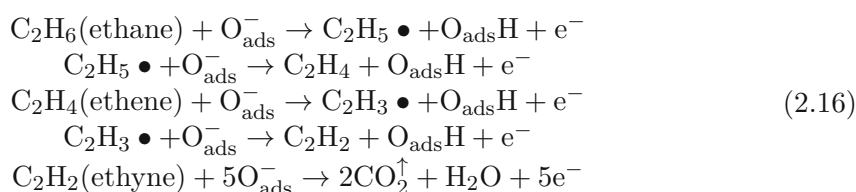
Companies are testing some specific gases and then estimate those as representative amount of VOCs. To check the sensitivity of sensor devices to VOCs, Sensirion for example is using ethanol, toluene and ISO16000-29 (n-octane and m-xylene in a molar ratio of 53:47). The company Membrapor is using a mixture of isopropanol, methanol, ethanol, formaldehyde, acetone, xylene, toluene, formic acid, acetic acid, vinegar, isobutylene and ethylene. Some companies specify the sensitivity of their sensors by an index of VOCs (i.e. Sensirion gives an index from 0-500, where 100 is an average value) [92], other companies are using concentrations (like Membrapor, 0-20 ppm). [92, 93]

In this thesis a specific ready-to-use hydrocarbon mixture (HCMix) of 500 ppm ethane, 500 ppm ethene (ethylene), 500 ppm ethyne (acetylene) and 500 ppm propane in nitrogen (total of 2000 ppm concentration in the bottle) from Linde Gas was used. The "collective" concentration of this gas mixture in the test chamber was controlled by mass flow controllers (see experimental setup Chapter 3.3.2) and calculated from the ratio of the flow of test gas and the background gas.

Hydrocarbons are reducing gases and the reactions in presence of pre-adsorbed oxygen ion species can occur in two directions:

- Step by step dehydrogenation or

- Combustion-like route

- both at the end producing carbon dioxide and water: [94–97]

$$C_2H_6(\text{ethane}) + O_{\text{ads}}^- \rightarrow C_2H_5 \bullet + O_{\text{ads}}H + e^-$$
$$C_2H_5 \bullet + O_{\text{ads}}^- \rightarrow C_2H_4 + O_{\text{ads}}H + e^-$$
$$C_2H_4(\text{ethene}) + O_{\text{ads}}^- \rightarrow C_2H_3 \bullet + O_{\text{ads}}H + e^-$$
$$C_2H_3 \bullet + O_{\text{ads}}^- \rightarrow C_2H_2 + O_{\text{ads}}H + e^-$$
$$C_2H_2(\text{ethyne}) + 5O_{\text{ads}}^- \rightarrow 2CO_2^\uparrow + H_2O + 5e^-$$

$$\text{(2.16)}$$

$$C_2H_6(\text{ethane}) + 7O_{\text{ads}}^- \rightarrow 2CO_2^\uparrow + 3H_2O + 7e^-$$
$$C_2H_4(\text{ethene}) + 6O_{\text{ads}}^- \rightarrow 2CO_2^\uparrow + 2H_2O + 6e^-$$
$$C_3H_8 + 10O_{\text{ads}}^- \rightarrow 3CO_2^\uparrow + 4H_2O + 10e^-$$

$$\text{(2.17)}$$

In the presence of water, the conclusion is again similar to the one made for CO and H_2S - HCMix molecules and water molecules compete for reactions with pre-adsorbed oxygen ion species. This should lead to a lower sensor signal in presence of humidity.

Toluene   Toluene ($C_6H_5CH_3$) can be considered as one of the VOCs.. In this work, the sensors were characterized separately towards toluene, because this gas can be emitted from furniture and is an issue for human health. [98] The maximum allowed concentration at the workplace in Germany is 50 ppm. [59] Toluene is widely used in industry, i.e. in paints, solvents, manicure products and gasoline. By CDC, "exposure to toluene can cause eye and nose irritation, tiredness, confusion, euphoria, dizziness, headache, dilated pupils, tears, anxiety, muscle fatigue, insomnia, nerve damage, inflammation of the skin, and liver and kidney damage." [99] Toluene is a reducing gas and reaction with metal oxide surface leads to increase of the electrical conductiicity of the gas sensitive material (for an n-type semiconductor). In presence of oxygen the chemical reaction of metal oxide with toluene is as follows: [100–103]

$$C_6H_5CH_3 + 18O_{\text{ads}}^- \rightarrow 7CO_2^\uparrow + 7H_2O + 18e^-$$
$$C_6H_5CH_3 + 9O_{2,\text{ads}}^- \rightarrow 7CO_2^\uparrow + 7H_2O + 9e^-$$

$$\text{(2.18)}$$

24
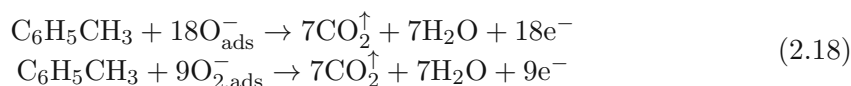
2.2   Metal oxide nanowires - growth and synthesis methods

Miniaturization of gas sensors is a key for consumer electronic applications, such as smartphones or smartwatches. Reducing the size means lower power consumption and lower price per device. Nanotechnology allows to create enormous numbers of various nanostructures - this work is focusing on nanowires (NWs) as sensing elements. Metal oxide nanowires are good candidates for gas sensing applications due to their specific properties:

- High surface-to-volume ratio

- Small distance between the surface (where reactions with gases take place) and the conductive path - meaning faster response times and/or possibility to measure even at room temperatures (carriers do not have to overcome many barriers to pass through the sensing material)

- Nanowires have a diameter comparable to the Debye length - so the depletion/ accumulation zones can expand to most of or even the whole nanowire

- Nanowires are, by definition, conduction channels - which is a perfect choice for conductometric sensors

- Existing technology allows to precisely control over crystallinity, morphology or composition of nanowires [104]

- Due to their single crystallinity nanowires have the ability to handle mechanical deformations without cracking - they are robust materials [105].

Growth methods to produce nanowires can be divided into two groups: top-down and bottom-up methods:

- Top-down methods are lithography-based techniques and involve photolithography, electron beam lithography, and ion beam lithography. The main advantages of those techniques are high precision of positioning the nanowires, high control of their sizes and potential integration into CMOS (complementary metal-oxide-semiconductor) technology. [106] Drawbacks of lithography-based methods are high costs and long fabrication time. In case that the nanowires are directly processed on a CMOS chip, the maximum allowable temperature, which the chip can withstand, limits the synthesis procedure.

- Bottom-up methods are based on different approach - nanowires are produced starting from the bottom and they build up from molecular building blocks. Advantages of the bottom-up methods are high control over the crystallinity and purity of nanowires and low cost of experimental equipment compared to lithography processes. There is also no limitation in pressure, temperature or chemical background

- which could be devastating for the microchip in a direct top-down approach. The lack of limits in bottom up production also has its consequences - the necessity for transfer and alignment of the nanowires onto the device (chip). [107] The nanowire transfer is the main topic of this work and will be described later (Chapter 2.3). All the metal oxide nanowires presented in this work were produced by bottom-up techniques and the description of them will be presented now.

2.2.1 Vapour phase growth

The growth of nanowires from the vapour phase requires evaporation of the source material and transportation of the resulting vapours by a proper carrier gas to the substrate, where the actual nanowire growth should occur. Evaporation of the material can be achieved by thermal treatment, laser, electron beam or ion beam heating. Vapour phase growth can be obtained by two different mechanisms: vapour solid (VS) and vapour liquid solid (VLS).

- The VS growth is based on direct condensation of the vapour source material without any catalyst. The condensation occurs on the substrate at lower temperature than the evaporation. On the substrate seed crystals are formed and act as nucleation sites (like catalyst). 1D growth (nanowires) is preferable to ensure minimization of surface energy.

- The VLS growth is based on the presence of a catalyst (usually metal). The substrate with the catalyst is prepared by e.g. sputtering, thermal evaporation or even sol-gel method, then the substrate is heated to the desired deposition temperature. During heating the metal catalyst changes to liquid phase and catalyst droplets are formed. The size of the droplets determines the size of the nanowires, and the catalyst material can determine the crystal structure of the nanowires. The source material in vapour phase absorbs on the substrate and creates a catalytic liquid alloy clusters (metal + source material) which have lower activation energy of nucleation and, due to that, the growth proceeds in 1D structures. The vapour source material will prefer to grow on the nucleation seeds at liquid-solid interface. [106, 108, 109]

Many different synthesis techniques are based on the vapour phase growth. Some of those techniques and their examples will be presented now.

Thermal oxidation

The thermal oxidation process is based on heat treatment of the source material (for metal oxide nanowires growth - usually metal) and subsequent oxidation of it in oxygen-containing background gas. The source metal can be in form of powders (i.e. Zn powder to obtain ZnO nanowires [110]), foils (Cu foil to obtain CuO nanowires [111]) or even wires (Cu wire wrapped over a heater to obtain CuO nanowires [112]). Adjustment of the process parameters (temperature, background gas, gas flow) allows to obtain different
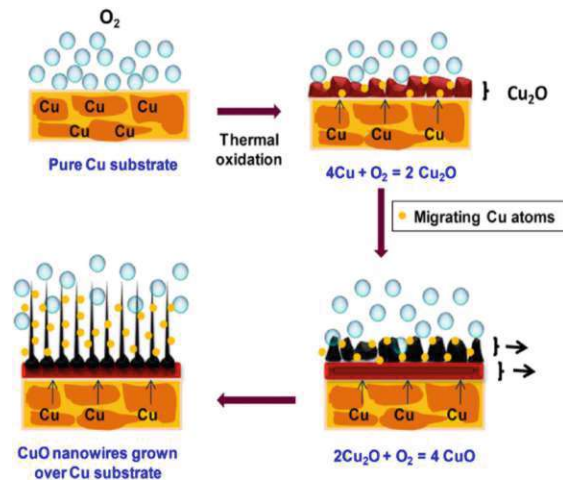
Figure 2.9: CuO nanowires growth mechanism - copper thermal oxidation. Copied from [113].

nanostructures. Thermal oxidation does not need any catalyst - so it is based on the vapour solid mechanism. An exemplary process is copper oxidation to obtain cupric oxide nanowires (see Fig. 2.9).

Thermal evaporation

The thermal evaporation process can be either catalyst-based (VLS mechanism) or self-catalytic (VS mechanism). The main difference between thermal oxidation and thermal evaporation is the background gas, which is usually an inert gas (e.g. Argon) for the thermal evaporation. The gas flow is used to transport the vapour onto the substrate, which has lower temperature than the temperature used for thermal evaporation of the source material. [114] Proper adjustment of the process parameters (temperature of the substrate, gas flow, catalyst - size and material) allow to obtain different morphologies or structures of the resulting product, like nanobelts, nanowires, or nanoribbons. [115]

There are also some other techniques such as oxidation by plasma treatment, where a metal foil is treated with oxygen plasma (e.g. niobium foil - [116]), In literature also, "a combination of carbothermal reduction and catalyst-mediated heteroepitaxial growth" has been reported, where In_2O_3 and graphite were first mixed and then subsequently a thermal evaporation process was used to obtain nanowires [117], see Fig. 2.10. Also an arc-discharge-based synthesis has been demonstrated, where graphite electrodes with gallium nitride were used to obtain Ga_2O_3 nanorods [118]. The main advantage of the vapour phase growth is high crystallinity of the product, but the disadvantage is that the growth involves very high temperatures (e.g. 1000°C for previously mentioned In_2O_3 nanowires). [109]

27
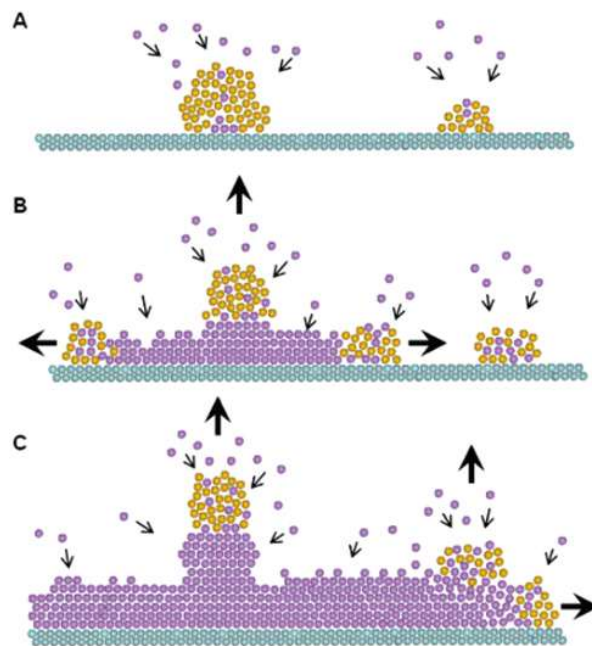
Figure 2.10: In_2O_3 nanowires growth mechanism - thermal evaporation. Copied from [117].

2.2.2 Liquid phase growth

The growth of nanowires from the liquid phase enables the use of considerably lower temperatures (e.g. 150°C for TiO_2 nanorods synthesis [119]) as compared to the vapour phase growth. The crystalline quality of the nanowires might be lower, but the advantages are reduction of fabrication cost and relatively simple way to go from laboratory experiment to large-scale production. Liquid phase growth methods can be divided into two groups: template-assisted and template-free methods.

Template-assisted liquid phase growth

The template-assisted nanowire growth uses templates which exhibit well-ordered and uniform in diameter nanochannels. Mostly anodic aluminium oxide - AAO is used as a template. The material for metal oxide nanowire growth is deposited into the nanochannels by i.e. electrodeposition. For example Zn is deposited at AAO membrane and then oxidized to ZnO nanowires. [120] Also AAO template was immersed in a mixture of $CuSO_4$ and H_2SO_4, next through the electrodeposition process Cu nanowires were formed and then calcinated to CuO nanowires in ambient atmosphere. [121] Another option is the sol-gel synthesis, where the AAO template is immersed in $Cr(OH)_3$ sol

28
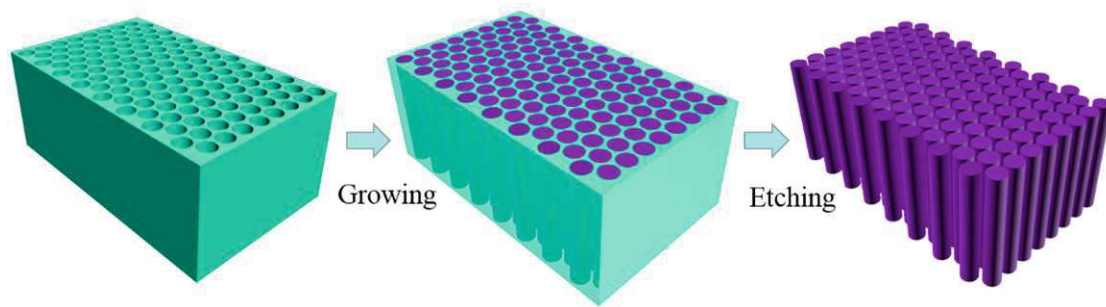
Figure 2.11: $Lu_2O_3 : Eu^{3+}$ nanowires growth mechanism - template-assisted growth by the sol-gel process using anodic aluminium oxide (AAO) templates. Copied from [124].

and then annealed to Cr_2O_3 nanowires. [122] Advantages of such processes are high uniformity of the nanowires diameters and the possibility to adjust the diameter and length of the nanowires just by changing the pores/nanochannel sizes. Drawbacks are the. necessity of template removal, where usually NaOH is needed, which is a strong base and may have an impact on the device, and that the nanowires are usually polycrystalline. [123] A schematic illustration of template-assisted growth is presented in Fig. 2.11.

Template-free liquid phase growth

The template-free nanowire growth can be performed by:

- Simple chemical reaction: $(Cu(NO_3)_2$ reacts with strong bases and $Cu(OH)_2$ nanowires are formed, by further calcination/dehydration CuO nanowires can be generated. [125] Also refluxing $SnC_2O_4 \cdot 2H_2O$ with organic polymer-containing solutions leads to SnO_2 nanocrystalline nanowire growth [126].

- Hydrothermal reaction: basic principle of such reaction is crystallization of the substance at high temperature and pressure (mostly above 100°C and above 1 atm) in aqueous solutions inside a pressure-resistant steel autoclave. For metal oxide nanowires the metal precursor, usually a metal salt, such as sodium tungstate Na_2WO_4 for WO_x nanowires synthesis [127], is placed inside the autoclave together with water and, if necessary, an additional organic solution and/or surfactants. During the thermal heating process, the metal precursor dissolves in the hotter part of the solution, which is usually the bottom of the autoclave, while the saturated solution mixes with the upper part of the solution in the cooler part. The material gets denser, moves down to the hotter zone and the process starts again. At a certain point the cooler part is supersaturated and the crystallization occurs. [109, 128] The growth can occur without surfactants. As an example $TiCl_3$ inside organic solution forms TiO_2 nanorods. [119] The use of surfactants, like $Zn(OAc)_2 \cdot 2H_2O$

29
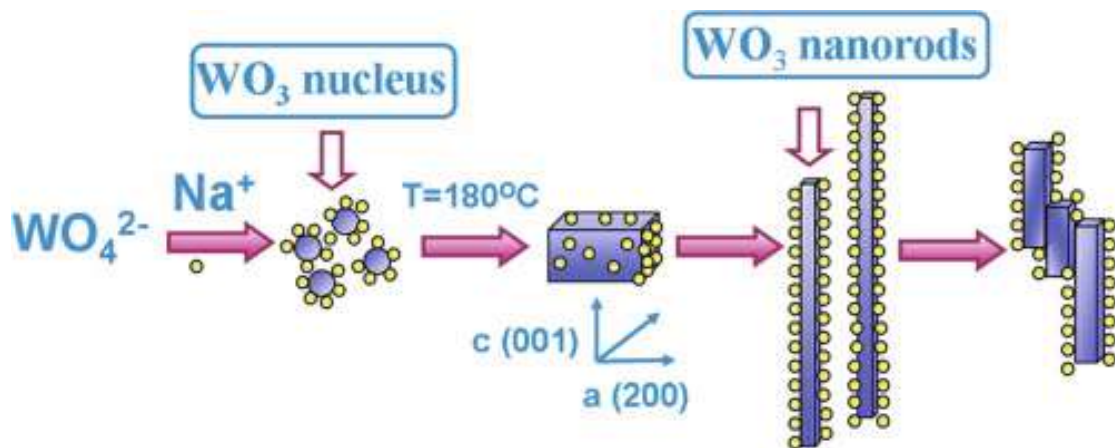
Figure 2.12: WO$_3$ nanowires growth mechanism - hydrothermal growth. Copied from [130].

solution which was added to surfactant-containing organic solution and heated in the autoclave, results in ZnO nanowires growth [129]). A schematic illustration of hydrothermal growth is presented in Fig. 2.12.

- Electrochemical deposition: this process is based on redox reactions in solutions. The substrate is immersed in the electrolyte and acts as working electrode, whereas the counter electrode forces the ions in the solution to move towards the substrate. Mostly the reference electrode is also used to control the potential between working and counter electrodes. The growth depends on the parameters from the solution (concentration, surfactants presence) and from the potential applied to the system. One example is production of SnO$_2$ nanowires onto ITO substrates with sodium dodecyl sulfade (SDS) addition as a surfactant. [131] A schematic illustration of hydrothermal growth is presented in Fig. 2.13.

- Electrospinning: this technology is based on applying a high voltage between the substrate and a syringe, which contains the source material in liquid phase. Without the high voltage normal droplets would be formed; the voltage produces a "charged liquid jet" of the source material which moves towards the substrate, where it is collected and produces solid fibers. The growth depends on the solution properties and the applied voltage. [133] An example of electrospinning metal oxide nanowires/nanofibers is the synthesis of TiO$_2$ nanofibers. Titanium butoxide (TiBu) is mixed with organic solution and, by electrospinning over ITO (indium tin oxide)
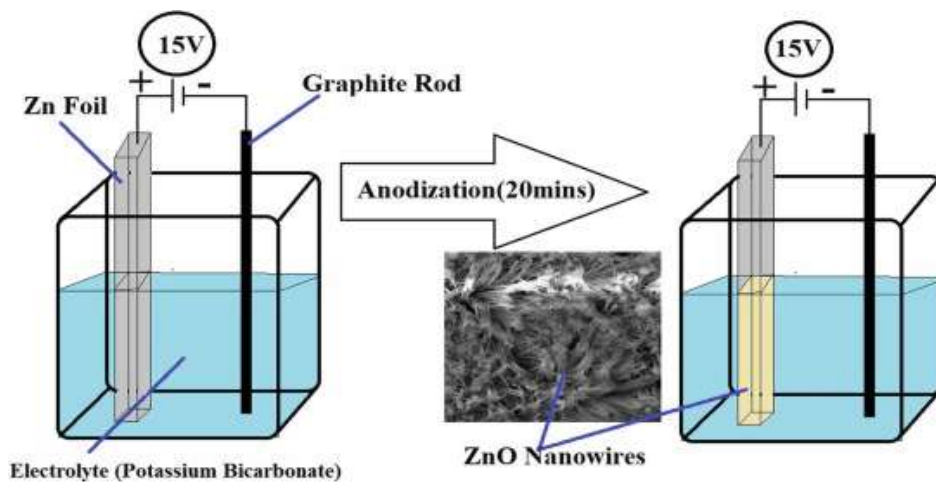
Figure 2.13: ZnO nanowires growth mechanism - electrochemical growth. Copied from [132].
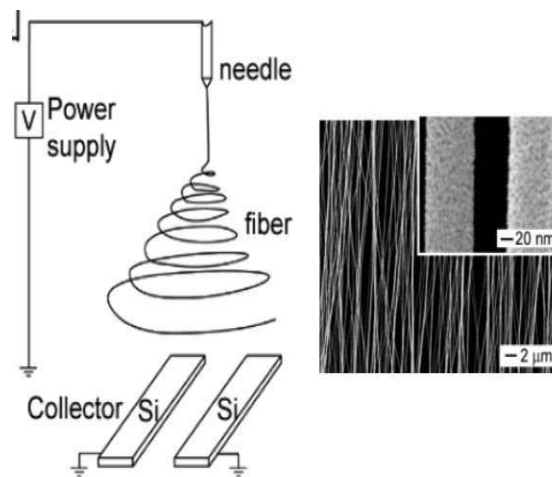
Figure 2.14: SnO$_2$ nanowires growth mechanism - electrospinning growth. Copied from [135].

collector and subsequent calcination, TiO$_2$ nanowires or nanofibers, respectively, were obtained. [134] This method allows to produce high amount of nanowires or nanofibers in diameters range of a few hundred nm. A schematic illustration of electrospinning is presented in Fig. 2.14.

31

2.3 Transfer techniques

One dimensional nanostructures, such as nanowires, have unique properties which can be used in many different applications. With respect to practical device fabrication, it is necessary to develop methods which allow a controllable transfer of those nanostructures on the substrate. In ideal case, this method should allow to proper alignment on the devices. Integration of 1D nanostructures is crucial for building functional systems, such as nanowire-based chemical sensors. While many different methods have been developed so far for the huge variety of 1D-nanostructures, the focus of this thesis is the implementation of metal oxide nanowires. Assembly of nanowires, which were synthesized by bottom-up growth, can be divided into two groups:

- "Grow-in-place" - this technology is based on direct growth of nanowires on the final substrate or device from i.e. seed particles or by use of a catalyst. This method is a transfer-free mechanism, because the nanowires are directly grown on the location, where they are required. A main disadvantage is the limitation of nanowire growth parameter, in particular the required growth temperatures, which cannot exceed maximum allowable temperatures for the device in case of a CMOS microchip or even a flexible polymer based substrate (e.g. PCB). Hence, the type of substrate may considerably limit the other process parameters such as pH-value or pressure.

- "Grow-and-place" - this technology is based on first growing the nanowires on the separate substrate (donor substrate) or in a liquid, and subsequently transfer onto the final device (i.e. electronic chip). Main advantage is that there are no temperature or pressure limitations for the nanowires growth process. The main disadvantage is the transfer process itself, which can damage the nanowires or, due to contamination from e.g. organic solvents, may be detrimental for gas sensing properties. [136–140]

The "grow-in-place" methodology has many examples in the literature. Some of those techniques and their examples will be presented now.

- Nanochannel-guided nanowire growth: Si nanowires were grown on a specific substrate; nanochannels were fabricated by e-beam lithography and gold catalyst particles were placed inside those channels to induce the nanowire growth [141]. The main advantage is a precise control over the nanowires dimensions, the density and placement; the disadvantage is the complex fabrication of such nanochannel template. The necessity of e-beam lithography process makes it slow and expensive in terms of experimental setup.

- Patterned substrate with seed layer for aligned-nanowires growth: ZnO nanowires were obtained by firstly depositing ZnO stripes with an additional inactive Cr layer on top of the ZnO stripes - to prevent the nanowires growth perpendicular to the substrate. Secondly the as-prepared substrate was immersed in a growth solution

and ZnO nanowires were grown parallel to the substrate surface and perpendicular to the stripes walls. [142]). This method has some advantages: the possibility to grow the nanowires on basically any substrate, the growth methods are simple, require low temperatures and are easy to scale-up. Disadvantage is the missing alignment - the nanowires do not grow precisely perpendicular to the stripe walls.

- Precisely prepared substrate with seed particles for aligned-nanowires growth: ZnO nanowires were grown due to preferential epitaxial growth on specific crystallographic steps of Au nanodots catalyst structures (diameter between 5-50nm, but also bigger rectangles of 430 nm $\times$ 140 nm size), which are prepared by photolithography [143] or e-beam lithography [144]. The substrate was precisely cut to control the growth of the nanowires in preferential crystallographic directions. The growth mechanism itself is a vapour phase growth. The epitaxial growth allows to precisely control the obtained nanowires orientations and size, but the substrates are quite expensive due to necessary precision in its preparation.

- Field-assisted electrospinning: ZnO hollow nanofibers were prepared by electrospinning - see. Sec. 2.2.2 - the solution with polymer was spin-coated on a substrate which was additionally negatively biased. The polymeric nanofibers itself were charged positively and, due to the additional applied electric field, the fibers aligned themselves parallel to each other. Next, ZnO was sputtered on such nanofibers, which act as kind of template and, by subsequent calcination, the polymer was removed, and ZnO hollow fibers were produced [145]. This method allows to grow roughly aligned nanostructures, which are parallel to each other and the template removal is an easy process. The control of morphology and structure is crucial and often ineffective - the obtained structures are porous; but for chemical sensing this might even be an advantage, as was demonstrated for other metal oxides. [146]

The "growth-and-place" methodology can be divided into three groups:

- Wet transfer: this process necessitates using liquids to transfer the nanowires either by direct synthesis of nanowires in solutions or by dispersing the nanowires in solution and subsequent drop coating or ink-jet printing of the nanowires-containing solution onto the final device.

- Dry transfer: this process does not need any solution, and mostly uses specific stamps, or tape to transfer the nanowires from a donor substrate to the final substrate

- Mixed transfer: this process involves a transfer with a polymeric stamp, whereas the polymer is firstly deposited on the growth substrate to embed the nanowires, then cured, and transferred on the final surface; and eventually the polymer is removed.

A lot of examples are reported in the literature; they are summarized in Table 2.5. List of the shortcuts used it this table:

PMMA - poly(methyl methacrylate)
PDMS - polydimethylsiloxane
PAni - polyaniline
TBAF - Tetra-n-butylammonium fluoride

AAO - anodic aluminium oxide
PUA - poly(urethane acrylate)
PET - polyethylene terephthalate (polyester)
IgG - immunoglobulin G

Table 2.5: Transfer techniques in literature.

Transfer technique	Transfer medium	Source
Wet transfer		
Drop-coating with PDMS as a mask	SnO_2 NWs solution (water and isopropanol)	[147]
Drop-coating plus laser printing of liquid-phase	Graphene solution in N-methylpyrrolidone	[148]
Laser-induced forward transfer of graphene oxide (GO) on quartz	GO solution	[149]
Drop-coating plus additional heating/rinsing/mechanical pressing after rinsing, final process - air drying	Filtered Ag-NWs in ethanol solution	[150]
Marker frame on graphene, wet etching of growth substrate, rinsing in water and then water pumped out and lowering the graphene onto the final surface	Marker frame and water	[151]
Thermal nanoimprint in PMMA film with roll-to-roll nanoimprinting of resin, hardened in UV	Resin mold fabricated by roll-to-roll nanoimprinting	[152]
Dry transfer		
Microstructured silicon ribbons stamping	Nitto Tape / PDMS stamp	[153]
Stamping of PDMS with silicon microstructures	PDMS stamp	[154]
Stamping of PDMS with silicon microwires	PDMS stamp	[155]
Si-micropillars embossed into the PMMA-PAni, growth substrate is removed by shear/bending fracturing	No medium, just growth substrate removal by lateral force and breaking the Si-micropillars	[156]

Transfer technique	Transfer medium	Source
SNAP - superlattice nanowire pattern transfer, silicon nanowires were stamped on plastic surfaces	PDMS stamp	[157]
Contact printing of ZrO_2 NW on top of graphene, NWs were transferred by pressing and sliding the growth substrate (additional aligning by shear forces)	No medium, just growth substrate removal by pressing and sliding	[158]
Exfoliation of graphene with adhesive tapes	Adhesive tapes: 3M France Ltd., type "810" and Nitto Denko UK Ltd., type "SWT 10+"	[159]
Tape transfer of epitaxial graphene onto SiO_2/Si, GaN and Al_2O_3	Nitto Denko Revalpha thermal release tape	[160]
Stamping of PDMS with Si microwires, washing the PDMS residues with TBAF 1% solution in propylene glycol methyl ether acetate	PDMS stamp	[161]
Contact printing of Si NWs with adhesive layer (photoresist) on the target substrate, adhesive layer removed after transfer with O_2 plasma	Adhesive layer on target substrate	[162]
stamping of PDMS with nanofibers	PDMS stamp	[163]
Drop-coating Ag NW solution on patterned film mask, evacuate the liquid through membrane filter, press the substrate to the NWs/filter mask and peel off the film mask	Patterned film mask/membrane filter	[164]
Drop-coating Ag NW solution on AAO filter, evacuate the liquid through membrane filter, pressing the pre-patterned PDMS stamp onto Ag-NWs and transfer on glass target substrate	Pre-patterned PDMS stamp	[165]
Mixed transfer		
Poly(L-lactic acid) spin-coating on Au-NPs or Ag NW, and PDMS as stamp for the polymer	Poly(L-lactic acid) stamp	[166]
PDMS spin-coating as a stamp on InAsP QDs	PDMS stamp	[167]

35

Transfer technique	Transfer medium	Source
Spin-coating of PMMA on graphene and PDMS as frame to transfer	Graphene/PMMA/PDMS frame	[168]
Liquid-bridge-mediated nanotransfer moulding, ink solution inside the holes in the mould, solidifying the ink and transferring on a wetted final surface	PUA and PDMS mould as frame	[169]
Spin-coating of PMMA on graphene and PDMS as frame to transfer on Ag-NWs; acetone for PMMA removal	PMMA/PDMS frame	[170]
Drop-casting of PMMA on graphene and spin-coating Ag-NW solution on glass, PMMA used as stamp to cover Ag-NWs with graphene frame to transfer on Ag-NWs; chloroform for PMMA removal	PMMA stamp and Ag-NW ink	[171]
Nano-patterned layer of positive resist (produced by laser interference lithograph) is transferred into metallic structure	Positive resist - as sacrificial layer	[172]
Roll-to-roll transfer of graphene from copper foil as a sacrificial growth substrate	Polymer support/Cu etchant/target substrate (PET)	[173]
Immersing PDMS stamp into solution of ZnO NPs in EtOH, subsequent stamping on target substrate with Au-electrode	Patterned PDMS stamp, O_2 plasma treated	[174]
Immersing PDMS stamp into solution of IgG antibodies in phosphate buffered saline, micro contact printing of IgG antibodies on glass substrate	Patterned PDMS stamp, O_2 plasma treated	[175]
Spin-coating of PMMA on PUA mold, pressed into target substrate by nanotransfer molding (NTM), PMMA removed by O_2 plasma etching	PMMA/PUA mold	[176]
contact printing (slip and slide with pressing) of Ge NWs onto prepatterned substrate with lubricant, then resist lift-off with acetone	Growth substrate, target substrate with lubricant	[177]
Spin-coating of PMMA on graphene, etching Cu-growth substrate, cleaning the PMMA/graphene stack, put on target substrate, removing PMMA with acetone	PMMA stamp	[178]

36

Transfer technique	Transfer medium	Source
PMMA drop-coating of graphene, etching Cu-growth substrate, washing with DI water, put on target substrate, adding drops of fresh PMMA on the stack (PMMA/graphene), removing PMMA with acetone	PMMA stamp	[179]
SNAP - superlattice nanowire pattern transfer, metallic nanowires were stamped directly from growth substrate onto epoxy film (adhesion layer) on Si substrate, growth substrate was etched, target substrate with NWs was rinsed and O_2 plasma treated (remove adhesion layer)	Sacrificial growth substrate, target substrate with adhesive layer	[180]

Wet transfer processes have many advantages; the deposition of the nanowire suspension is very precise, the amount of solution - and so the nanowires density - is precisely controlled and the solvent can be easily removed from the final substrate. This technique is also suitable for basic testing, because it can be performed manually, by drop coating. Of course, the size of the droplet limits the minimum achievable feature size of the device, where the nanowires should be deposited. By using inkjet printers [181] or electrostatic-induced (ES) inkjet printers - the droplet size can be considerably smaller than 100µm. [182] Moreover, by applying external forces an alignment of the nanowires can be achieved. Several approaches are feasible:

- Electric-field-assisted assembly: this technique is based on a substrate with an integrated electrode system and, by applying an alternating electric field (AC) to the electrodes, the nanowires in the solution start to align themselves due to dielectrophoretic forces. The process can be controlled by gap distance between the electrodes and by magnitude and frequency of the electric field. As an example, ZnO nanowires were assembled by this method. [183] A schematic illustration of an electric-field-assisted assembly is presented in Fig. 2.15.

- Fluid flow directed assembly: this method employs a solution with nanowires, which flows through microchannels made by polymers and the nanowires align themselves parallel to the flow direction by shear forces. By controlling the flow rate, time of flow and size of microchannels, a precise alignment and density of nanowires can be achieved. [184] This method is simple and cost efficient. A schematic illustration of a fluid flow directed assembly is presented in Fig. 2.16.

37

Electric field induction
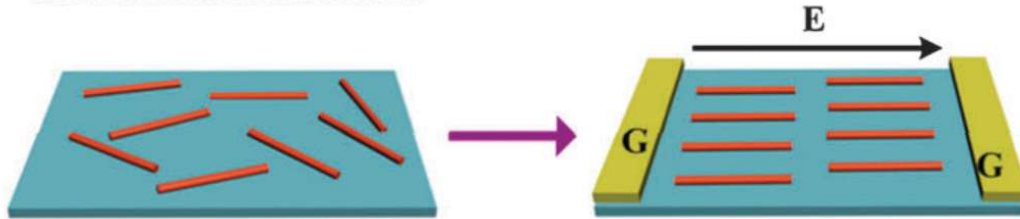
Figure 2.15: Electric-field-assisted assembly. Copied from [138].

Flow induced alignment
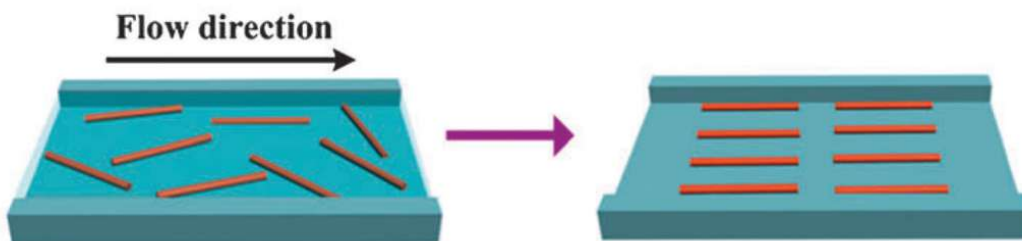
Figure 2.16: Fluid flow directed assembly. Copied from [138].

- Bubble-blown assembly: this method requires three steps. Firstly the nanowires are dispersed in a polymer-based solution, secondly a bubble is formed by blowing nitrogen into the solution and thirdly the nanowires from the bubble are transferred onto the substrate. This is achieved by pressing a substrate into the bubble and destructing the bubble. This transfer procedure can be controlled by the nanowires concentration in the solution, the gas flow parameters into the bubble and the placement of substrates depending on the position of the bubble. The substrate can be a Si-wafer or even a flexible matrix. [185, 186] A schematic illustration of a bubble-blown assembly is presented in Fig. 2.17.

- Langmuir-Blodgett (LB) assembly: a typical LB process requires a solution with nanowires-surfactant monolayer on top of the surface. This solution is then compressed and transferred on the final substrate by drawing the substrate out of the solution. The compression of the monolayer leads to close packaging of the nanowires and, due to that, their alignment parallel to each other, because the nanowires try to reduce the energy of the system. By controlling the speed of "pulling out" the substrate from the solution and the speed of compression, the density of nanowires on the substrate can be controlled. [187, 188] A schematic illustration of a Langmuir-Blodgett assembly is presented in Fig. 2.18.
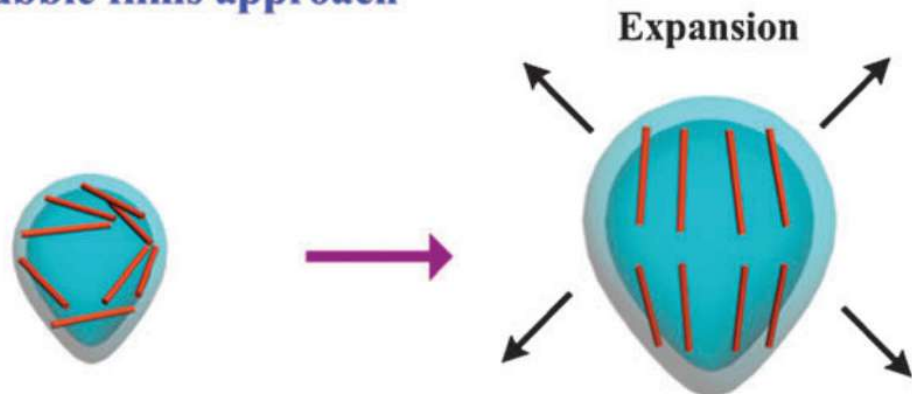
Figure 2.17: Bubble-blown assembly. Copied from [138].

Figure 2.18: Langmuir-Blodgett assembly. Copied from [138].
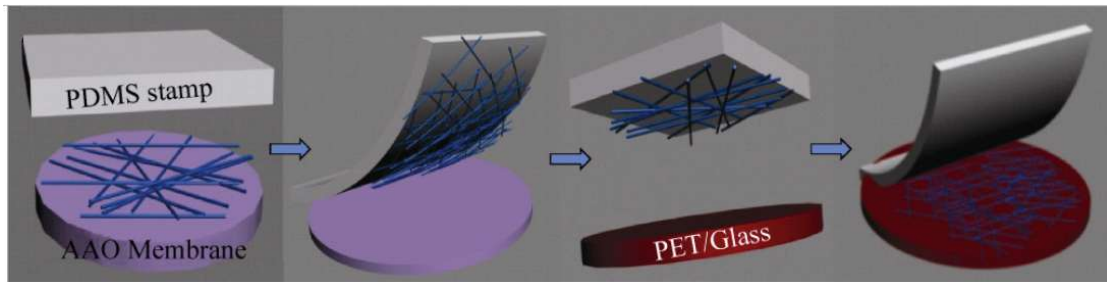
Figure 2.19: Stamp-based transfer. Copied from [165].

Despite many advantages of wet transfer processes there is one crucial disadvantage for using it for the assembly of metal oxide nanowires for gas sensing: the use of organic solvents/polymers, which can result in detrimental contamination. Experiments in our group and also results reported in literature [189] demonstrated that organic residues on the metal oxide can influence the adsorption of gases on the surface and, due to that, reduce or even "kill" the chemical sensing response. Hence, contamination is a big issue when handling MOx nanowires. Moreover, it was also observed in our group that metal oxide sensors, which were investigated in SEM, were obviously contaminated by carbon due to the SEM inspection. While measurement before the SEM inspection showed a good sensor performance, the sensor was "blind" after the SEM inspection. That is why the dry transfer processes were investigated in this work and the use of liquids was minimized or completely eliminated.

The main dry transfer methods are stamp/tape based transfer; and contact printing:

- Stamp/tape-based transfer: the nanowires are removed from the growth substrate by polymeric stamps or tapes and transferred onto the final substrate (see examples in Tab. 2.5). The stamp materials mostly used are PDMS or PMMA polymers; the tape can be a normal Scotch tape (e.g. transparent adhesive tape, produced e.g. by 3M company), which has also been successfully used in the graphene production by mechanical exfoliation and transfer onto the final substrate [190]. Also a thermal release tapes (adhesive tape that sticks firmly at room temperature but can be easily removed with the application of heat, produced e.g. by Nitto company) can be used to "pick up" the nanowires. This method is simple, scalable, cheap, and fast. Moreover, if the nanowires are grown aligned on the growth substrate, this method would result in parallel alignment of the nanowires on the final substrate. By the use of a polymeric soft stamp no organic residues are left on the final substrate; by use of a sticky tape - the rests of the glue could be potentially the source of a contamination. The stamp/tape method is also very useful for preliminary experiments, because it can be simply made "by hand". A schematic illustration of a stamp/tape-based transfer is presented in Fig. 2.19.

- Contact printing: this technique is based on a direct transfer of nanowires by directional sliding of the growth substrate directly on the final substrate. The final substrate can be patterned by lithography to obtain nanowires only at desired locations; there is also a possibility to use lubricants (e.g. octane and mineral oil mixture) to minimize friction and reduce potential mechanical damage such as breakage of the nanowires. [177, 191] There are also some interesting processes which are based on contact printing:

  - Nanocombing: the growth substrate carries an unaligned mesh of nanowires, the transfer substrate exhibits ordered "anchoring regions" to stick the ends of the nanowires onto those regions. By contacting those two substrates face-to-face and subsequent pulling the growth substrate over the final surface with use of a lubricant, well-aligned arrangement of the nanowires, precisely
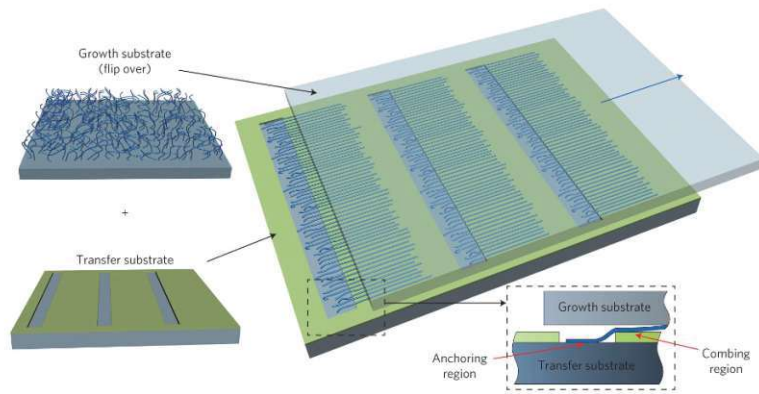
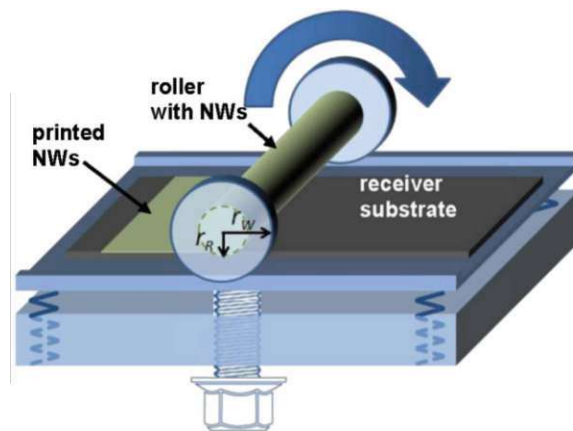Figure 2.20: Nanocombing. Copied from [192].

Figure 2.21: Roll contact printing. Copied from [193].

positioned by the anchoring regions, can be realized. The "pulling over process" is comparable to combing hair - that is why the process is called nanocombing. [192] A schematic illustration of a stamp/tape-based transfer is presented in Fig. 2.20.

– Roll contact printing: the growth substrate has the shape of a cylinder with nanowires grown perpendicular to the surface. This cylinder is rolled over the final substrate, the nanowires are detached from the growth substrate and aligned as parallel arrays on the final substrate. [193] A schematic illustration of a roll contact printing is presented in Fig. 2.21.

CHAPTER 3

Experimental part

3.1 Metal oxide nanowires growth

The wide range of methods used for nanowires growth can be divided into two main groups: vapour phase growth and liquid phase growth, as described in Sec. 2.2. Both methods were used in this work. Three different techniques were used to growth metal oxide nanowires:

- Thermal oxidation of a metallic foil for fabrication of CuO nanowires

- A two-step annealing with a metal-catalyst, for fabrication of SnO_2 nanowires and

- A hydrothermal synthesis process for fabrication of WO_3 nanowires

All of these techniques could be in principle easily adjusted and upscaled to an industry level due to a high number of nanowires prepared by each of the methods. The properties of the metal oxides applied in this work, their growth techniques and characterisation methods will be presented now.

3.1.1 Characterisation methods

The nanowires were characterised with Scanning Electron Microscopy (SEM) at Materials Center Leoben Forschung GmbH with help of Zeiss Instruments. The SEM images show the size and morphology of the nanowires, and also supported the selection of the best transfer method of nanowires (see Chapter 3.2). The Transmission Electron Microscopy (TEM) was performed at the Austrian Center for Electron Microscopy and Nanoanalysis (FELMI-ZFE) on a FEI Tecnai F20 with an operation voltage of 200 kV. The TEM images showed the size of nanowires after transfer procedureon TEM grids with drop coating. Raman spectroscopy was performed using a Horiba Jobin Yvon, LabRAM HR800 with

a green Ar laser of 514.5 nm and a spot size of around 1 μm at room temperature at the Department Applied Geosciences and Geophysics at Montanuniversität Leoben. The Raman spectra showed the chemical structure of the drop-coated CuO nanowires. XRD measurements were also performed using a PANalytical EMPYREAN diffractometer with Cu Kα radiation ($\lambda = 1.54$ ˚A) at the Institute of Solid State Physics, Graz University of Technology. This method allowed for in-situ analysis of the CuO nanowires during the growth process.

3.1.2 Copper (II) oxide

Copper (II) oxide is a p-type semiconductor with a band gap of 1.2 eV in bulk [194, 195]. Main CuO applications, beside gas sensing [196], are antimicrobial coatings [197], electrochemical material for lithium-ion batteries [198] and solar cells [199].
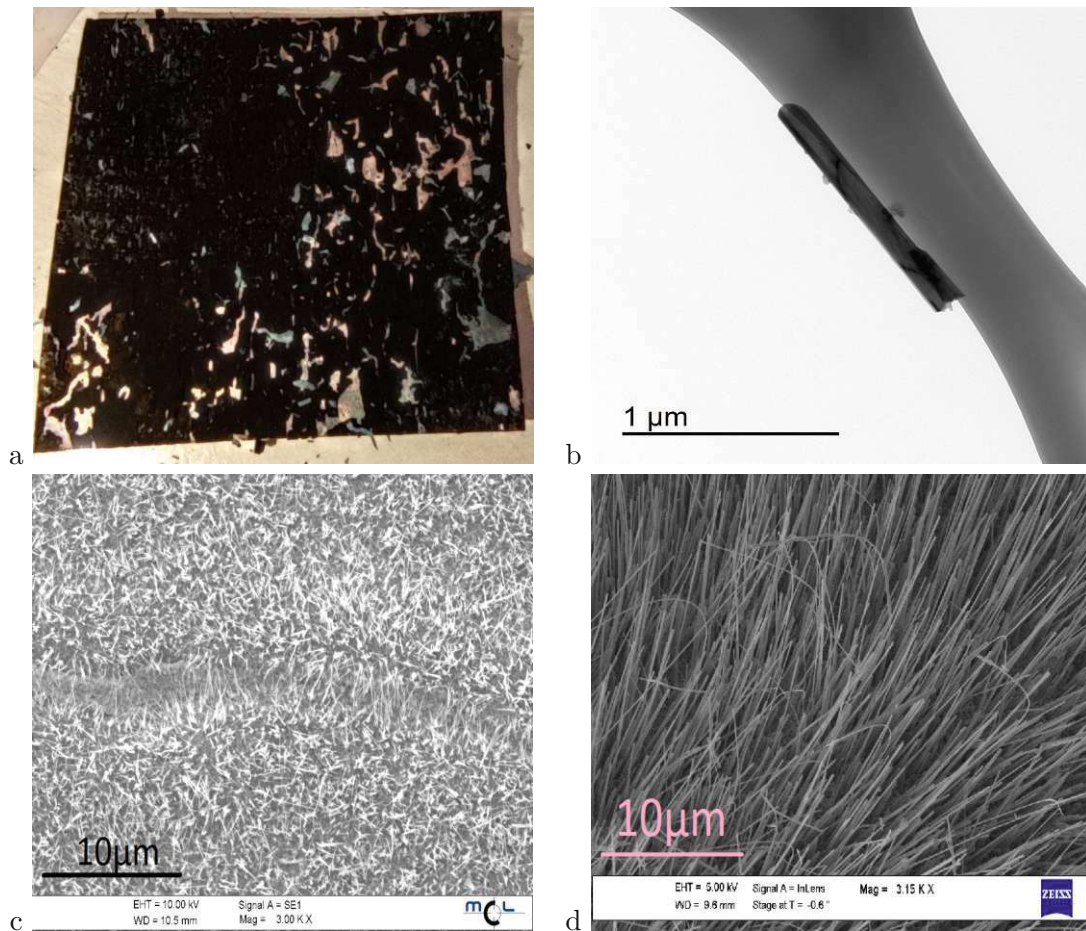
Figure 3.1: a) Picture of an oxidized Cu foil, b) CuO nanowire transferred from the oxidized copper foil onto a TEM Ni grid, c-d) SEM pictures of CuO nanowires grown on Cu foil.

The types of synthesized CuO nanostructures can be very different: flake-like nanoparticles [200], nanotubes [201], nanoneedles [202] and flower-like structures [203] are some of them. CuO nanowires used in this work were produced by thermal oxidation, which is a simply and hence widely used method reported in literature. [204] First a copper foil (≥99.8% purity, 0.1 mm thick, Sigma-Aldrich) was cut into 1x1cm pieces and then cleaned by rinsing the foil in hydrochloric acid (1M) and water three times for 10s. This step removed all contaminations and passivation oxide layer from the metal foil [205]. Then the foil was placed inside a tube furnace and heated up to 500°C for 4h in ambient air. After the annealing process the sample was left in the furnace to cool down. The samples appear black after the oxidation process. This black layer consists of densely grown CuO nanowires on top of the Cu foil (see Fig. 3.1).
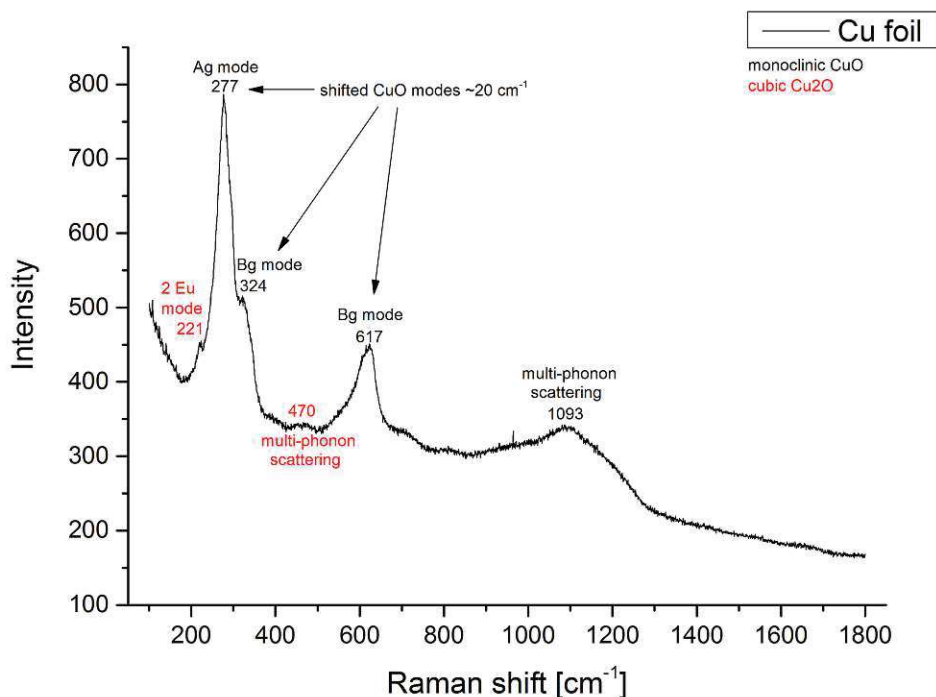
Figure 3.2: Raman spectrum of CuO nanowires on Cu foil, black marks are for CuO and red marks for Cu_2O.

The CuO nanowires on Cu foil were investigated by Raman spectroscopy (see Fig. 3.2). The Raman spectrum shows three major peaks, which can be attributed to CuO (black)

and one peak from Cu_2O (red). The phonon modes from CuO are A_g (277cm^{-1}), B_g (324cm^{-1}) and B_g (617cm^{-1}), all shifted by ~20cm^{-1} in comparison to the bulk CuO to the lower wavenumbers region [206]. The shifts can be related to the size effect - nanowires morphology can confine the lattice vibration in the crystal structure [207]. The Cu_2O peak is visible due to the mechanism of CuO nanowires growth. First the Cu_2O layer grows on the Cu foil and then the thin CuO layer on top of the Cu_2O. The strain induces a 1D growth and nanowires are grown from the CuO layer [204].

The growth of CuO nanowires was also investigated by XRD. The in-situ measurement was performed in ambient air and with help of a heater. The Cu foil was placed on a Si substrate and then heated to 500°C (this temperature was accomplished after around 4 h). The XRD spectrum was recorded almost every half of an hour (see Fig. 3.3).

The XRD spectra changes with time - copper peaks (marked with cyan lines) are getting smaller with increasing temperature and oxides peaks (blue and red lines) are arising around 400°C. This result is consistent with the mechanism of CuO nanowires growth, which was described in Raman spectrum analysis and also shown in Fig. 2.9.
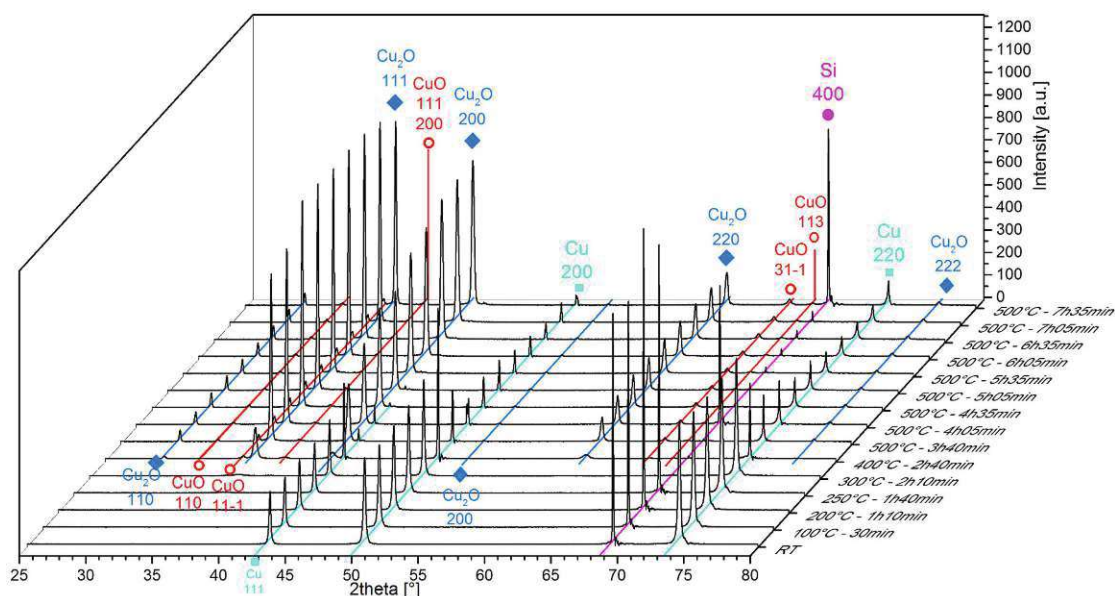
Figure 3.3: CuO nanowires growth - in-situ XRD investigation.

3.1.3   Tin (IV) oxide

Tin (IV) oxide is an n-type semiconductor with a band gap of 3.6 eV in bulk. [208] It can be applied not only in gas sensing [209], but also in lithium ion batteries [210], solar cells [211] and photocatalysis [212]. Different morphologies of SnO_2 1D nanostructures (beside

0D - nanoparticles and 2D - nanosheets [213]) can be obtained: nanowires/nanorods [214], nanobelts [215] and nanotubes [216].
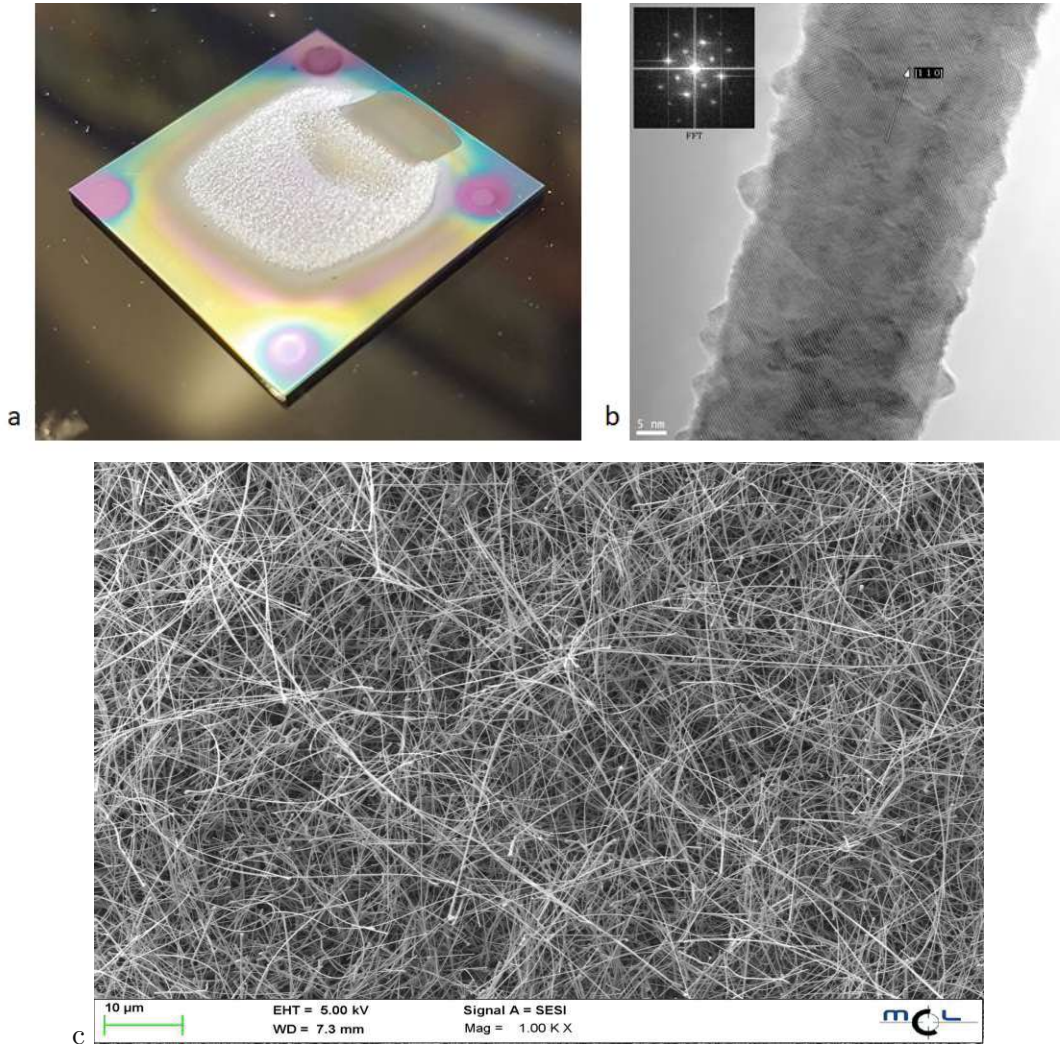
Figure 3.4: a) Picture of a white 'mold-like' structure of SnO_2 nanowires, b) TEM picture of a single SnO_2 nanowire, and c) SEM picture of SnO_2 nanowires.

SnO_2 nanowires used in this work were produced by a two-step synthesis. First step is coating of two different 2x2cm^2 sized silicon substrates with two different layers: one substrate ("donor substrate") has been coated with a 400 nm SnO_2 layer by spray pyrolysis technique, the second substrate ("catalyst substrate") has been coated with a 40 nm sputter deposited Cu layer. Those two substrates were mounted "face-to-face" to each other with a spacing in between of 2-5 mm and put into a tube furnace. Next, an annealing process is performed at a temperature of 900°C for 3h in Ar-atmosphere.

After annealing the sample stack was left in the furnace to cool down. A white 'mold-like' appearing structure of SnO_2 nanowires was found on top of the Cu sputtered sample (see Fig. 3.4a). The catalyst substrate can be coated also with other metals, like gold or combinations of Au and Cu - in the next chapter those metals were used for structured nanowires growth (see Fig. 3.16).

3.1.4 Tungsten (VI) oxide

Tungsten (VI) oxide is an n-type semiconductor with a band gap of 2.4 eV in bulk (for monoclinic structure). [217] The monoclinic structure is a stable phase below 320°C and an orthorhombic structure above this temperature. [218] WO_3 applications, beside gas sensing [219], are UV photodetectors [220], photocatalysts [221] and electrochromic devices [222]. Different morphologies can be obtained: urchin-like structures [223], nanorods [224], nanoplates or nanospheres [225].
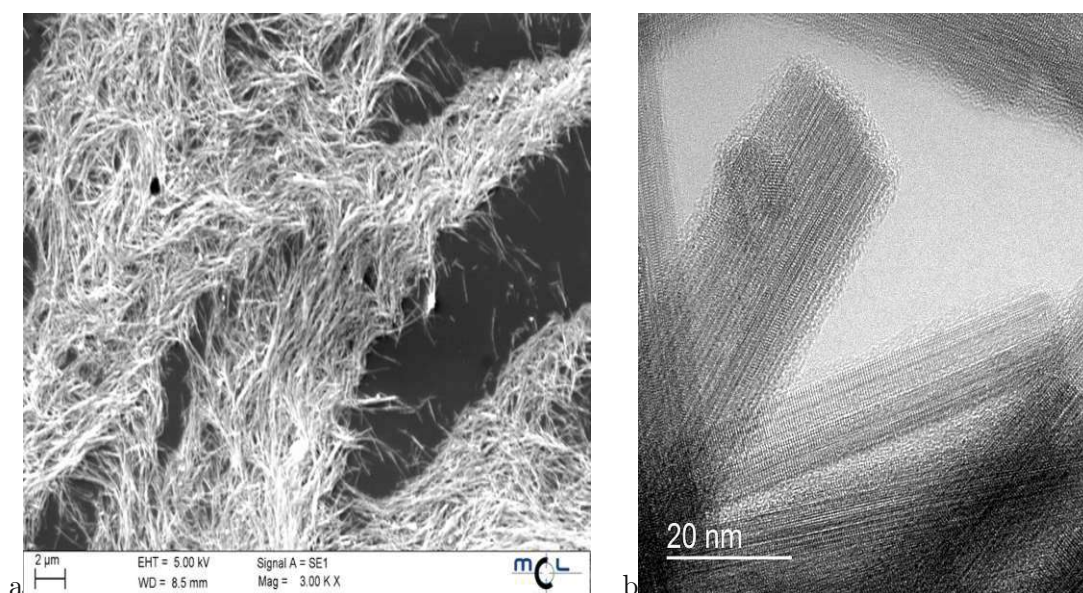
Figure 3.5: a) SEM picture of WO_3 nanowires, and b) TEM picture of single WO_3 nanowires.

The WO_3 nanowires used in this work were produced by hydrothermal synthesis. First 0.85g of tungstic acid H_2WO_4 (Sigma Aldrich) was stirred in 30 ml of deionised water until homogeneously distributed. Second 40g of potassium sulphate K_2SO_4 (Sigma Aldrich) was added spoon by spoon and mixed carefully for approximately 5 min until a smooth paste was formed. The paste was placed in the autoclave, and the autoclave was left in a furnace for 12h at 180°C. The autoclave was left to cool down naturally and the

powder-like product was then washed with deionized water and ethanol until complete removal of potassium sulphate. The resulting nanowires were in form of big bundles of nanowires of 10-30 nm in diameter and the length of $1-10$ µm (see Fig. 3.5). The details about the structure and using of tungsten oxide nanowires in gas sensors (inkjet printer, wet process) are presented elsewhere. [226] Fig. 3.5a and 3.5b shows a SEM image of bundles of nanowires and TEM image of a few single WO_3 nanowires, respectively.

3.2 Application of transfer methods

3.2.1 Transfer of nanowires

The integration of MOx nanowires into an assembly, which enables electrical gas sensing, was the most critical step to realization of multi-nanowire sensors. From the diverse transferring methods shown in Tab. 2.5, the dry transfer method with a stamp/tape was chosen to minimize the use of liquids and due to its simplicity and cheapness. Four transfer media were chosen for this work (see Fig. 3.6):

- A Scotch 810 3M tape

- A polydimethylsiloxane (PDMS) self-produced stamp

- A Blue Low Tack Tape (P/N 18733, Schubert Technologies, Germany), and

- A Thermal Release Tape (Revalpha RA-98L(N), Semiconductor Equipment Corp.)
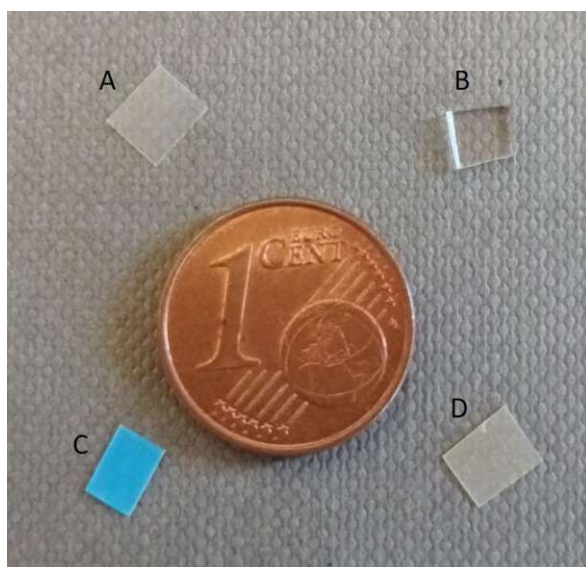
Figure 3.6: Different media for dry transfer process, 1 eurocent for size comparison: A - Scotch 810 3M tape, B - PDMS stamp, C - Blue Low Tack Tape, and D - Thermal Release Tape.

While the tapes were commercially available products, the polydimethylsiloxane (PDMS) was prepared by a standard Dow Corning Sylgard 184 recipe. An elastomer and a curing agent were mixed with a 10:1 weight ratio and then put into a desiccator for around 5 min. The mixture was carefully applied on a glass substrate to receive a smooth surface of a PDMS stamp and then cured at 100 °C for 1 h. The part of a resulting polymer was then crumbled and added to KBr powder to create a pellet suitable for transmission

measurements for checking the IR spectrum (Nicolet Avatar 320 FT-IR spectrometer) of the produced PDMS stamp (see Fig. 3.7). The result is in good agreement with results reported in the literature. This indicates that the PDMS stamp produced in this work is of high quality and purity.
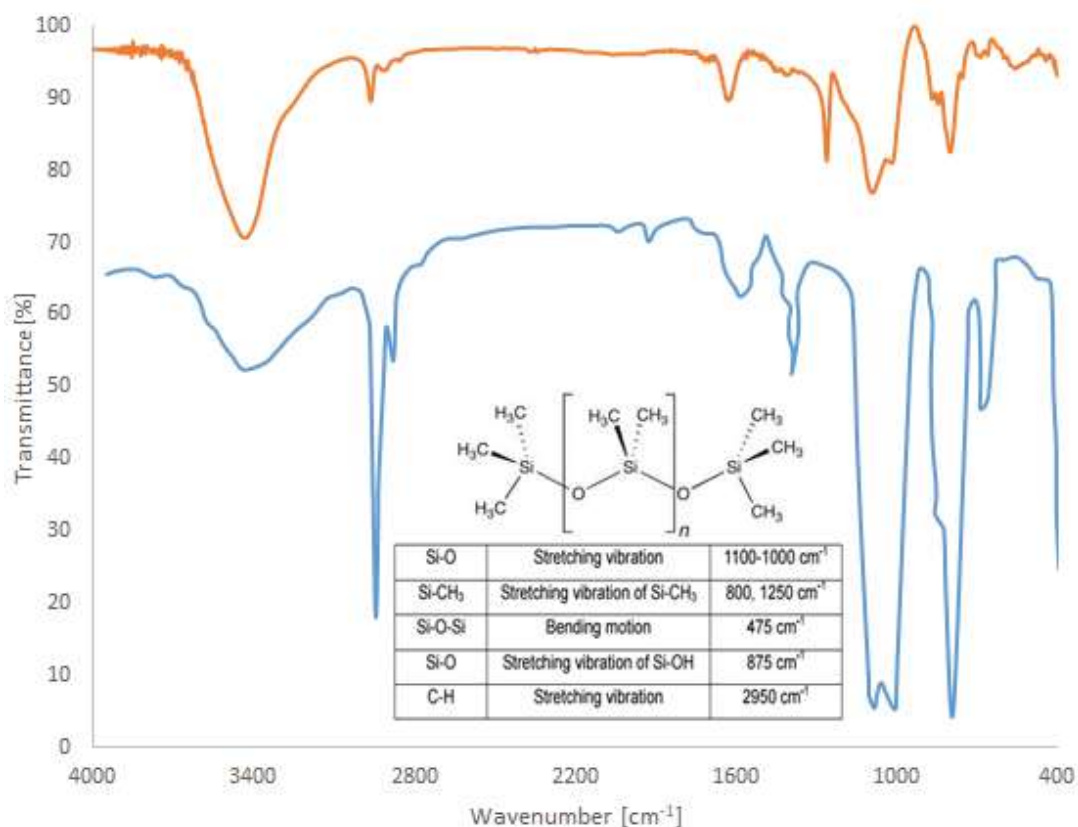
Figure 3.7: IR spectra of PDMS in comparison with literature (blue - literature [227]).

First the transfer process was performed from silicon to silicon substrates - to test which transfer media gives the best results. The methodology of the transfer process was presented in Fig. 3.8. Afterwards, for realization of a practical gas sensor device, the nanowires were transferred onto specific substrates with inter digitated electrodes (IDE, gold or platinum), which enabled electrical connections to the nanowires. The following substrates were used for nanowire implementation:

1. Silicon substrates with Au-IDES fabricated by photolithography, evaporation and Lift-off (Si-based devices), and assembled into a gas sensing device with use of external heaters (more details in Chapter 3.3.1)

2. Commercial SiN-micro-hotplate based sensor platforms (APPS - Applied Sensors GmbH, now ams OSRAM AG) with IDE and a microheater beneath the electrode structure, assembled into a DIL package (more details in Chapter 3.3.1)

3. CMOS integrated microhotplate chip (hereafter designated as MPW4) with Au-IDES fabricated by photolithography, evaporation and Lift-off in post-processing, glued and bonded onto a PCB carrier (more details in Chapter 3.3.1)

The transfer scheme for the PDMS stamp and tapes is presented in Fig. 3.9. The thickness of the stamp is approximately 2 mm, thickness of the tapes is 0.06mm for Scotch 810 3M tape), 0.08mm for Blue Low Tack Tape, and 0.158mm for Thermal Release Tape.
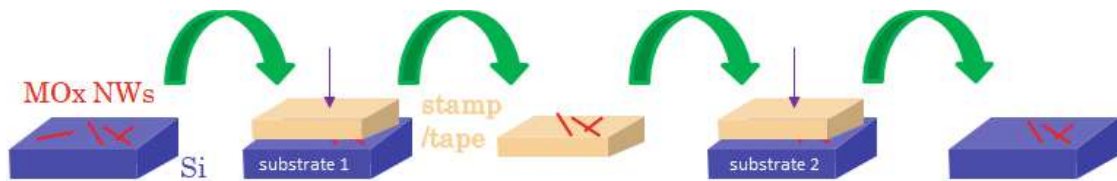
Figure 3.8: Scheme of dry nanowire transfer processes.
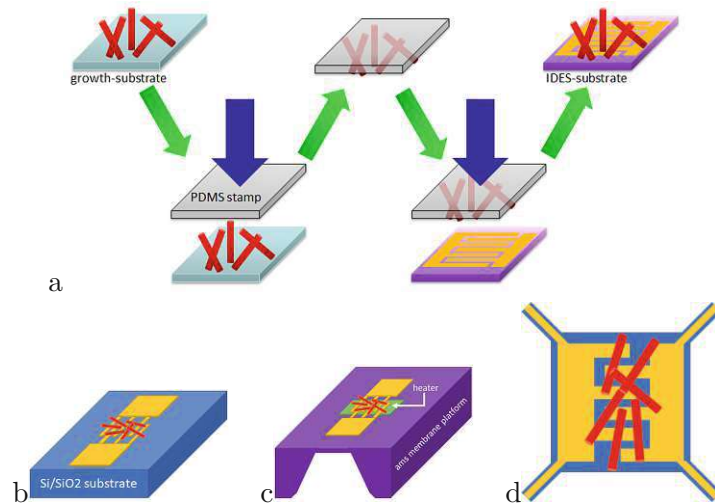
Figure 3.9: a) A scheme of PDMS-based nanowire transfer on IDE structures (presented also in [228]) and a scheme of IDE structures (b - on a silicon based device, c - on a APPS chip, d - on one of the microheaters of the MPW4 chip) with MOx nanowires on it.

51

3.2.2 Manual transfer of metal oxide nanowires - copper (II) oxide

The transfer process of the CuO nanowires was performed by first pressing the 5x5mm^2 sized stamp/tape to the oxidated copper substrate - to harvest the nanowires from the growth substrate ("donor substrate"). Second step was to press the stamp/tape with the nanowires to the final substrate, to deposit the nanowires directly onto the desired region (see Fig. 3.8). The representative qualitative pictures of the silicon (final) substrates with the transferred CuO nanowires are presented in Fig. 3.10.
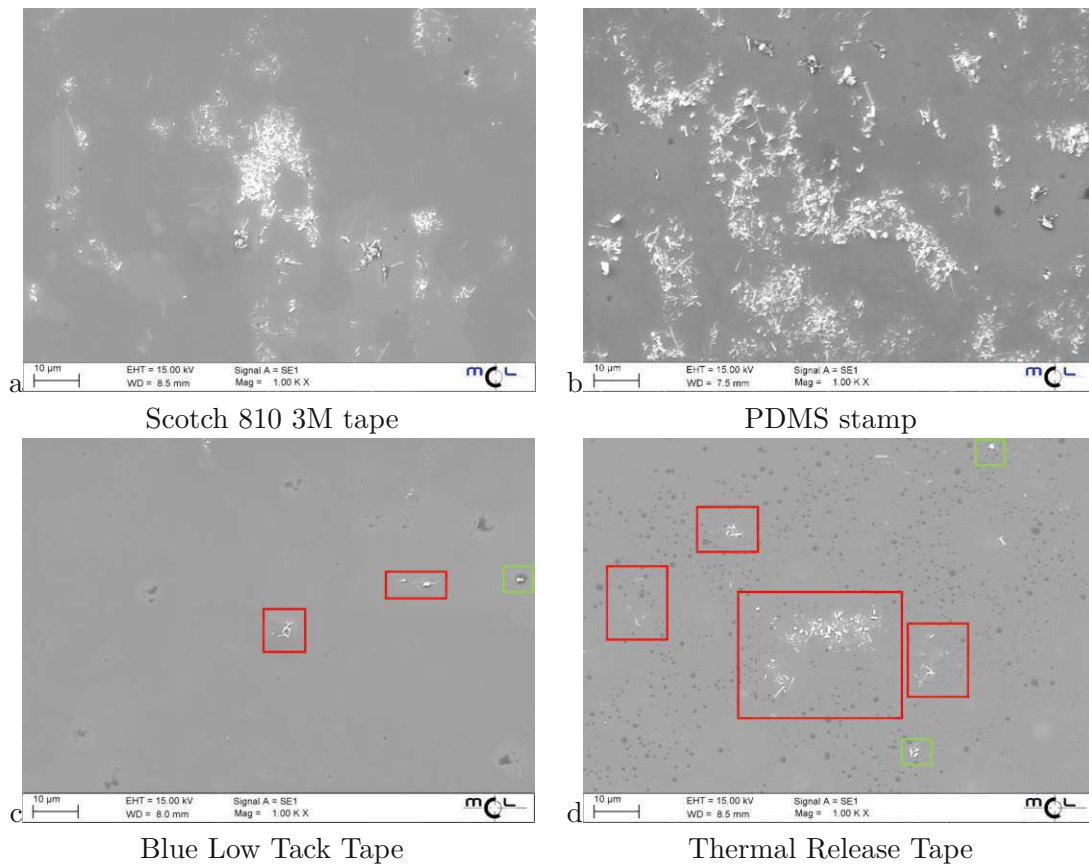
Figure 3.10: CuO nanowires transferred from the oxidized copper foil with dry transfer methods.

The Scotch 810 3M tape has transferred some groups of nanowires (Fig. 3.10a). The PDMS stamp was able to transfer the biggest amount of nanowires in comparison with

other transfer methods (Fig. 3.10b). The Fig. 3.10c shows the final substrate after CuO nanowires transfer with the Blue Low Tack Tape. This tape has transferred a few nanowires onto the final substrate (only the ones in the red squares were found) , and some bigger microcrystals (in the green square). The Thermal Release Tape (Fig. 3.10d) transferred more microcrystals/dirt (green squares) than nanowires (red squares, mostly microcrystals connected with nanowires) and some residues from the tape itself (round structures over the whole final substrate). The best results of the dry transfer process was obtained for the PDMS stamp. Hence, this method was used afterwards to transfer the nanowires on the gas sensing devices with gold IDE structure. Unfortunately, the as-transferred nanowires were too short to make connection between the electrodes (see Fig. 3.11), because the nanowires break during the "pick-up" process.
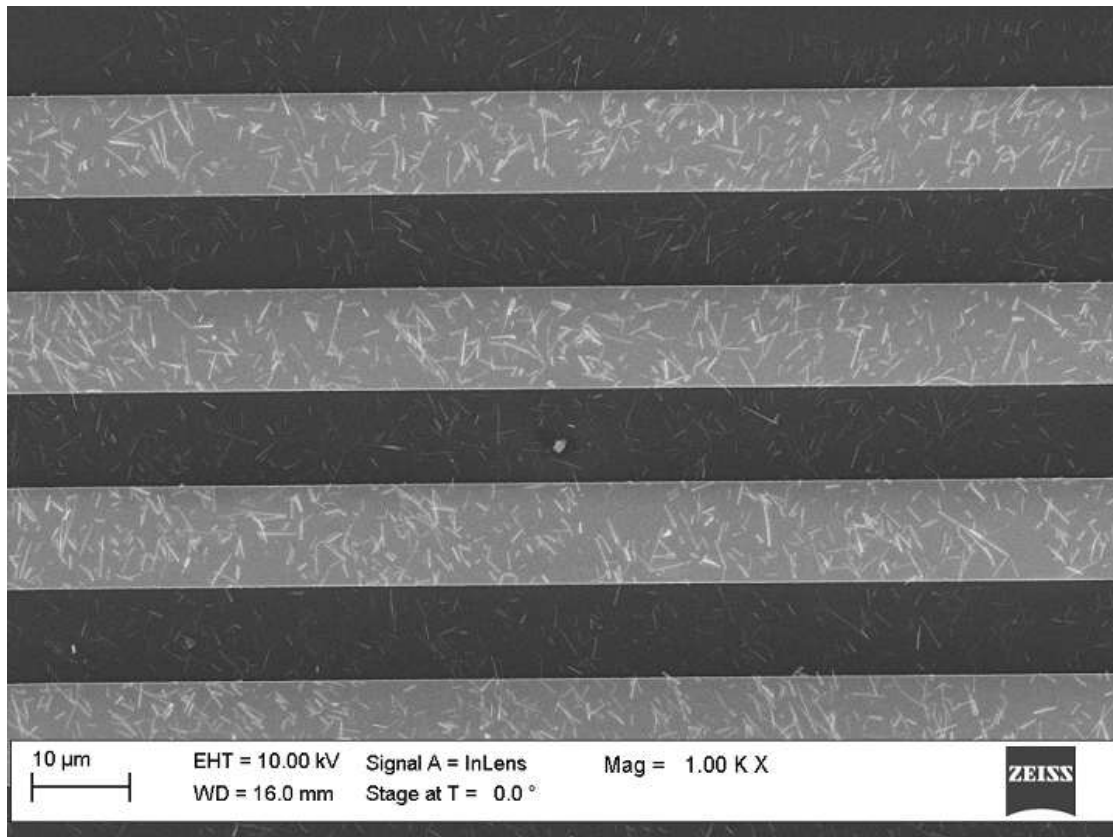
Figure 3.11: CuO nanowires on top of the IDE structure.

3.2.3   Manual transfer of metal oxide nanowires - tin (IV) oxide

Similar experiments as for the CuO nanowires were performed also for SnO_2 nanowires - with all types of tapes/stamps. First the donor substrate with SnO_2 nanowires was put into an isopropanol solution and the nanowires were harvested by an ultrasonic bath for 5 minutes. Then 4 silicon substrates were drop-coated with this solution (50µl per sample) and left to dry. Afterwards SEM pictures and 4 FIB markers on those 4 samples were performed (see 3.13a, inside violet crosses). The next step was the nanowires transfer, which was accomplished onto 4 silicon substrates by the four media mentioned in the previous chapter (Scotch 810 3M tape - see Fig. 3.12a, PDMS stamp - see Fig. 3.13b, Blue Low Tack Tape - see Fig. 3.14c and Thermal Release Tape - see Fig. 3.15d). After the nanowires transfer the substrates were again investigated in SEM and the places with FIB markers were compared before and after transfer. Additionally the substrates with transferred nanowires (named as substrate 2) were also investigated to evaluate if the transfer was successful:

- The Scotch 810 3M tape has transferred a few single nanowires and has left glue residues on substrate 1.

- The PDMS stamp was able to transfer the biggest amount of nanowires.

- The Blue Low Tack Tape has transferred the most nanowires from substrate 1 but there were a few single nanowires on substrate 2 (red square) and some microcrystals (green square).

- The Thermal Release Tape transferred only some microcrystals (green squares, additionally no nanowires were found on substrate 2), and some residues from the tape itself were present both on substrate 1 and substrate 2.

Again, the best result was achieved with the PDMS stamp - similarly to the CuO nanowires.

Substrate 1 before transfer

Substrate 1 after transfer

Substrate 2 with transferred nanowires
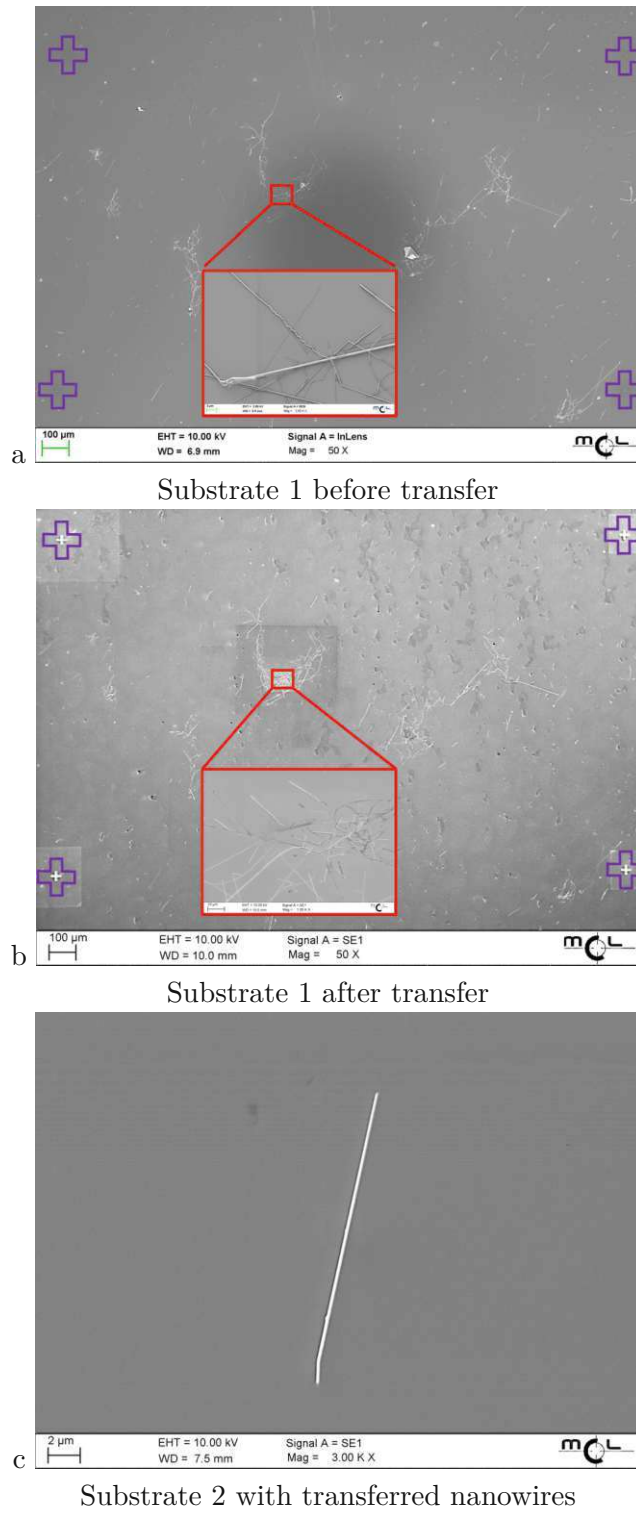
Figure 3.12: SnO$_2$ nanowires transferred with a Scotch 810 3M tape.

Substrate 1 before transfer

Substrate 1 after transfer

Substrate 2 with transferred nanowires
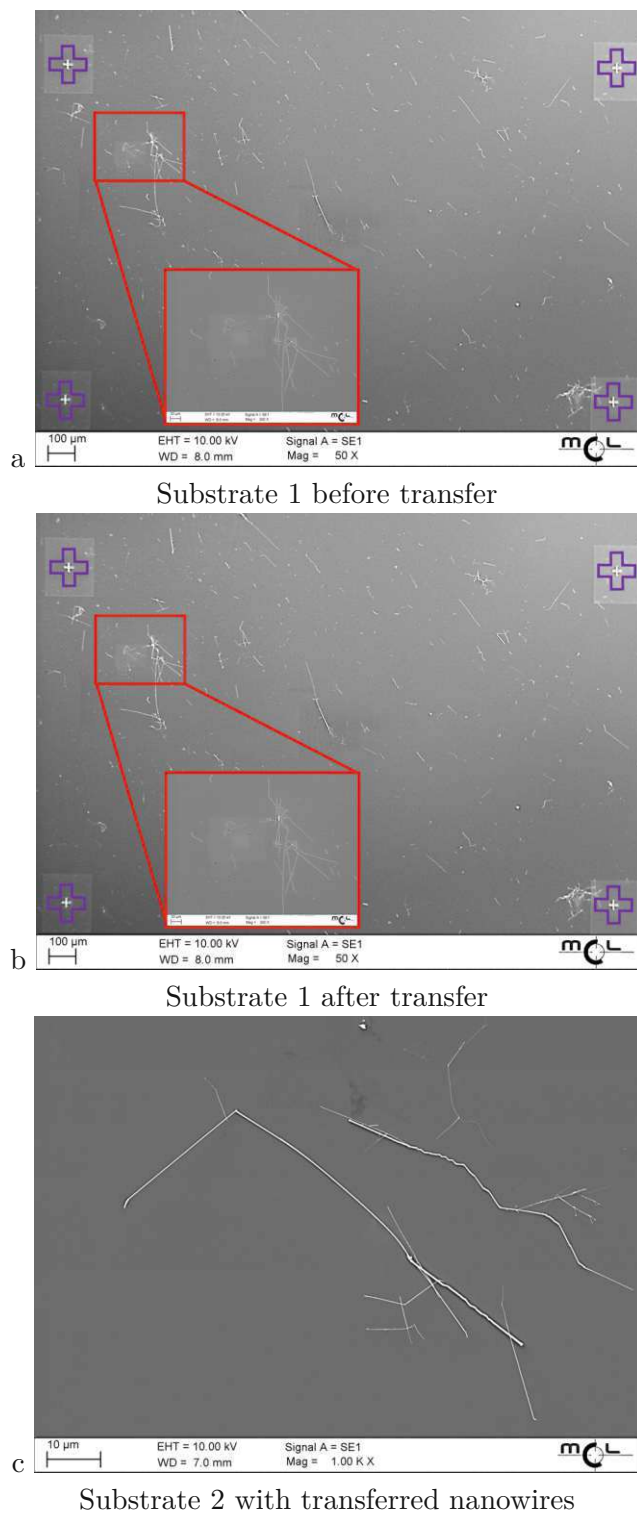
Figure 3.13: SnO$_2$ nanowires transferred with a PDMS stamp.

a

Substrate 1 before transfer

b

Substrate 1 after transfer

c

Substrate 2 with transferred nanowires
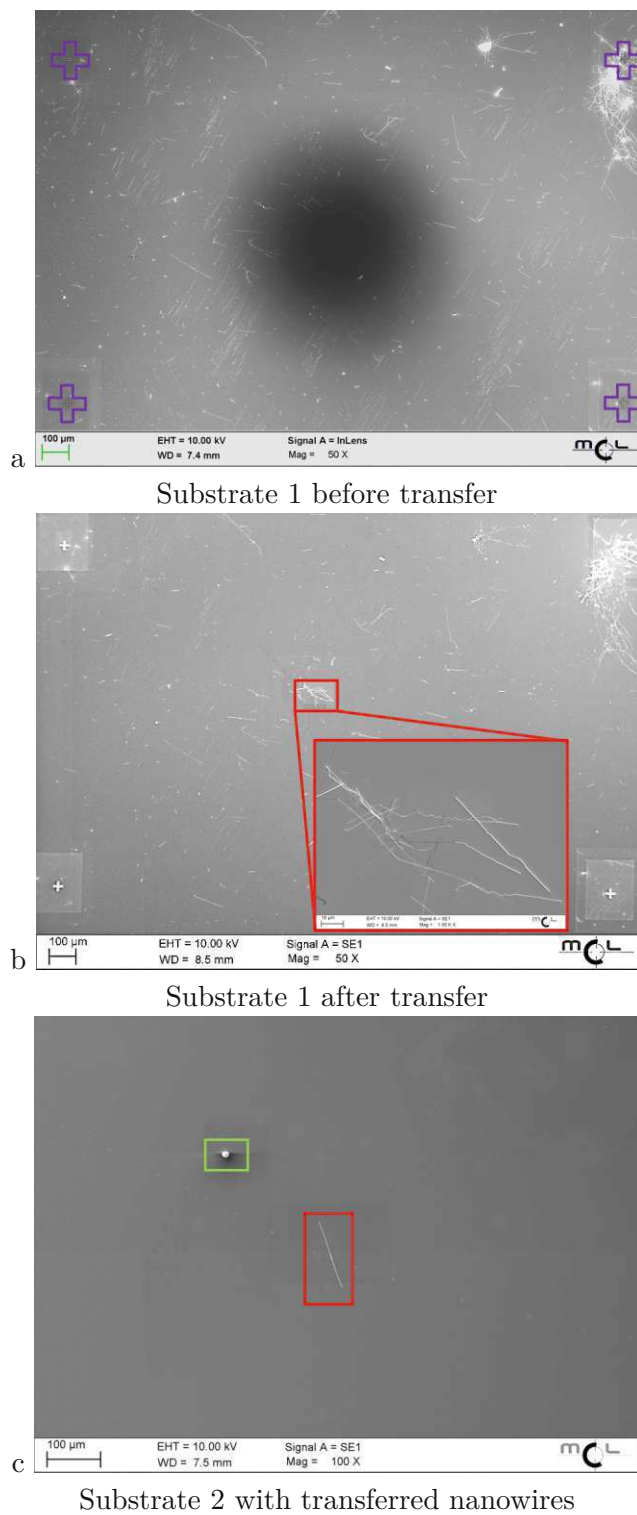
Figure 3.14: SnO$_2$ nanowires transferred with a Blue Low Tack Tape.

57

Substrate 1 before transfer

Substrate 1 after transfer

Substrate 2 with transferred nanowires
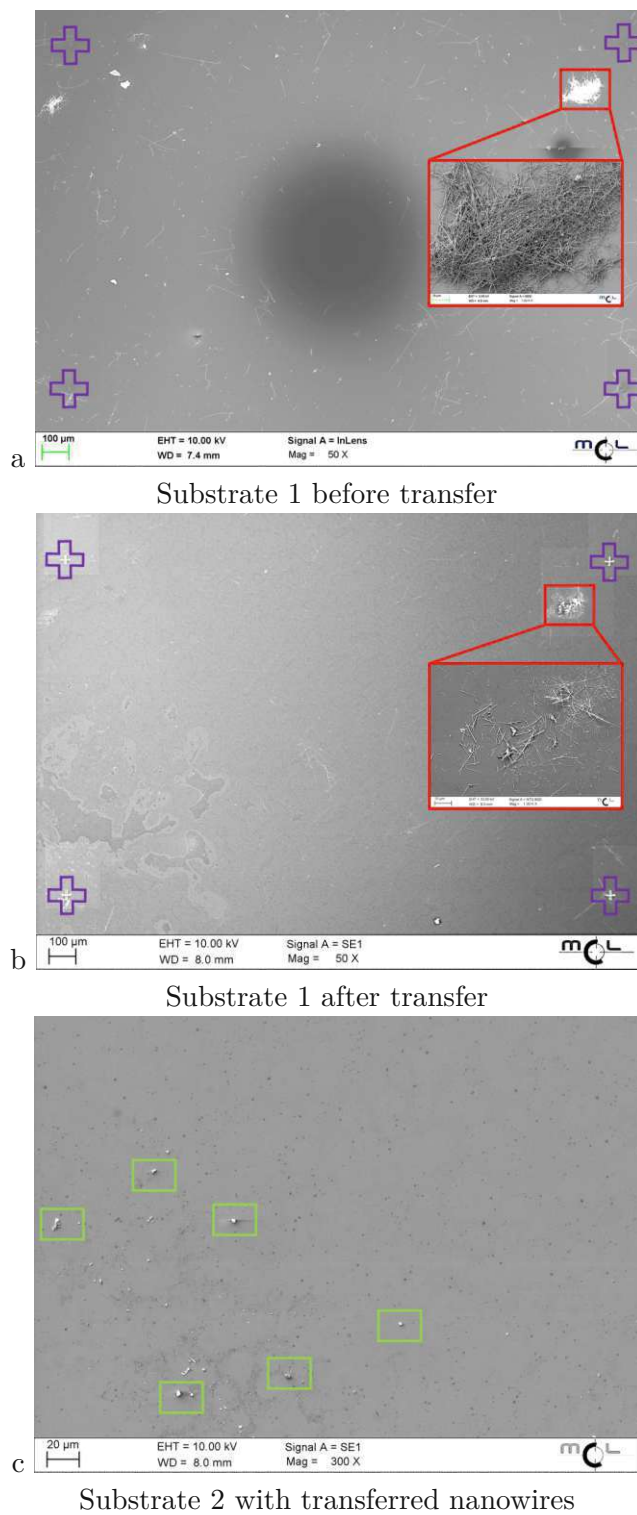
Figure 3.15: SnO$_2$ nanowires transferred with a Thermal Release Tape.

The SnO$_2$ nanowires growth, where the nanowires are synthesized on the whole surface, was described in 3.1. We have also performed nanowire synthesis on a substrate, where the catalyst Cr/Au/Cu was structured by means of photolithography, evaporation, and lift-off. As a result, the nanowires are synthesized on well-defined locations. Such a local growth can be very favorable when transferring the nanowires to a corresponding electrode structure. With this approach it should be feasible to reproduce multi-nanowire based sensor devices. Fig. 3.16a shows the nanowires grown on the structured catalyst donor substrate: it is obvious that the nanowires are exclusively on the catalyst. Fig. 3.16b shows the nanowires after being transferred on the final substrate, and demonstrates that the initial structure was well reproduced by the PDMS transfer process (see Fig. 3.16a and b).

The structure was well reproduced by the PDMS transfer process (see Fig. 3.16a and b).
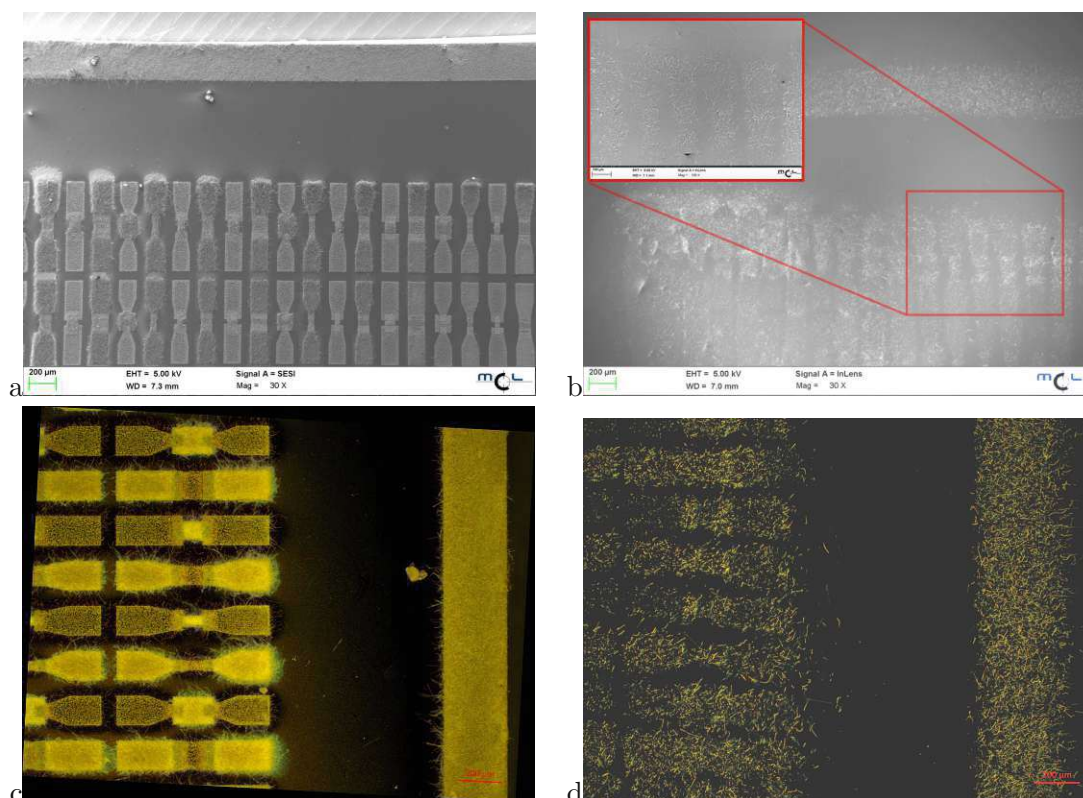
Figure 3.16: a,c) SnO$_2$ nanowires grown on structured Cr/Au/Cu catalyst donor substrate, and b,d) nanowires transferred on a Si substrate with PDMS stamp.

Characterization of the SnO$_2$ and CuO nanowires was performed by means of Atomic Force Microscopy (AFM), which was implemented in a SEM (BRR 2770 from DME, SEM-FIB Auriga 40 from Zeiss). Both types of semiconducting nanowires were transferred directly from their donor substrates (for CuO nanowires - oxidized Cu foil and for SnO$_2$ nanowires - Cu-sputtered substrate after SnO$_2$ nanowires synthesis in a tube furnace) with a PDMS stamp onto a silicon sample with platinum electrodes. The SEM was first used to localize the nanowires, nest the AFM was used to measure the topography of the nanowires (see Fig. 3.17a-d). The CuO nanowires were found to be 1-2 µm long and 16-130 nm was their diameter. The SnO$_2$ nanowires were much longer - from 2 to even tens of µm long and 70-250 nm in diameter. More details can be found in [229].

CuO nanowires
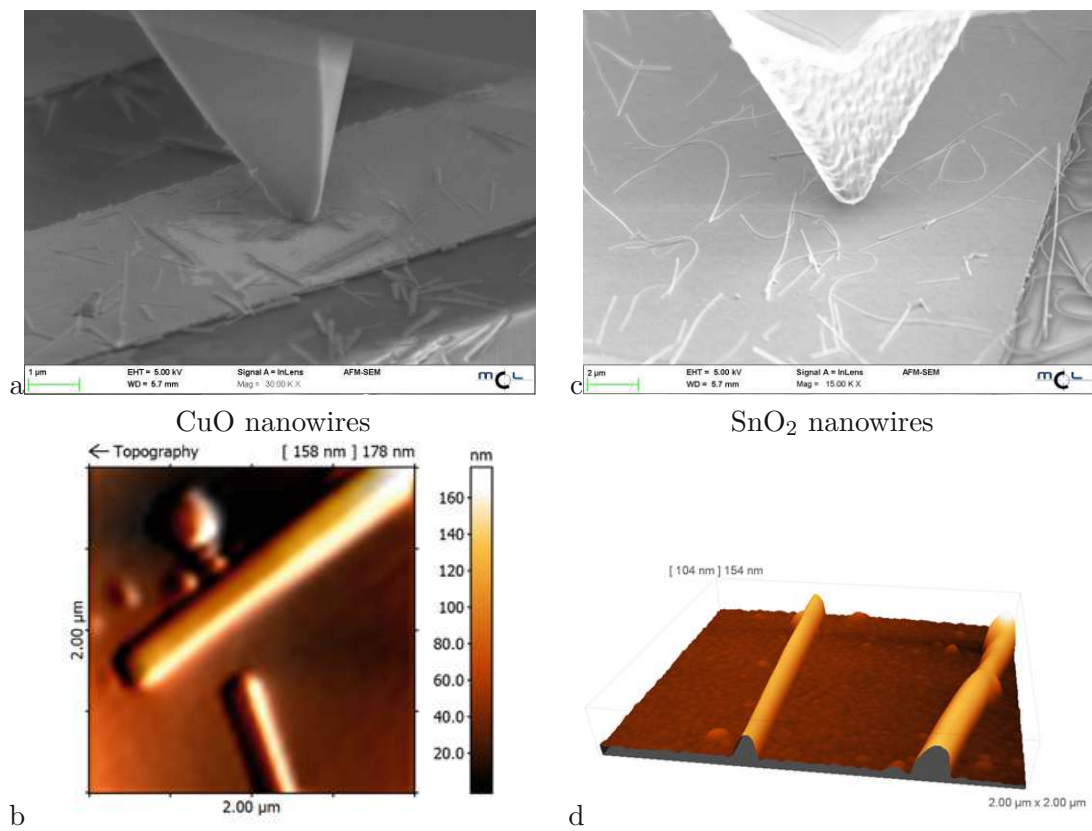
SnO$_2$ nanowires

Figure 3.17: SnO$_2$ and CuO nanowires - AFM in SEM measurements.

Finally, for realization of a gas sensor, the SnO$_2$ nanowires were transferred directly from a growth (donor) substrate onto Si-based devices with either gold IDE structure (see. Fig. 3.18) or on Pt-IDE structure on top of a SiN-membrane based micro-hotplate chip (see APPS, Chapter 3.3.1). In both configurations the nanowires interconnect the

fingers of the IDE structure and enable use of nanowires as sensing elements for electrical measurements (presented in the next chapter - 3.3).
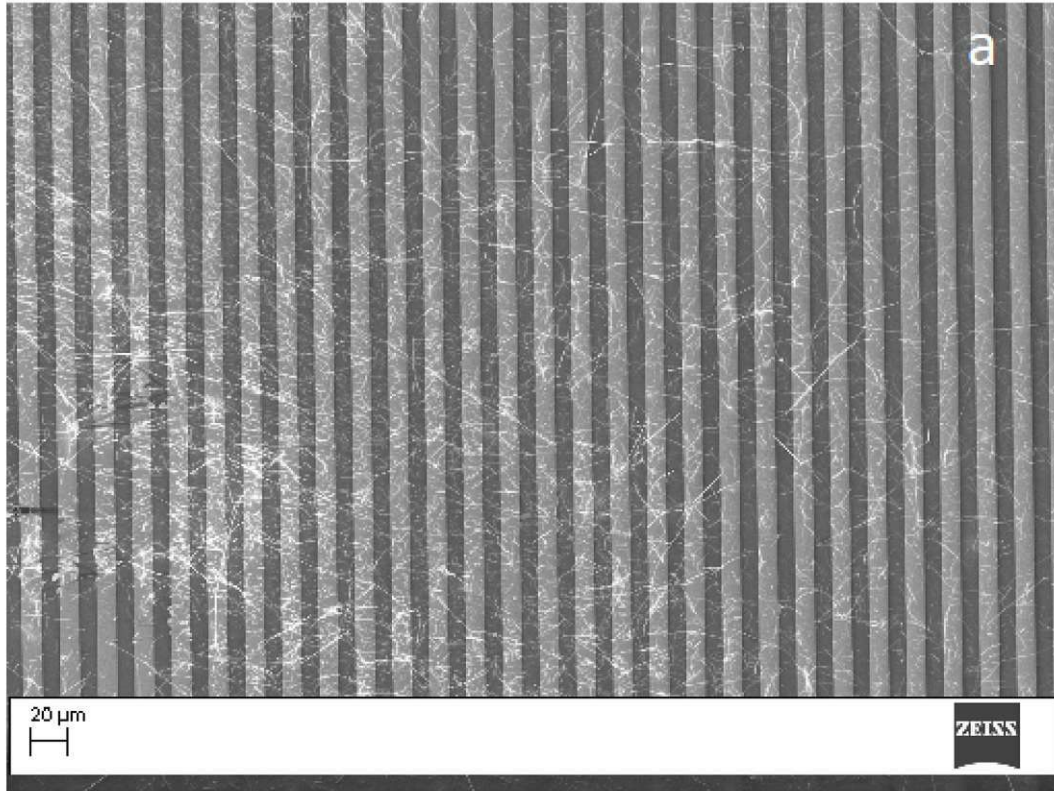
Figure 3.18: SEM picture of SnO$_2$ nanowires transferred on IDE structure of a Si-based sensor (presented also in [228]).

3.2.4 Manual transfer of metal oxide nanowires - tungsten (VI) oxide

Similar experiments as for the SnO$_2$ nanowires were performed also for WO$_3$ nanowires - with all types of tapes/stamps. This type of nanowire was synthesized by hydrothermal route, and after the synthesis the nanowires were suspended in water. Then silicon donor substrates (size 2x2cm^2) were drop-coated by the nanowire solution. Subsequently, the nanowires were transferred from these donor substrates onto desired samples or devices. For testing the transfer process, the procedure was similar to the one used for the SnO$_2$ nanowires - four FIB markers on silicon substrates before the nanowires transfer were produced (see Fig. 3.19a, inside the violet crosses). The SEM pictures were performed before and after nanowires transfer. The nanowires transfer was accomplished by four media mentioned in the previous chapter (Scotch 810 3M tape - see Fig. 3.19a, PDMS

stamp - see Fig. 3.20b, Blue Low Tack Tape - see Fig. 3.21c and Thermal Release Tape - see Fig. 3.22d).

After transfer the substrates were investigated in SEM and the locations with FIB markers were compared before and after transfer. Additionally the substrates with transferred nanowires (named as substrate 2) were also investigated to evaluate if the transfer was successful. The Scotch 810 3M tape has transferred a lot of nanowires but also left some residues on substrate 2. Bigger agglomerates of the nanowires were transferred (green squares) as well as single nanowires. The PDMS stamp transferred only a few microcrystals (one qualitative example in Fig. 3.20b, inside a green square). The Blue Low Tack Tape has transferred most of the big structures, which are nanowire bundles (green squares). The Thermal Release Tape transferred no nanowires, only one microcrystal (green square) was found on the sample; and left some residues from the tape itself both on substrate 1 and substrate 2. The best result gave a Blue Low Tack Tape (P/N 18733, Schubert Technologies, Germany) transfer.

Substrate 1 before transfer

Substrate 1 after transfer

Substrate 2 with transferred nanowires
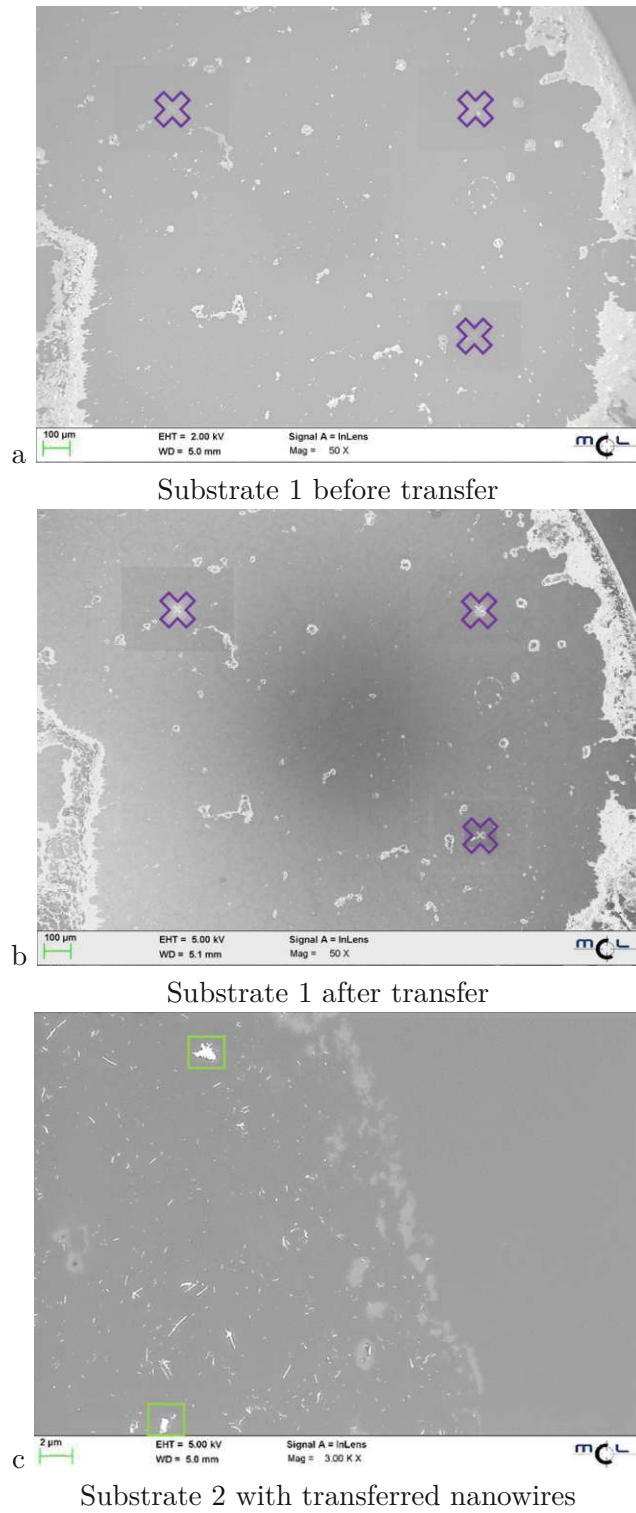
Figure 3.19: WO$_3$ nanowires transferred with a Scotch 810 3M tape.

a

Substrate 1 before transfer

b

Substrate 1 after transfer

c

Substrate 2 with transferred nanowires
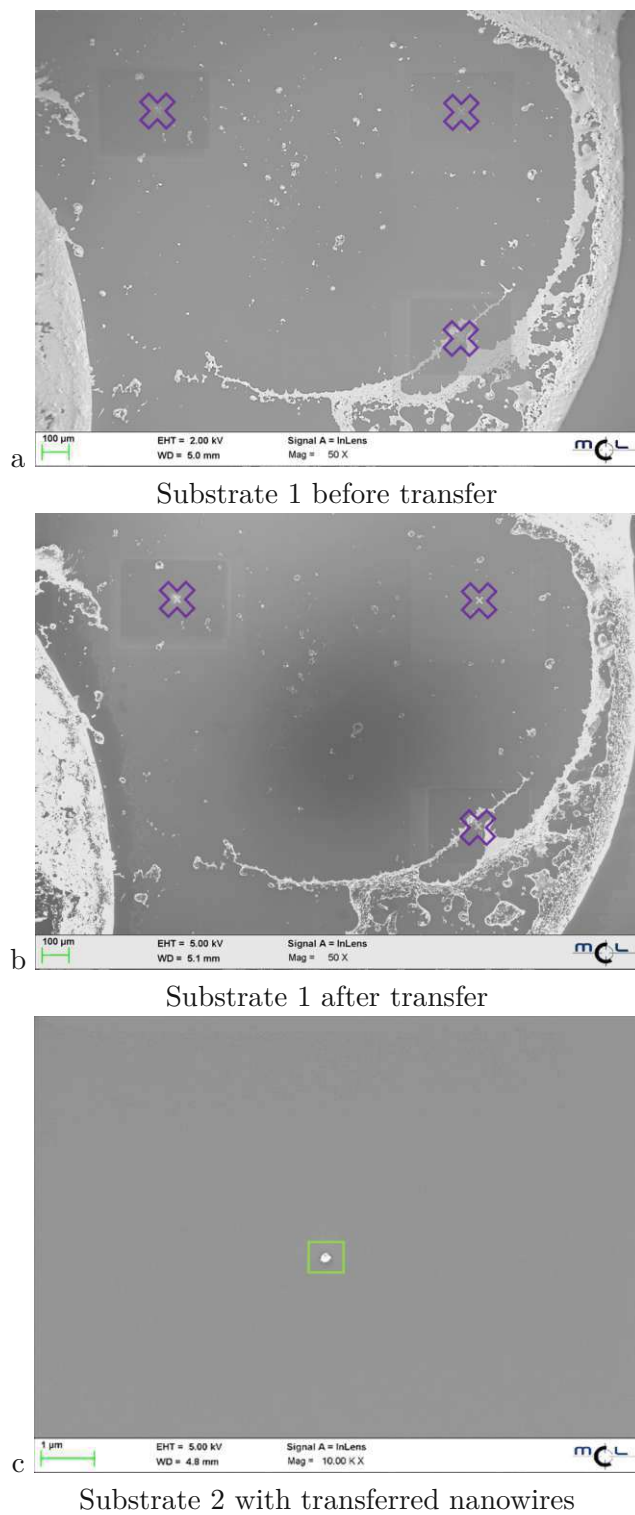
Figure 3.20: WO$_3$ nanowires transferred with a PDMS stamp.

64

a

Substrate 1 before transfer

b

Substrate 1 after transfer

c

Substrate 2 with transferred nanowires
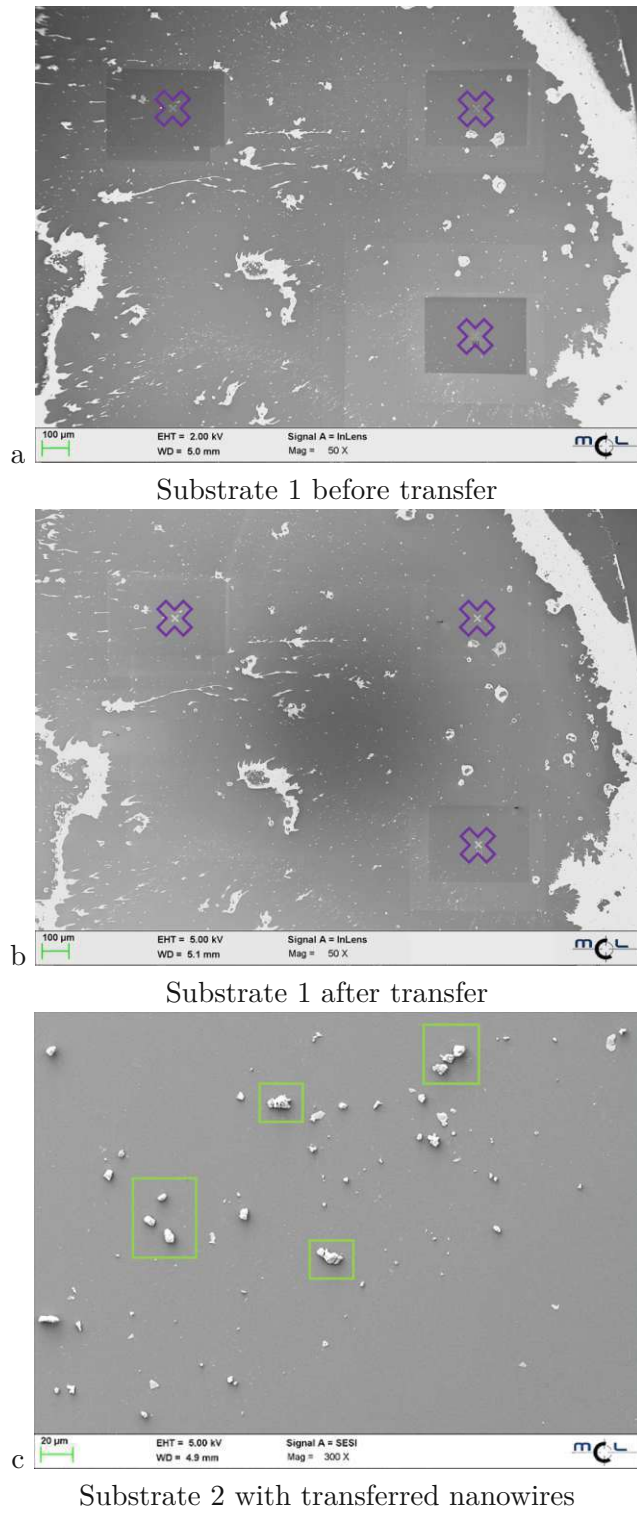
Figure 3.21: WO$_3$ nanowires transferred with a Blue Low Tack Tape.

a

Substrate 1 before transfer

b

Substrate 1 after transfer

c

Substrate 2 with transferred nanowires
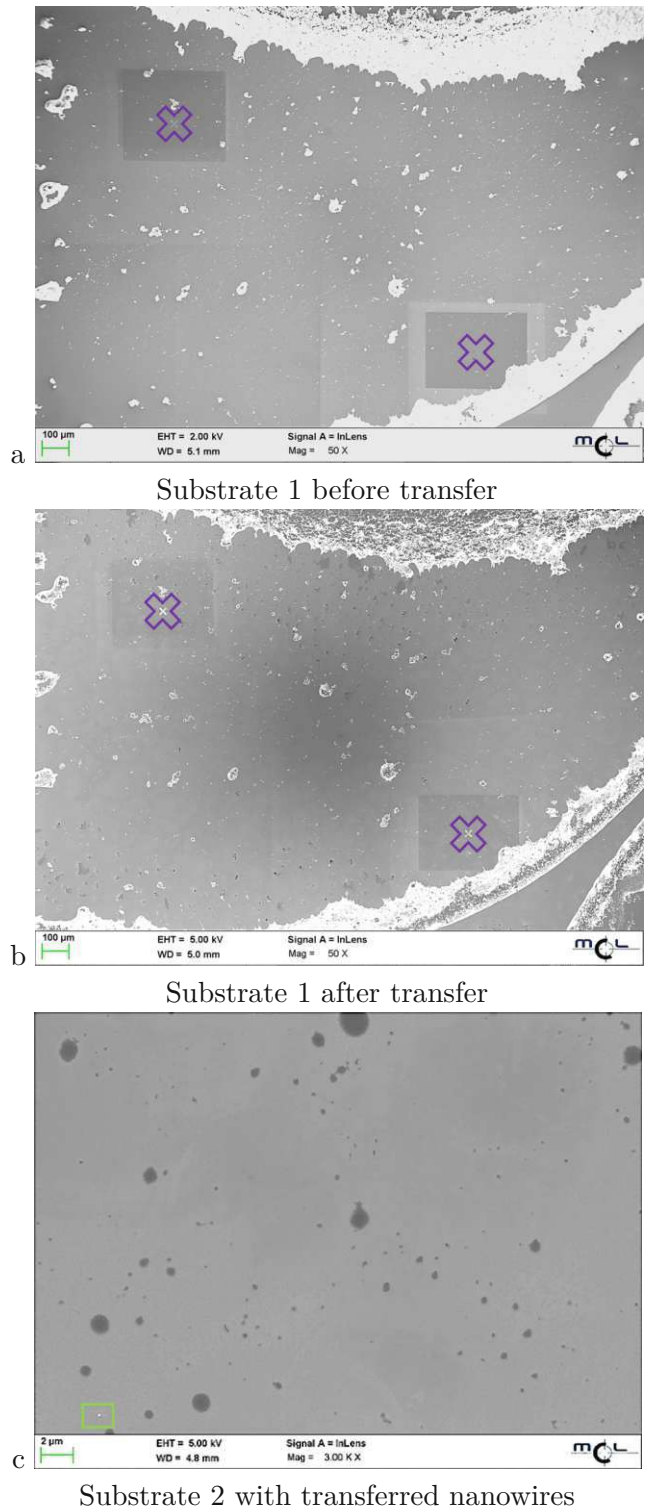
Figure 3.22: WO$_3$ nanowires transferred with a Thermal Release Tape.

The WO$_3$ nanowires were transferred with a Blue Low Tack Tape onto a gas sensing devices with gold IDE structure (see. Fig. 3.23). The resulting sensors could be electrically characterized, because also in this case the nanowires interconnect the fingers of the IDE structure.
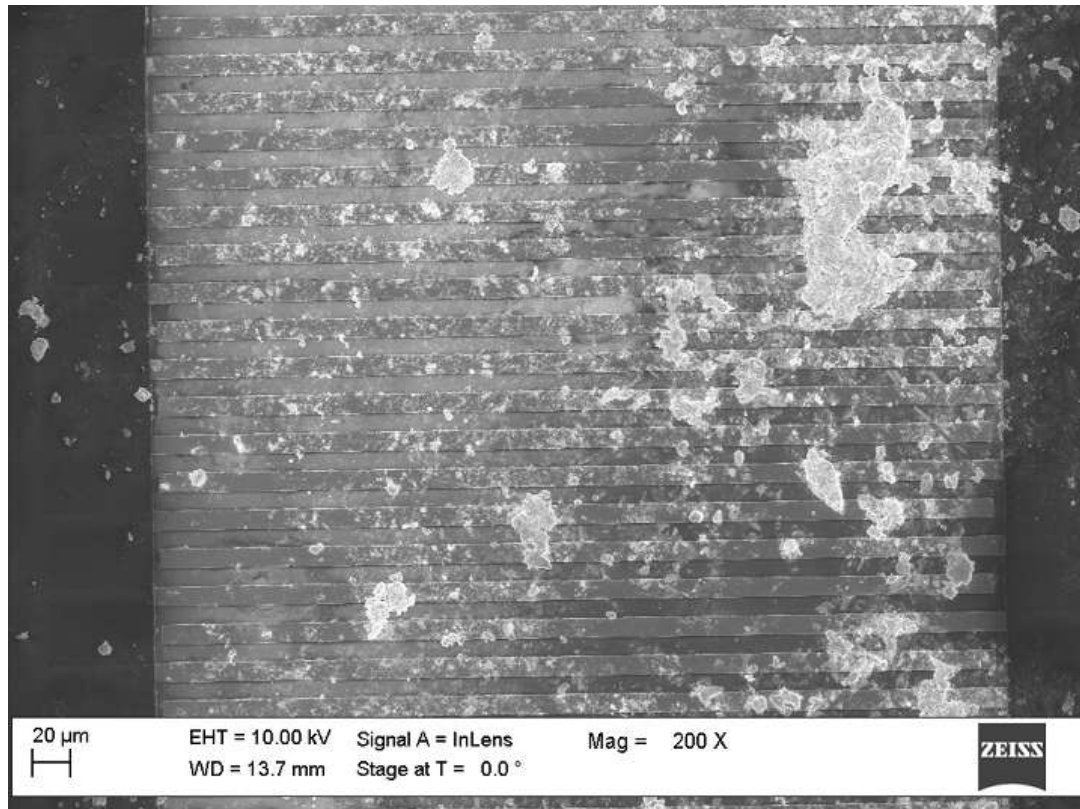
Figure 3.23: SEM picture of WO$_3$ nanowires transferred on IDE structure of a Si-based sensor.

3.2.5 Transfer of metal oxide nanowires - tin (IV) oxide - with a bond tester

In addition to the manual transfer, the possibility of using a machine for better controlled nanowire transfer has been tested. A XYZ-TEC Condor Sigma device was used for SnO$_2$ nanowires transfer.

Figure 3.24: XYZ-TEC Condor Sigma device - bond tester. Copied from: `https://www.xyztec.com/wp-content/uploads/2023/05/Sigma-lite-2022.png`.

This tool is usually employed to test the performance of wire bonds as used in semiconductor industry to electrically connect microchips with PCBs, lead frames, or specific sockets, such as the Kyocera KD-SB9F85 used in our setup. (e.g. see Fig. 3.36a). This tool enable pull tests as well as shear tests and features a movable head for the uptake of highly specifics microtools for bond testing. The movement can be precisely controlled along the Z axis in vertical direction. Additionally, there is a table, where the samples are placed, with controlled horizontal movements in X and Y axis. An applied force in Z direction can be precisely controlled and it is suitable for delicate procedures such as picking up nanowires, pressing nanowires onto the membranes (see APPS, Chapter 3.3.1) or suspended in air microhotplates (see MPW4, Chapter 3.3.1). Two different forms of PDMS stamp were used - one was a flat $11x1x2cm^3$ sized cube and the second one was a specifically manufactured stamp with pillars, which was used for nanowires transfer onto the MPW4 chip. Those transfer processes resulted in the fabrication of multi-nanowire gas sensing devices. The bond tester has been applied to transfer nanowires onto real gas sensor devices: the APPS chip, and the CMOS-integrated µhp array.

Flat PDMS stamp

The transfer of the nanowires was performed with a $1x1x2cm^3$ sized PDMS stamp, which was fabricated as described at the beginning of Chapter 3.2.1, and glued to the tip of a filed screw, which was fixed in the head of the bond tester tool. Next, the stamp was carefully pressed with well controlled parameters (force, distance and position) onto the donor substrate with the synthesized SnO_2 nanowires. The nanowires were picked up with the stamp (see Fig. 3.25) without any liquids - directly from the growth substrate. Afterwards the stamp with the nanowires was moved directly above the electrodes structure of the APPS chip (described in detail in Chapter 3.3.1) and pressed to the surface with a maximum force of 0.7N and 10s contact time, the applied force versus time during the nanowires transfer is shown in Fig. 3.26. The SnO_2 nanowires transferred on the APPS chip is presented in Fig. 3.28a.
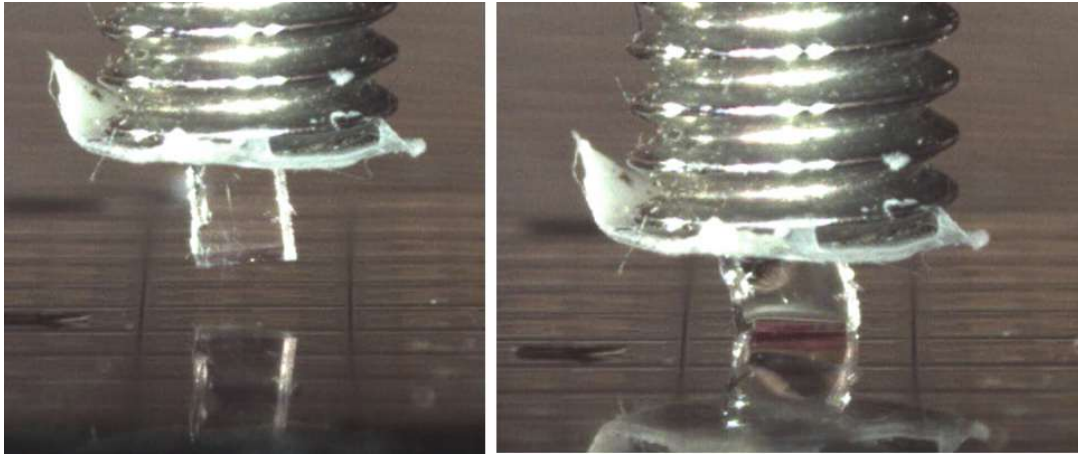
Figure 3.25: Bond tester tool tip with glued PDMS stamp above (left) and pressed (right) to the APPS chip, which was still undiced into the single device.

The integration of metal oxide nanowires was also performed on a real CMOS chip. During the "MSP – Multi Sensor Platform for Smart Building Management" project, a specific chip (MPW4) was designed and fabricated by ams AG. This microchip integrates 8 microhotplates (size $72x72\mu m^2$), which can be operated simultaneously. Each microhotplate implements two separate metal oxide layers, hence the chip has a total of 16 sensor devices (see Fig. 3.37).

A bond tester-based transfer process was performed for the MPW4 chips, which are already glued and wire bonded onto a PCB carrier; the maximum force used in this case was 0.2N in order to avoid breakage of the µhps (see Fig. 3.27). The stamp was big enough to cover two microhotplates simultaneously and the suspended structure of the

µhp was not destroyed. Unfortunately, the coverage of the nanowires on the µhps was very low due to the suspended structure of the µhp and its bending during pressing of the stamp (see Fig. 3.28b). As a result, only very low number of nanowires were transferred to the µhps. Therefore, a more sophisticated approach was applied, which is described in the next chapter.
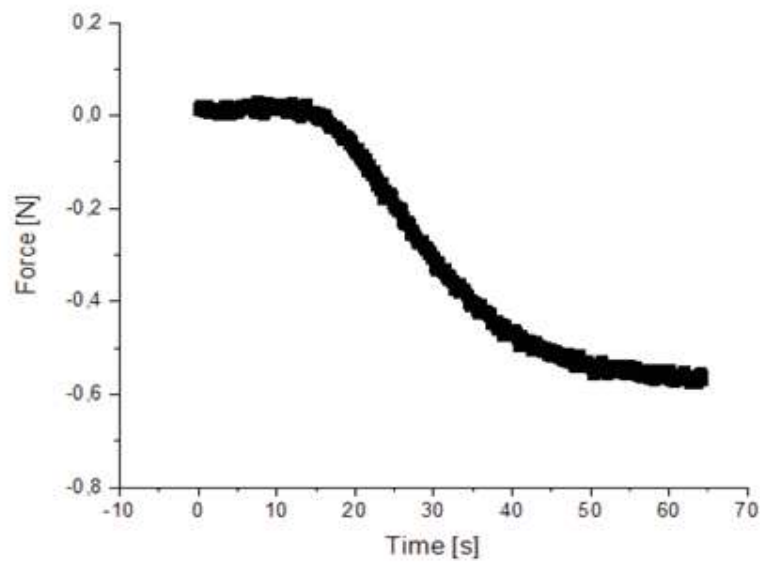
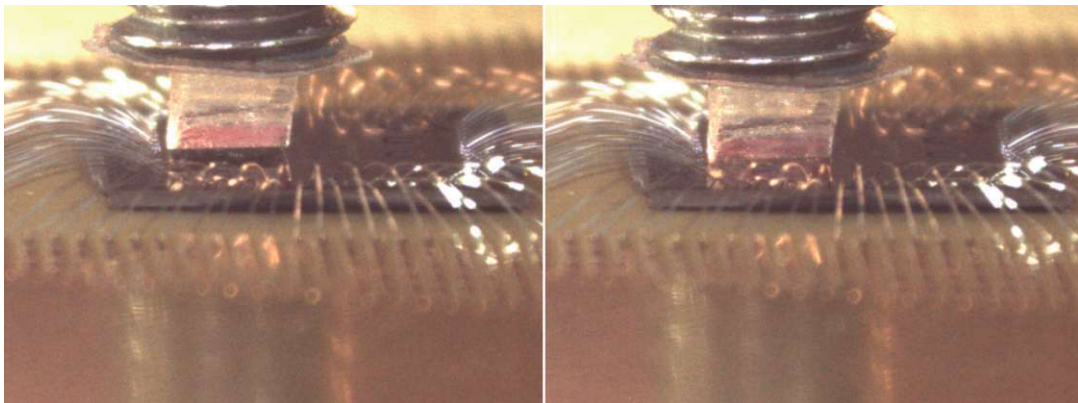Figure 3.26: Force versus time during the nanowires transfer.

Figure 3.27: Bond tester tool tip with glued PDMS stamp above (left) and pressed (right) to the MPW4 chip.
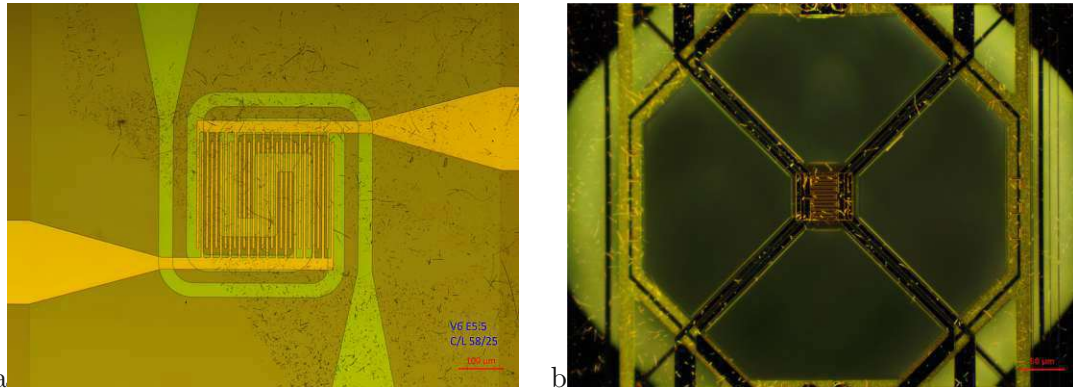
Figure 3.28: a) SnO$_2$ nanowires transferred with a bonder onto the APPS chip and b) MPW4 chip.

Structured PDMS stamp

For transferring nanowires more efficiently on the MPW4 chip, a specific form for a PDMS stamp was designed at MCL in accordance with the dimensions of the MWP4 chip, and produced by a company KBG Kunststoff-Bearbeitungs Ges.m.b.H. (Austria) out of polyoxymethylene (POM). Instead of the flat approach, the stamp exhibits 8 pillars, which can be placed precisely over the 8 µhps (see Fig. 3.29a-d). The middle rectangular structure was prepared to be pressed against the middle of the MPW4 chip, to ensure that the suspended microhotplates will not get too much mechanical pressure themselves, and break.

First tests were performed by manual picking up the SnO$_2$ nanowires from the growth (donor) substrate and pressing the stamp onto a Si/SiO$_2$ chip. In Fig. 3.29 a successful transfer of multiple nanowires is presented, where the structure of the stamp stamp is preserved as reflected in the pattern of the transferred nanowire. The areal density of the nanowires is very high, almost no nanowires were found out of the pillars positions and the middle rectangle.
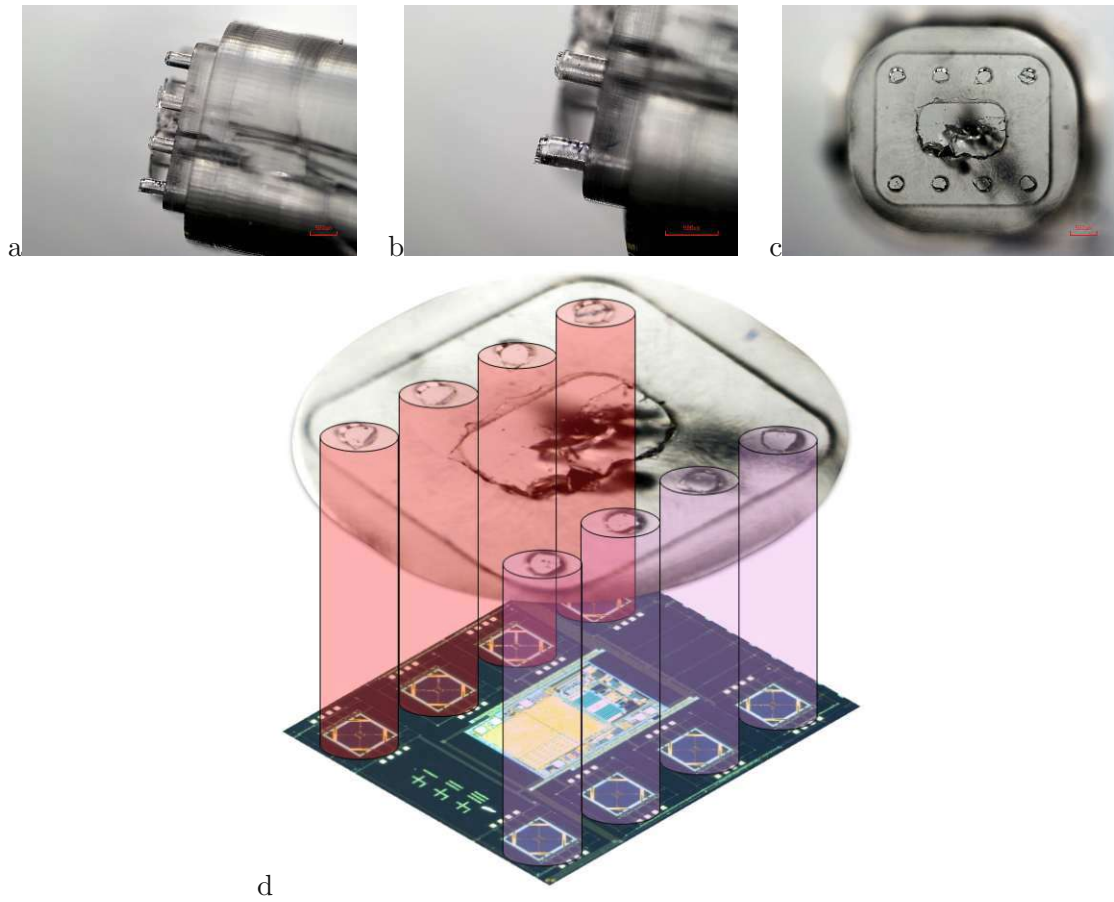
Figure 3.29: Structured PDMS stamp for nanowires transfer, a and b - view form the side, c - view from the top, d - comparison of the stamp with a MPW4 chip.
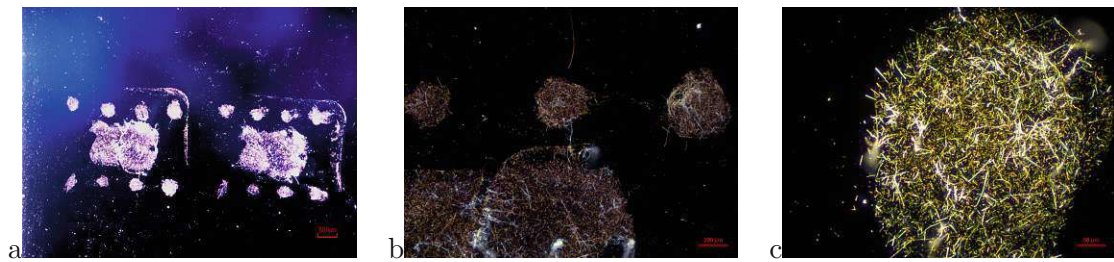
Figure 3.30: Transfer of SnO_2 nanowires with a structured PDMS stamp; a - one stamp was pressed two times near to each other, b - view on the top right corner, and c - view on one of the pillar places.

Next, the stamp was used for the bond tester transfer process. A screw was placed inside the form of the stamp into the liquid PDMS before cross-linking of the polymer and hardening of the stamp to ensure good fastness of the stamp on the movable head of the bond tester. The nanowires were pressed several times to the growth substrate, to ensure high coverage of the nanowires at the ends of the pillars (see Fig. 3.30).
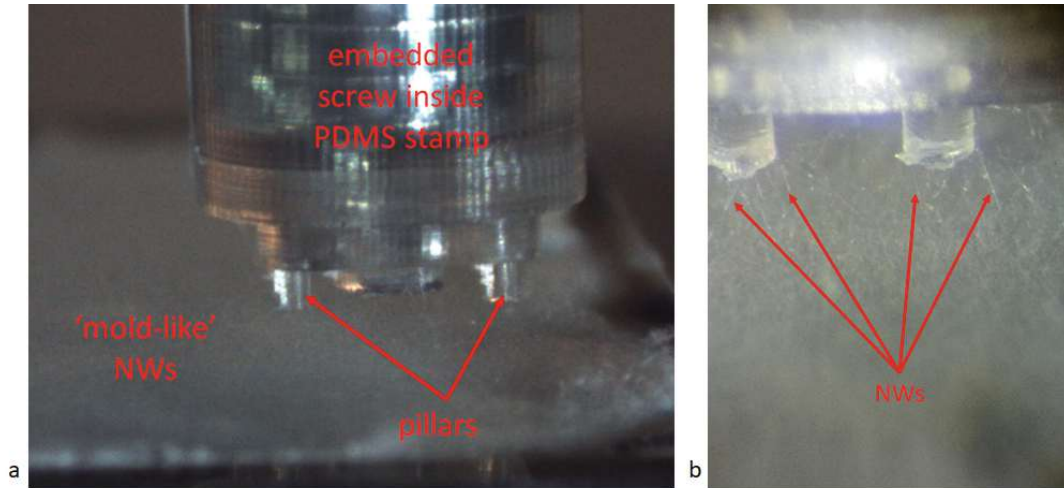
Figure 3.31: Collecting SnO_2 nanowires with a structured PDMS stamp.

After picking up the nanowires the stamp was pressed onto the MPW4 chip, but due to some misalignment in the stamp itself the four outer pillars had to be cut away. The middle 4 pillars were pressed to the MPW4 chip multiple times with 15cN (centinewton, 1cN = 0.01N) force and 10s contact time (see Fig. 3.32). The microhotplates with the SnO_2 nanowires are presented on Fig. 3.33. The resulting sensors could be measured electrically because the nanowires interconnect the fingers of the IDE structure on top of the microhotplate. Not all µhps were covered by the same amount of the nanowires, however, there was enough interconnections to use the devices a gas sensor and measure the sensor response.
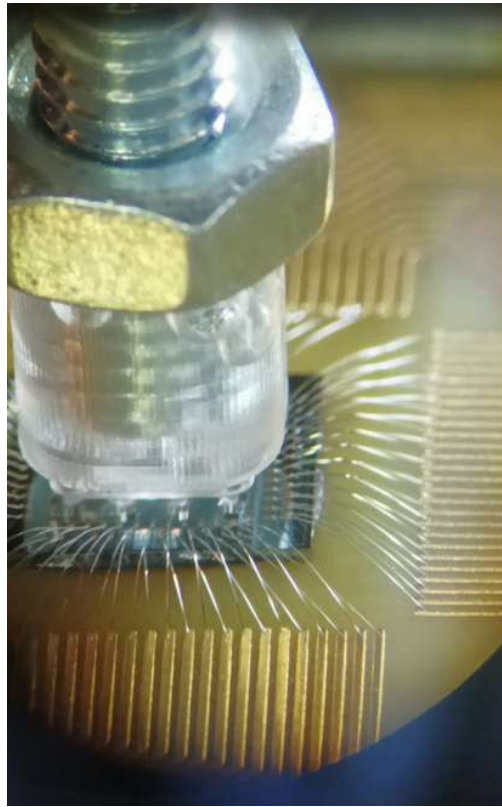
Figure 3.32: Transfer of SnO_2 nanowires with a structured PDMS stamp onto the MPW4.
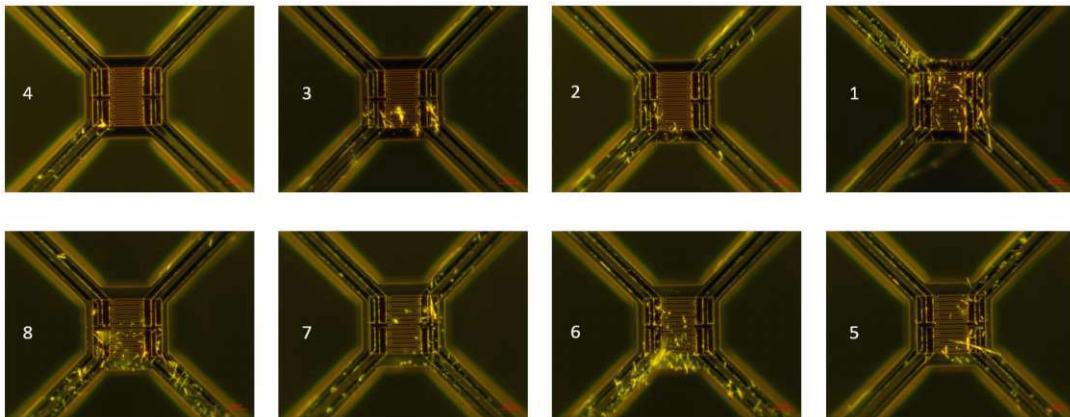
Figure 3.33: Transfer of SnO_2 nanowires with a structured PDMS stamp onto the MPW4 microhotplates (8 of them).

3.3 Characterisation of gas sensing performance

3.3.1 Fabrication of multi-nanowire based gas sensors for gas characterisation

Two main platforms for gas characterisation were used:

- Si-based structures which was mainly applied for testing new materials and/or new methods of transfer due to its simplicity and diversity. For this commercial parts, i.e. heater and thermoresistive elements were implemented to enable the setup of a gas sensor device.

- Microhotplate (μhp) based structures, where two different types were employed. A commercial 2x2mm^2 sized chip from Applied Sensors with a SiN-membrane, integrated heater structure and Pt-electrode. A 4x5mm^2 sized fully CMOS integrated chip integrating a total of 8 micro-hotplates, which has been fabricated by ams AG (nowadays ams OSRAM, Praemstetten, Austria). The main difference between those two structures is the type, size and thickness of the μhp: a 1x1mm^2 sized closed SiN-membrane (thickness 900nm) as compared to the 72x72μm^2 sized, spider-like -suspended CMOS μhp (thickness 8 μm). Both μhp designs are a huge challenge for the nanowire transfer process.

Fabrication of Si-based sensors

Deposition of electrode structure on Si-substrates   Silicon-based structures were produced on a silicon substrate with a 300 nm thick thermal silicon oxide layer on top to provide electrical insulation (Siegert Wafer GmbH, Germany). Firstly, the IDE structure was fabricated by photolithography and evaporation processes. The initial substrate was spin-coated with a positive photoresist (AZ MIR 701, MicroChemicals GmbH, Germany) with 3000 rpm speed for 35 s. A pre-annealing step was applied for 60 s at 100 °C for solvents removal and partial hardening before light exposure. Then a photolithography process (EVG620, EV Group, Austria) was performed. A photomask was designed in-house and produced by Compugraphics Jena GmbH, Germany from Soda Lime glass with a structured chromium layer as a UV-reflective coating. Light exposure was performed in a constant power mode with 70 $\frac{mJ}{cm^2}$, then the sample was developed in AZ726 MIF solution (MicroChemicals GmbH, Germany) for 60 s, followed by rinsing in deionised water (stopper) for 1 min and drying in N$_2$ flow. Next, the structured silicon substrate was coated with an evaporated metallic film, firstly with 5 nm titanium as an adhesion layer and then with 150 nm gold as the electrode material, by Univex exaporator (UNIVEX 450, Leybold AG, Switzerland). After metal deposition the substrates were

put into acetone for 8 h to remove the remaining resist with the metallic layer on top (lift-off process) and leave only the structured IDE. The electrode finger width and the distance between the electrode fingers were both $10\,\mu$m (see Fig. 3.34).
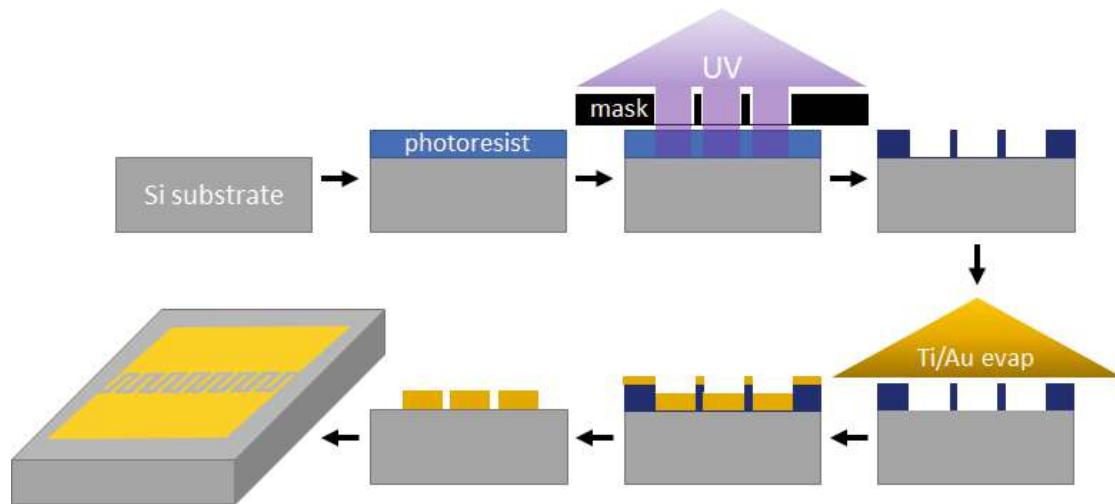

Figure 3.34: Scheme of Ti/Au electrode deposition on a Si-based gas sensing device.

Chip assembly   The silicon substrate with the IDE structure was then assembled by means of another Si sample (5x15 mm^2) as a heatspreader, two microheaters (10 × 2 Pt 6.8, Delta-R GmbH, Germany) and a resistance temperature detector (4 × 1 Pt100, Delta-R GmbH, Germany) for temperature control. As shown in Fig.3.35a, the whole construction was glued with Ceramabond (865 A2, Aremco Products, Inc., distributor: Germany) for homogeneous heat distribution and connected to a ceramic chip carrier. The wires of the microheaters and thermoresistive were soldered to the ceramic chip holder. These are the only "macroscopic" connectors to ensure a good thermal insulation between the sensor setup and the chip holder. The electrodes on Si-substrate were connected to contact pads on the chip holder with Au-wires by a commercial wire bonder (5550 F&K DELVOTEC Bondtechnik GmbH, Austria). The wire bonding procedure, due to thin and delicate Au-wires, was performed after MOx nanowire transfer. Electrical connection legs of the ceramic chip holder provided connection between gas measurement chamber and the electronics for gas sensor performance measurements.
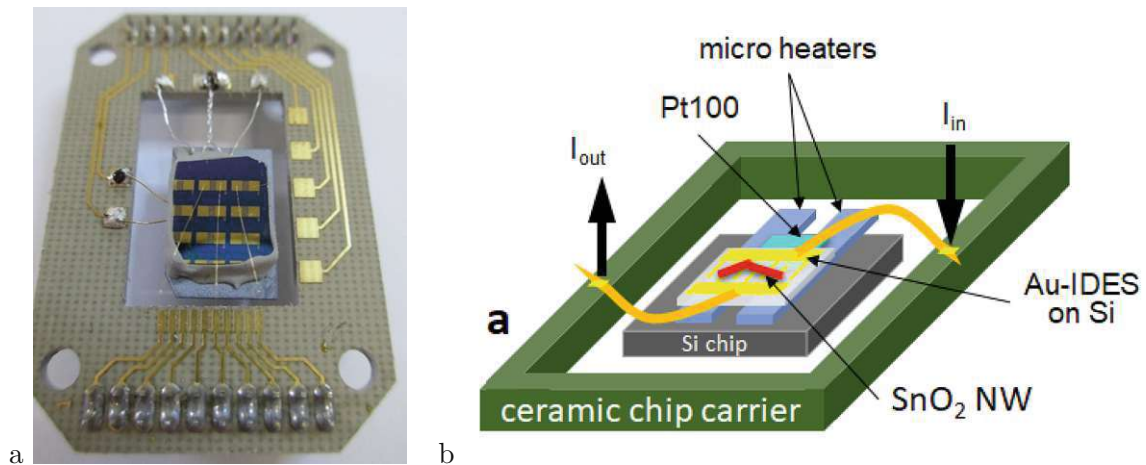
Figure 3.35: a) Picture of an assembled Si-based gas sensing device, b) scheme of an assembled Si-based gas sensing device (from [228]).

Fabrication of APPS-based sensors

The APPS chips did not need any additional processes - they were "ready to use" platforms for nanowire transfer. The APPS chip is a $2x2mm^2$ SiN membrane-based microhotplate device with Pt-IDES exhibiting an electrode width and distance between the electrode fingers of 5 µm, respectively. The whole IDE structure had a width of 250 µm (length of fingers) and length of 300 µm. This is a commercial sensor platform provided by ams AG, Austria, which contains an Pt-based electric microheater on a silicon nitride membrane (1 µm thick), to achieve good thermal isolation and decrease the power consumption of the device. The nanowires were transferred manually and with a bonder (see Chapter 3.2). The APPS chips were then assembled on ceramic packages (Kyocera type KD-SB9F85) with a glue (type LOCTITE ABLESTIK 2035SC) and then wire bonded with a bonder (see Fig. 3.36). Four sensor chips are implemented on each package. A DIL (dual in-line) package is a chip carrier with a rectangular shape and two parallel rows of electrical connecting pins on the back side of the package to provide electrical connections to the sensors. The package itself is mounted on a printed circuit board (PCB), which is implemented in the gas measurement setup.
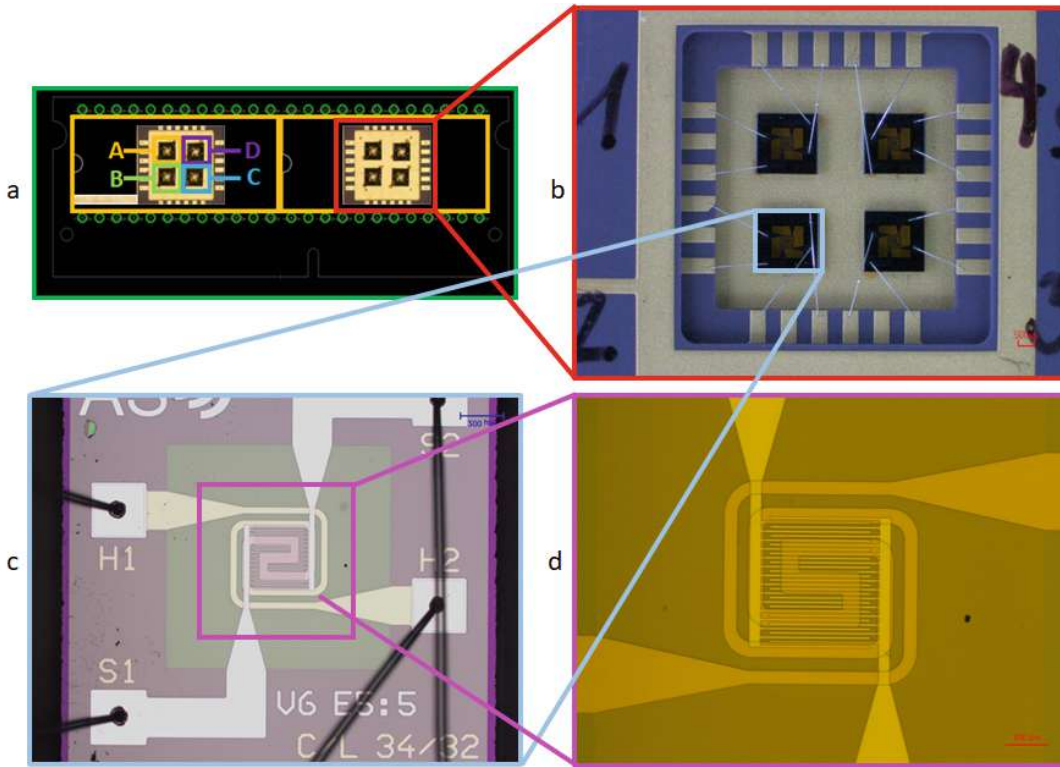
Figure 3.36: a) A scheme of a PCB carrier with two DIL packages, b) picture of the middle of a DIL package with four APPS platforms, c) picture of a bonded APPS platform, d) picture of an IDE structure on APPS chip.

Fabrication of MPW4-based sensors

A MPW4 chip was produced by a CMOS (complementary metal–oxide–semiconductor) technology, which is based on pairs of p-type and n-type metal–oxide–semiconductor field-effect transistors (MOSFETs). The FET is a type of transistor which has three terminals: source, gate and drain and by changing the voltage (field) applied to the gate, the channel between drain and source can change its conductivity. The MOSFET has an insulated gate which modulates the current in the channel by changing field applied to the gate. Due to the insulation of the gate the MOSFET does not require any current from the control system (of any device).
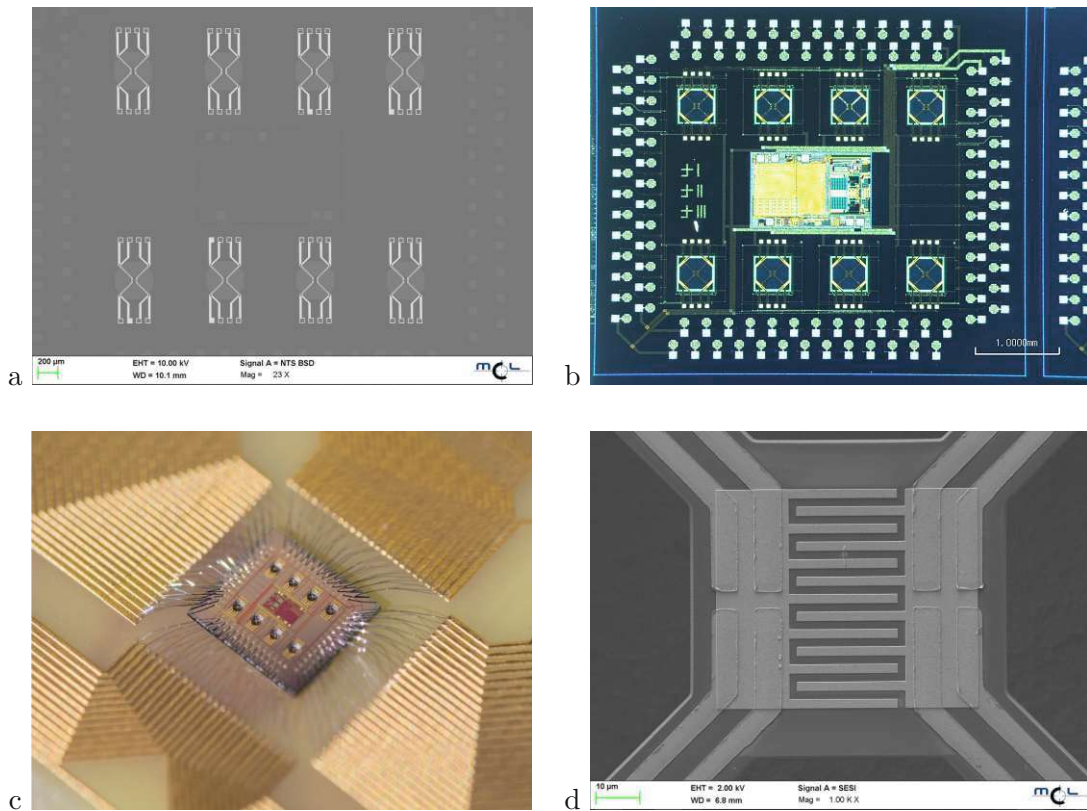
Figure 3.37: MPW4 chips: a) 8 spider-like structures with 8 electrodes for each µhp, b) complete chip with temperature controllers in the middle, c) chip bonded with Au-wires to a specific carrier - for gas measurements, published in [230], and d) gold electrode structure on a single microhotplate, prepared by e-beam lithography.

The MPW4 platform chip has been produced by ams AG with a standard 0.35µm CMOS technology within the FP7 project "MSP - Multi Sensor Platform for Smart Building Management" (Grant No. 611887) and the FFG project "RealNano - Industrielle Realisierung innovativer CMOS basierter Nanosensoren" (Grant No. 843598). The chip contains 8 microhotplates (µhps) with dimensions of $72x72µm^2$ (see Fig. 3.37a and b). The µhp structure is spider-like - a poly-silicon microheater is suspended in air and connected to the rest of the chip by four arms, to ensure thermal insulation between µhp and the rest of the chip, low power consumption - due to low volume of the structure, electrical connection to the heater itself and to the sensing material on top of the µhp. This thermal insulation is achieved by a post-CMOS etching - a XeF_2 isotropic silicon dry etching. Before this etching an additional post-processing is performed to provide electrical connection for the nanowires, which was performed by e-beam lithography. The IDE structure with 2µm thick fingers and 2µm wide gap between them, and 13 fingers in

total, was prepared first by spin-coating the MPW4 chip with a positive resist (AR-P 679.04, ALLRESIST GmbH) with 1000 rpm for 60s. A pre-annealing step was applied for 5 min at 150°C. Then an e-beam lithography process (eLine from Raith GmbH) was performed with exposure of 240 µC/cm², 30kV; the sample was then developed (AR 600-60, ALLRESIST GmbH) for 60s, rinsed in isopropanol, immersed in stopper (AR 600-56, ALLRESIST GmbH) for 30s, rinsed in isopropanol and dried in N_2 flow.

Next, a Ti/Au metal film (thickness 5nm and 200nm) was deposited (Univex Evaporator 450, Leybold AG) followed by a lift-off process, which was performed in acetone for 12h. The final IDE structure on the MPW4 µhp is shown in Fig. 3.37d. The electrodes which are providing electrical connection from the µhp to the contact pads were Ti/Au electrodes deposited by Siemens AG, Munich, Germany. The MPW4 chips were assembled on a special PCB carrier with a glue (ABLEBOND 8290, Ablestik Henkel AG & Co.) and wire-bonded by ams AG in wedge bonding mode of a 25 µm aluminium wire using an automatic wire bonder (Bondjet 810, Hesse GmbH) - Fig. 3.37c. The PCB with the sensor chip can be implemented in the gas measurement setup for sensor performance tests. Finally, the nanowires transfer with the bond tester was performed (see Chapter 3.2.5).

3.3.2 Gas measurement setup - GMS1 and GMS2

The multi-nanowire gas sensor performance was measured in an automated gas measurement setup, which is shown in Fig. 3.38. Synthetic air (ready to use 80% nitrogen and 20% oxygen mixture, Linde Gas GmbH, Austria) was used as a background gas with a constant flow of 1 l/min. The sensor response was tested towards 4 different test gases: carbon monoxide mixture in nitrogen (ready to use mixture of 900 ppm from Linde Gas GmbH, Austria), hydrogen sulfide mixture in nitrogen (ready to use mixture of 10 ppm from Linde Gas GmbH, Austria), hydrocarbon mixture (HCMix, mixture of 500 ppm ethan, 500 ppm ethen, 500 ppm ethyne, and 500 ppm propane in nitrogen, Linde Gas GmbH, Austria), and toluene mixture in nitrogen (ready to use mixture of 50 ppm from Linde Gas GmbH, Austria). The background gas humidity level was adjusted by two mass flow controllers (MFC, F-201CV, Bronkhorst High-Tech B.V., Netherlands). A part of the background gas flows through air bubbler filled with deionized water and is mixed to the dry synthetic air; by controlled mixing the humified and dry air flows, the humidity level can be adjusted Control of relative humidity level was achieved by feedback loop with commercial humidity sensor (AFK-E, KOBOLD Messring GmbH, Germany).

To realize the desired test gas concentration, the ready-to-use test gases have to be further diluted. This was achieved by using three mass flow controllers (high, middle and low flow rates) in parallel, which enables precise adjustment of the test gas concentration. After the MFC's both gases (background and test gases) were mixed together and purged through one of gas chambers - GB1 or GB2. Each of those gas chambers was used for

different type of gas sensor assembly, GB1 was used for the Si-based and GB2 for the APPS and CMOS-based sensors.

The GB1 chamber was a stainless steel cylinder with a volume of $80\,cm^3$, where the chip carrier was placed and connected by shielded cables with measurement units: source measure unit to apply sensor current and measure the signal from the gas sensor (SMU, 2400 SourceMeter, Keithley, United States), SMU to apply current to the heater (PL330P, Thurlby Thandar Instruments, UK) and a multimeter to measure the voltage on the integrated resistance temperature detector, which is then converted to temperature (34401A, from Agilent Technologies, Agilent Technologies). Each of these measurements was conducted with a 1-second interval. All the electronic devices were then connected to the computer and from there operated.

The GB2 chamber was a stainless steel box with a volume of $80\,cm^3$ for the gas flow and the integrated electronic circuits for gas sensor operation and measurement inside the GB2. The GB2 was then connected to the computer and from there operated. A Python program was used for controlling both the gas flow system and the electronic system, for both gas chambers (GB1 and GB2).

3.3.3 Gas measurement methodology and analysis

The multi-nanowire gas sensors were measured with a special routine (one example presented in Fig. 3.39):

- Two hours of annealing at 300°C were performed at the beginning of each gas measurement, for stabilisation of the resistance signal and to ensure homogeneous distribution of the gases inside the gas chamber.

- Three different relative humidity levels (25, 50 and 75%) were selected, to mimic realistic humidity levels in different real-life conditions (home, office, industry etc.)
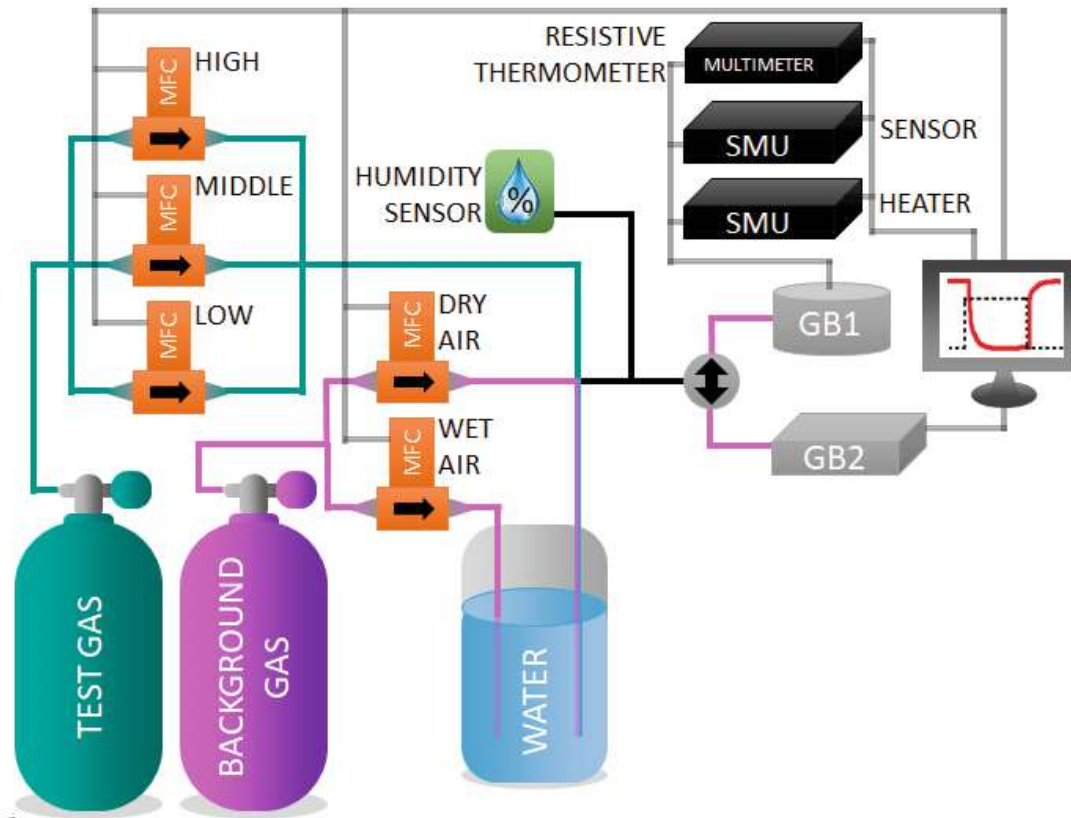
Figure 3.38: Gas measurement setup with two gas chambers - GB1 and GB2.

- Duration of the test gas pulse was 5 minutes, followed by 15 min pure synthetic air. The test gas pulses were always measured with increasing gas concentration (i.e. 10 ppm, 30 ppm, 60 ppm, 100 ppm, 150 ppm and 200 ppm). At least 15 minutes stabilisation time was applied after every relative humidity change or temperature change.

- All measurements were performed in constant current mode, where a specific current was set to the electrodes. The measured voltage was converted into electrical resistance by dividing it by an applied constant current. The voltage change was measured to get the change of the electrical resistance due to the test gas presence in the chamber.

The main performance parameter of the gas sensor is the sensor response (S), which was calculated with Eq. 3.1.

$$S = \frac{|R_{air} - R_{gas}|}{R_{air}} * 100\% \tag{3.1}$$

where R_{air} was a resistance value of the sensor in the background gas (synthetic air) and R_{gas} was a resistance value at the end of the test gas pulse. The sensor response in this work was calculated automatically from raw measurement files with a Python-based program, where R_{air} was calculated as a median from 10 resistance points before the start of a gas pulse and R_{gas} as a median from 10 points just before the end of the gas pulse.

Two other important parameters of gas sensors are the response and recovery times.

- The response time shows how fast a gas sensor can detect the target gas and is defined as a time difference between gas pulse injection and a point when the resistance reaches 90% of the saturation level (in this case - R_{gas}).

- The recovery time shows how fast a gas sensor can reach an initial base resistance and is defined as the time difference between the gas pulse end and the point when the resistance reaches 90% from the initial resistance (in this case - R_{air}). [231] An example of a gas pulse and a resistance measurement is shown in Fig. 3.40.
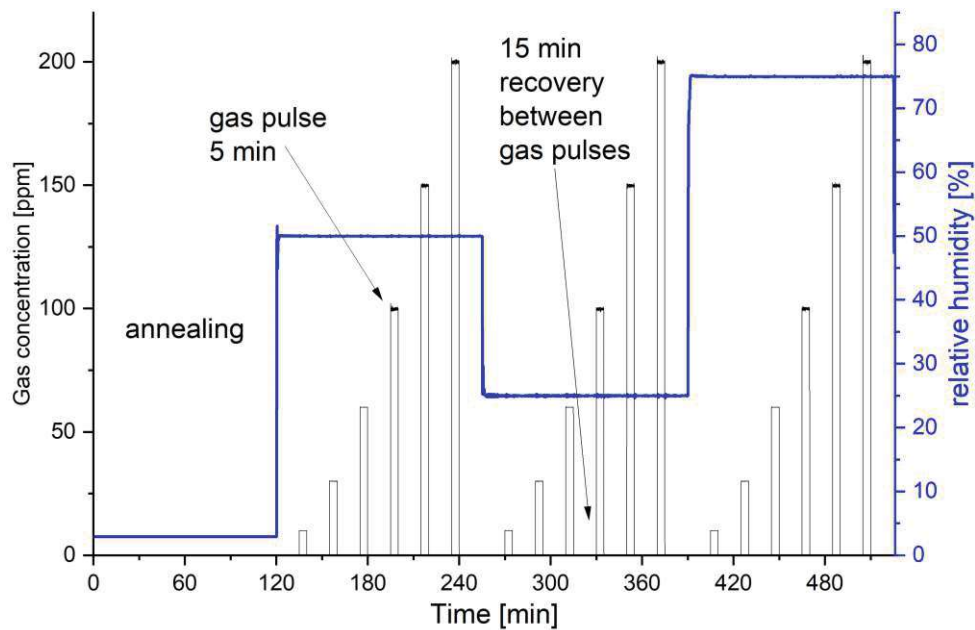
Figure 3.39: Gas measurements routine for 6 different test gas concentrations and 3 different relative humidity levels.
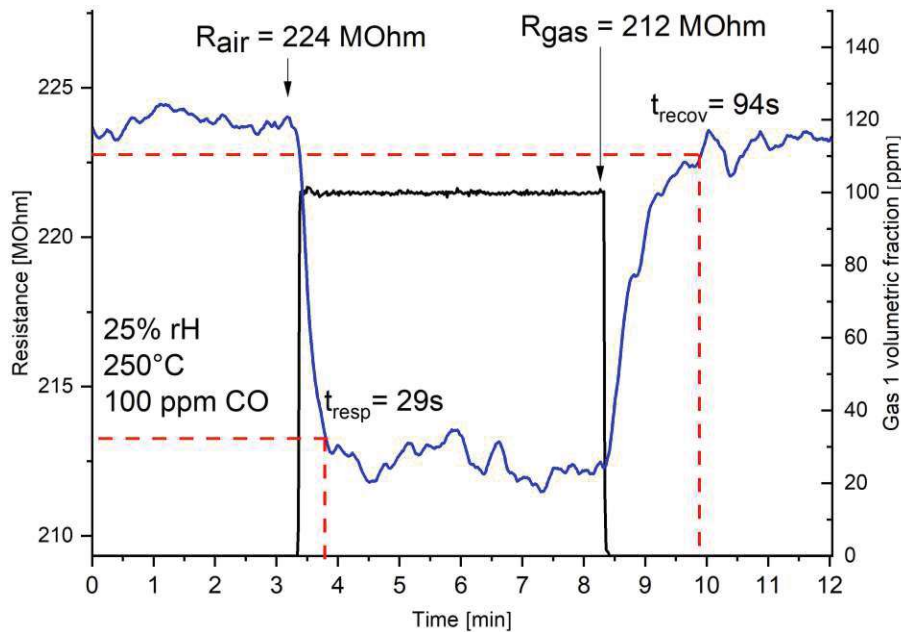
Figure 3.40: Resistance change of a typical WO_3 nanowires-based gas sensor in presence of a gas pulse.

3.3.4 Performance results for SB sensors

CO measurements

The response towards carbon monoxide was measured for two different devices: metal oxide-based nanowires - SnO_2 and WO_3 nanowire-based sensors. The assembly process was described in detail in Section 3.3.1. The transfer of each of the MOx-type was described in Chapter 3.2. The gas measurement methodology was described in Chapter 3.3.3. The protocol of the measurements is as follows:

- CO concentrations: 10 ppm, 30 ppm, 60 ppm, 100 ppm, 150 ppm, 200 ppm

- Relative humidity levels: 25%, 50%, 75%

- Temperature: 300°C (for SnO_2 nanowires) and 250°C (for WO_3 nanowires)

- Constant current mode - 10 nA

Two SB sensors (sensor 1 and sensor 2) were produced on basis of SnO_2 nanowires by manual transfer, and were characterised simultaneously in GMS1 (see Chapter 3.3.2) towards CO at 300°C (Fig. 3.41). The resistance decreases in the presence of the testing gas, which shows that both sensors are sensitive towards CO in a typical manner for a

n-type semiconductor like SnO_2. The base resistance changes with the humidity level. For sensor 1, the base resistance is 46 MΩ at 25% relative humidity, 37 MΩ at 50% relative humidity, and 32 MΩ at 75% relative humidity. For sensor 2, the base resistance is 36 MΩ at 25% relative humidity, 31 MΩ at 50% relative humidity, and 29 MΩ at 75% relative humidity.
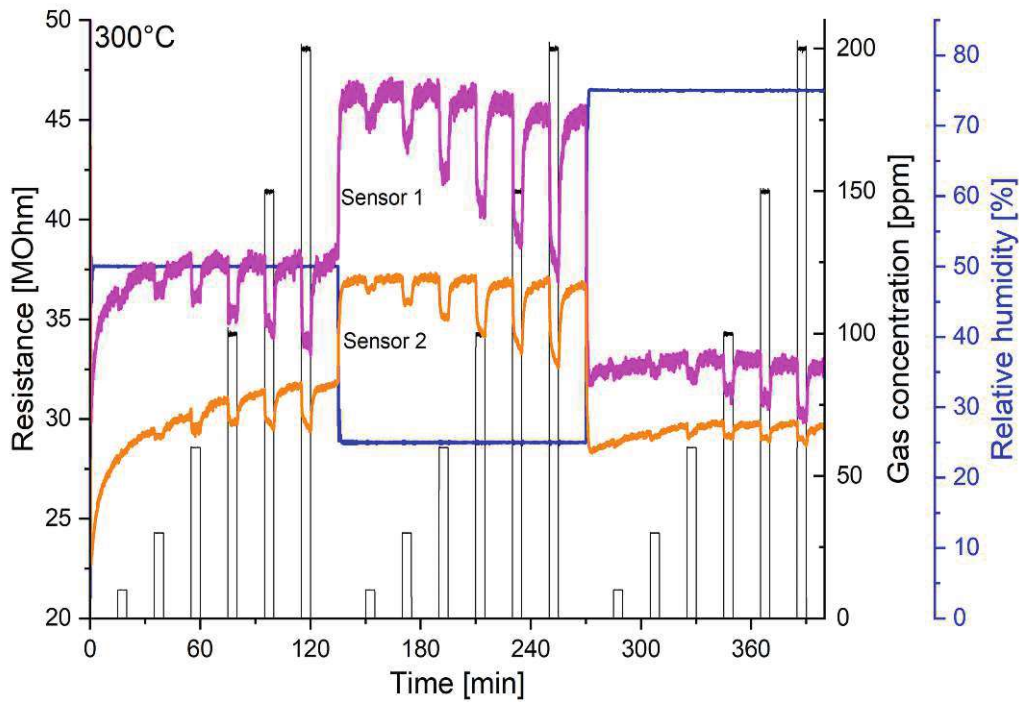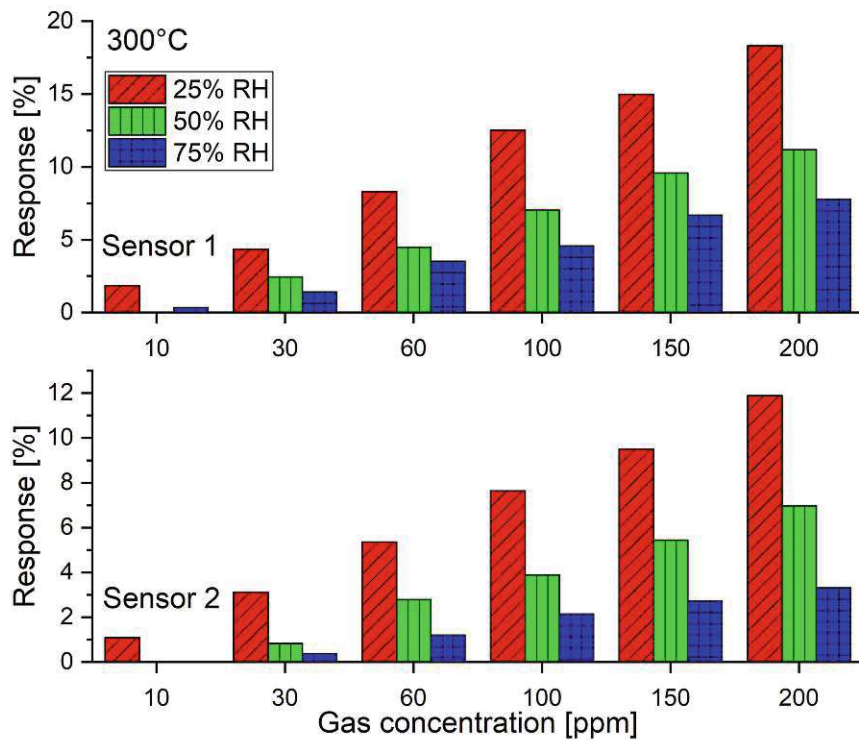

Figure 3.41: Resistance of two SB gas sensors based on SnO_2 nanowires towards CO (10 ppm, 30 ppm, 60 ppm, 100 ppm, 150 ppm and 200 ppm) at 300°C operation temperature and at three different relative humidity levels: 25%, 50% and 75%.

The sensor response is shown in Fig. 3.42: towards 10 ppm CO and at 25% RH sensor 1 and sensor 2 show the highest response of 2%, and 1%. The response increases linearly with increasing concentration up to 18%, and 12% for 200 ppm CO, respectively. This linear behaviour is important for practical applications and might be the consequence of the high surface-to-volume ratio of the SnO_2 nanowires. Both sensors show a similar behaviour concerning relative humidity level - the highest response is achieved at the lowest relative humidity level of 25%, which means that the sensor is cross-sensitive towards water. For example for sensor 1 the response towards 200 ppm of CO decreases from 18% at 25% RH to 8% at 75% RH. The sensor response for sensor 1 is slightly

higher than sensor 2 which might be due to a different number of nanowires which were transferred on the two sensors. Also the diameters of the nanowires used as sensor components are certainly different for both sensors, However, the comparable results obtained from both sensors indicates a good reproducibility of the multi-nanowire approach. Hence, we conclude that the PDMS stamp-based transfer method could be used for reproducible sensor fabrication.

The sensors were characterized at different operation temperatures (250°C, 300°C, and 350°C) and have obtained the highest response for SnO_2 and WO_3-based sensors for operation temperatures of 300°C and 250°C, respectively.
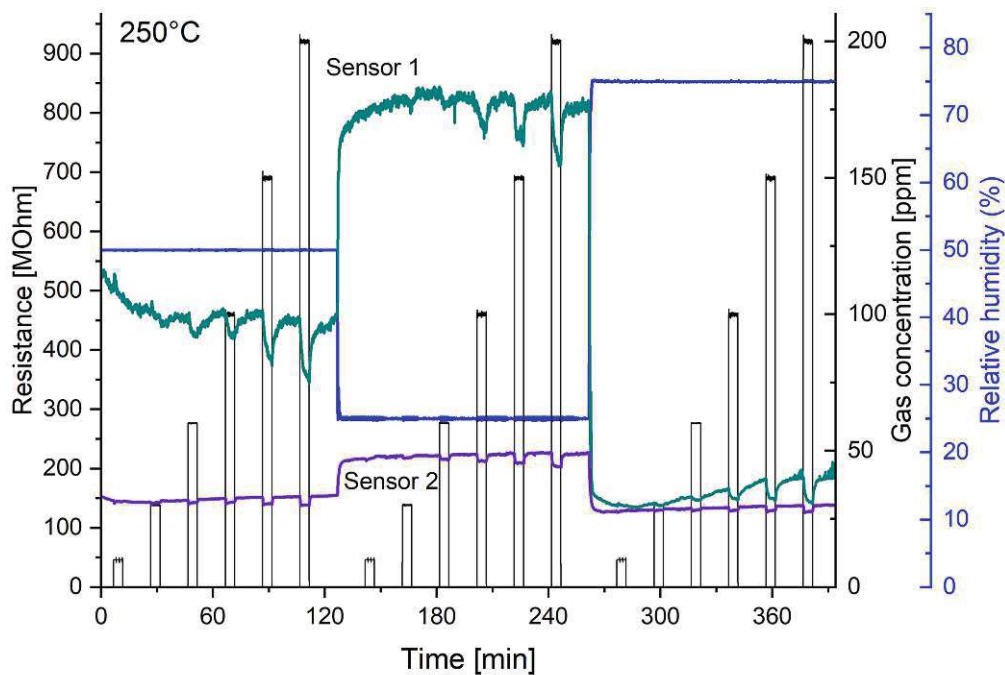

Figure 3.42: Response of two SB gas sensors based on SnO_2 nanowires towards CO (10 ppm, 30 ppm, 60 ppm, 100 ppm, 150 ppm and 200 ppm) at 300°C operation temperature and at three different relative humidity levels: 25%, 50% and 75% (presented also in [228]).

The same methodology was used for WO_3 nanowires - two SB sensors (sensor 1 and sensor 2) were produced by manual transfer and measured simultaneously in GMS1 towards CO at 250°C (Fig. 3.43). The resistance decreases in the presence of the testing gas, which shows that both sensors are sensitive towards CO in a typical manner for a n-type

semiconductor. The base resistance changes with the humidity level. For sensor 1, the base resistance is 820 MΩ at 25% relative humidity, 460 MΩ at 50% relative humidity, and 175 MΩ at 75% relative humidity. For sensor 2, the base resistance is 220 MΩ at 25% relative humidity, 150 MΩ at 50% relative humidity, and 130 MΩ at 75% relative humidity. The base resistance of sensor 1 is significantly higher than for sensor 2, which might be due to the different amount of WO_3 bundles, which have been transferred onto the IDE structures of both sensors.

The sensor response is shown in Fig. 3.44: towards 10 ppm CO and at 25% RH sensor 1 and sensor 2 show the highest response of 2%, and 1%. The response increases linearly with increasing concentration up to 14%, and 11% for 200 ppm CO, respectively. Both sensors show a cross-sensitivity towards water, but for the sensor 1 the highest response is achieved for the highest relative humidity level, and for sensor 2 it is the opposite (similar to SnO_2 nanowires). This may be attributed to variations in the mechanisms of water interaction with different nanowire bundle dimensions and the number of bundles on the IDE structures of each sensor. The sensor responses for both sensors are similar, which means that also the Blue Low Tack Tape-based transfer method could be used for reproducible sensor fabrication.

Figure 3.43: Resistance of two SB gas sensors based on WO_3 nanowires towards CO (10 ppm, 30 ppm, 60 ppm, 100 ppm, 150 ppm and 200 ppm) at 250°C operation temperature and at three different relative humidity levels: 25%, 50% and 75%.
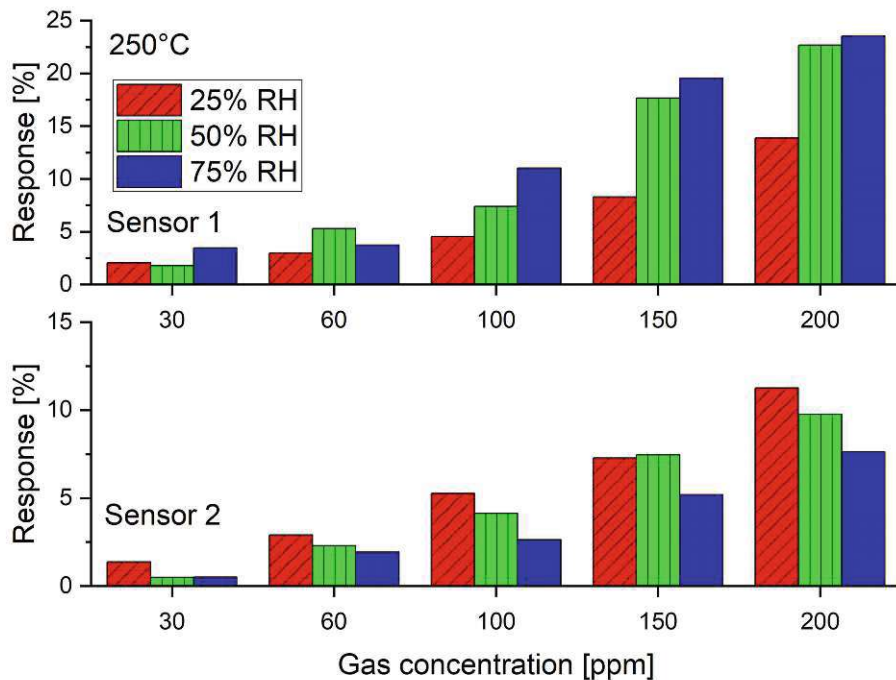
87

Figure 3.44: Response of two SB gas sensors based on WO_3 nanowires towards CO (30 ppm, 60 ppm, 100 ppm, 150 ppm and 200 ppm) at 250°C operation temperature and at three different relative humidity levels: 25%, 50% and 75%.

H_2S **measurements**

The sensors were also tested towards hydrogen sulfide for two different metal oxide-based nanowires - SnO_2 nanowires and WO_3 nanowires. Gas measurement methodology was described in Chapter 3.3.3. The protocol of the measurement is as follows:

- H_2S concentrations: 10 ppb, 100 ppb, 1 ppm (for SnO_2 nanowires) and 200 ppb, 500 ppb, 1 ppm (for WO_3 nanowires)

- Relative humidity levels: 25%, 50%, 75%

- Temperature: 350°C (for SnO_2 nanowires) and 400°C (for WO_3 nanowires)

- Constant current mode - 10 nA

Three SB sensors (sensor 1 and sensor 2 were measured also for CO) were produced on basis of SnO_2 nanowires by manual transfer, and were characterised simultaneously in GMS1 (see Chapter 3.3.2) towards H_2S at 350°C (Fig. 3.45). The resistance decreases in the presence of the testing gas, which shows that all three sensors are sensitive towards

H$_2$S in a typical manner for a n-type semiconductor. The base resistance changes with the humidity level. For sensor 1, the base resistance is 27 MΩ at 25% relative humidity, 24 MΩ at 50% relative humidity, and 21 MΩ at 75% relative humidity. For sensor 2, the base resistance is 21 MΩ at 25% relative humidity, 17 MΩ at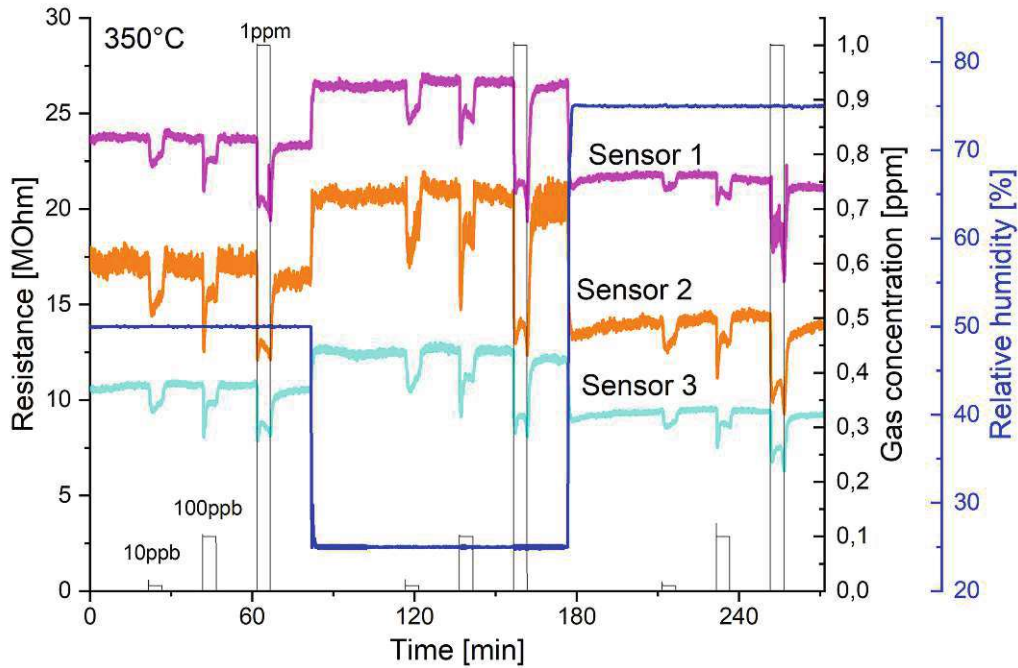 50% relative humidity, and 14 MΩ at 75% relative humidity. For sensor 3, the base resistance is 13 MΩ at 25% relative humidity, 11 MΩ at 50% relative humidity, and 9 MΩ at 75% relative humidity.

Figure 3.45: Resistance of three SB gas sensors based on SnO$_2$ nanowires towards H$_2$S (10 ppb, 100 ppb and 1 ppm) at 350°C operation temperature and at three different relative humidity levels: 25%, 50% and 75%.

The sensor response is shown in Fig. 3.46: towards 10 ppb H$_2$S and at 25% RH sensor 1, sensor 2, and sensor 3 show the highest response of 9%, 7%, and 5%. The response increases with increasing concentration up to 32%, 37%, and 24% for 1 ppm H$_2$S, respectively. All three sensors show a similar behaviour concerning relative humidity level - the highest response is achieved by the lowest relative humidity level of 25%, which means that the sensor is cross-sensitive towards water, i.e. for sensor 1 the response towards 1 ppm ofH$_2$S decreases from 32% at 25% RH to 29% at 75% RH. Sensor 1 and sensor 2 response of 6-8% was achieved for H$_2$S concentration as low as 10 ppb - which demonstrates a very high response towards very small concentrations of this highly toxic gas.
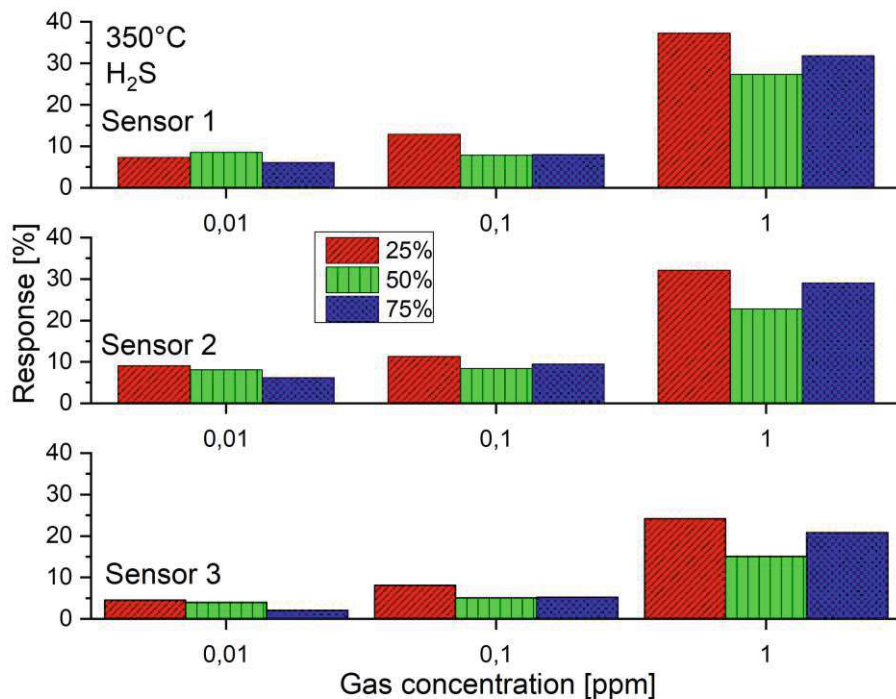
89

Figure 3.46: Response of three SB gas sensors based on SnO_2 nanowires towards H_2S (10 ppb, 100 ppb and 1 ppm) at 350°C operation temperature and at three different relative humidity levels: 25%, 50% and 75% (presented also in [228]).

The resistance curves of the SnO_2-nanowire based sensors towards H_2S show very specific features: for 10 ppb the shape of the curve is rather normal, for 100 ppb there is a significant "overshoot" in the resistance decrease followed by a second decrease; for 1 ppm the curve exhibits two significant minima in the resistance. Obviously these features reflect to some extent the level of concentration. Detailed investigation of these response features and exploitation for practical applications will be the topic of future work.

The sensors were characterized at various operating temperatures (250°C, 300°C, 350°C, and 400°C). The SnO_2-based sensor showed the highest response and most stable base resistance curve at 350°C, while the WO_3-based sensor achieved these at 400°C.

For WO_3 nanowires (manual transfer, same as sensor 1 for CO measurement) one SB sensor was measured in GMS1 towards H_2S at 400°C (Fig. 3.47). The resistance decreases in presence of the testing gas, which shows that the sensor is sensitive towards H_2S in a typical manner for a n-type semiconductor. The base resistance changes with the humidity level. At 25% RH, the base resistance is 82 MΩ, at 50% RH - 92 MΩ, and 50 MΩ at 75% relative humidity. The lower base resistance at 25% RH compared to that at 50% RH is likely because a stable resistance value wasn't reached; the resistance continued to decrease even after the last pulse at 50% RH.
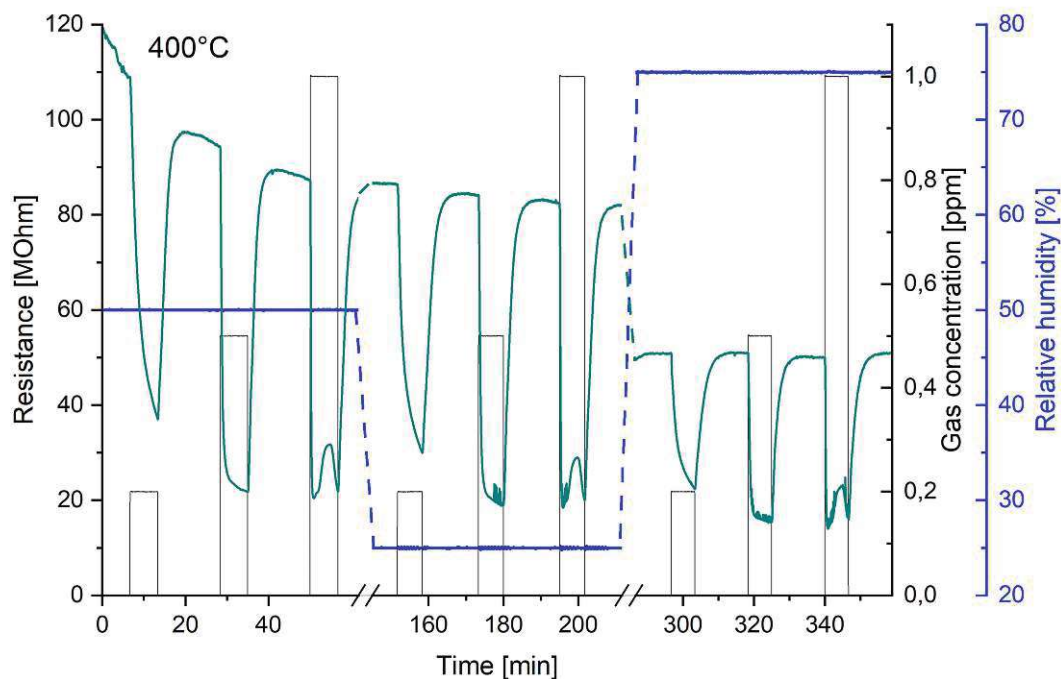
Figure 3.47: Resistance of SB gas sensor based on WO$_3$ nanowires towards H$_2$S (200 ppb, 500 ppb and 1 ppm) at 400°C operation temperature and at three different relative humidity levels: 25%, 50% and 75%.

The sensor response is shown in Fig. 3.48. Towards 200 ppb H$_2$S and for 25% RH the sensor show a very high response of 65%. The response increases up to 77% for 500 ppb, and decrease to 75% for 1 ppm H$_2$S. This behaviour indicates a kind of saturation. At high gas concentrations, the sensor's surface becomes saturated with adsorbed gas molecules. Once all active sites are occupied, additional gas molecules cannot adsorb, causing the sensor's response to plateau. The other explanation can be limited charge transfer - at high gas concentrations the charge transfer may reach its limit, after which additional gas molecules no longer significantly affect the sensor's resistance, resulting in saturation of the sensor response.

The sensor response shows the cross-sensitivity towards water and that the response of WO$_3$-based sensor for 1 ppm H$_2$S at 25% RH is double the response of the SnO$_2$-based sensor in the same conditions. Main conclusion is that the WO$_3$-based sensor is highly sensitive towards H$_2$S and the Blue Low Tack Tape-based transfer method leads to an organic residue-free gas sensing device.

Similar as for the SnO$_2$-nanowire-based sensor, the response curves of the WO$_3$-nanowire-based sensor towards H$_2$S show some specific features: For 200 ppb and 500 ppb the

shape of the curve is rather normal, while for 1 ppm there are again two significant minima in the resistance behaviour.
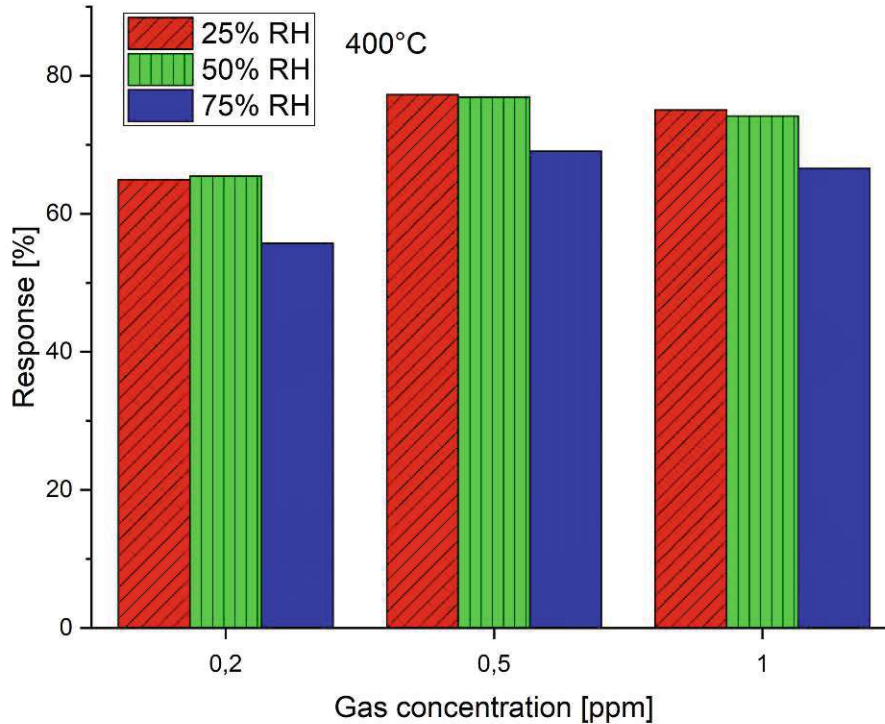

Figure 3.48: Resistance of SB gas sensor based on WO_3 nanowires towards H_2S (200 ppb, 500 ppb and 1 ppm) at 400°C operation temperature and at three different relative humidity levels: 25%, 50% and 75%.

3.3.5 Performance results for APPS sensors

CO measurements

The response towards carbon monoxide was measured for SnO_2 nanowires. The assembly process was described in Chapter 3.3.1) and the transfer of each of the MOx-type in Chapter 3.2. Gas measurement methodology was described in Chapter 3.3.3. The protocol of the measurement is as follows:

- CO concentrations: 10 ppm, 30 ppm, 60 ppm, 100 ppm, 150 ppm, 200 ppm

- Relative humidity levels: 25%, 50%, 75%

- Temperature: 350°C

- Constant current mode - 10 nA

Two APPS sensors (sensor 1A and sensor 1B) were produced on basis of SnO_2 nanowires by manual transfer, were measured simultaneously in GMS2 (check 3.3.2) towards CO at 350°C (Fig. 3.49). The resistance decreases in the presence of the testing gas, which shows that both sensors are sensitive towards CO in a typical manner for an n-type semiconductor like SnO_2. The base resistance changes with the humidity level. For sensor 1A, the base resistance is 18 MΩ at 25% relative humidity, 20 MΩ at 50% relative humidity, and 17 MΩ at 75% relative humidity. For sensor 1B, the base resistance is 32 MΩ at 25% relative humidity, 35 MΩ at 50% relative humidity, and 32 MΩ at 75% relative humidity. The difference between base resistances for all humidity levels is not as high as for the SB sensors. For SnO_2 nanowires-based SB sensors and CO measurements the difference between the highest and the lowest base resistance was 20-30%, and for APPS-based devices it is 9-15%. It shows that the IDE material (Au for SB sensors, and Pt for APPS sensors) and the substrate material (SiO_2-thick wafer for SB device, and SiN-thin membrane for APPS device) have a crucial role in the sensor characteristics.
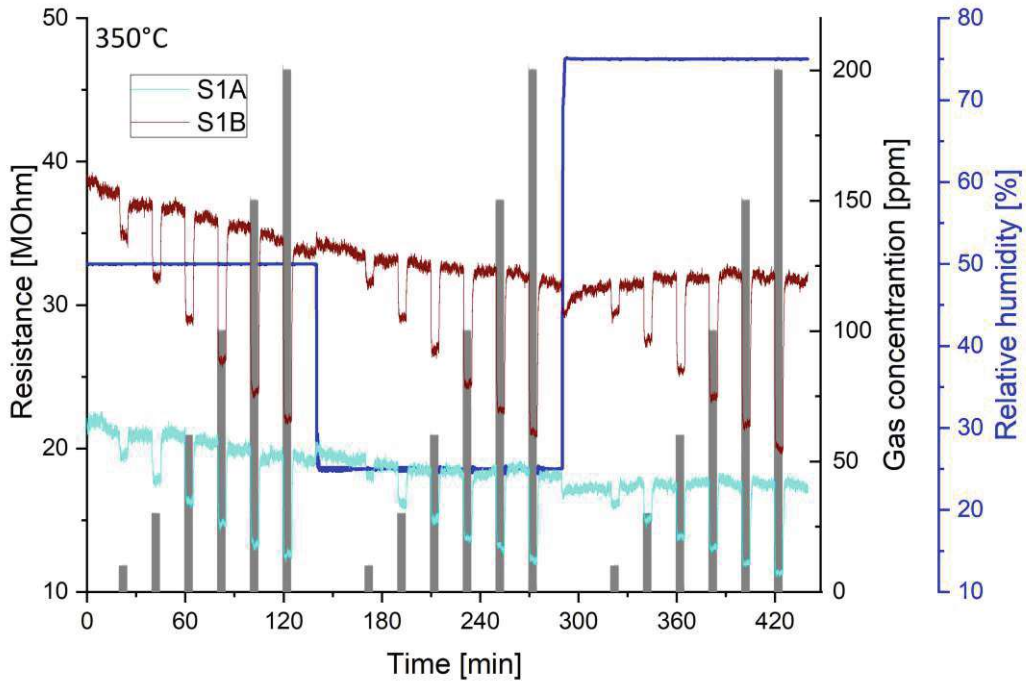
Figure 3.49: Resistance of two APPS gas sensors based on SnO_2 nanowires towards CO (10 ppm, 30 ppm, 60 ppm, 100 ppm, 150 ppm and 200 ppm) at 350°C operation temperature and at three different relative humidity levels: 25%, 50% and 75%.

The sensor response is shown in Fig. 3.50: towards 10 ppm CO and at 25% RH sensor 1A and sensor 1B show the highest response of 7% and 5%, respectively. The response increases linearly with increasing concentration up to 34% for both sensors for 200 ppm

CO. At the highest CO concentration, the response varies by only 3% for sensor 1A and 8% for sensor 1B across different humidity levels. This indicates a small cross-sensitivity towards water, which can be beneficial for future applications. The sensor response for APPS-based gas sensors is also higher than the one for SB-based gas sensors (APPS - 34% for 200 ppm CO, SB - 18% and 12%), which indicates a higher surface-to-volume ratio for APPS sensors.
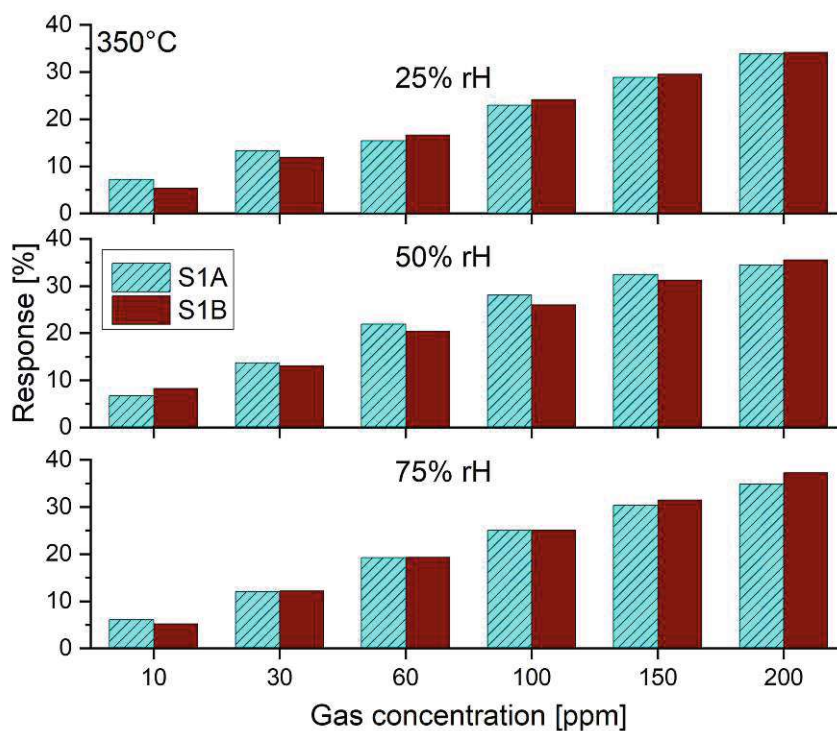

Figure 3.50: Response of two APPS gas sensors based on SnO_2 nanowires towards CO (10 ppm, 30 ppm, 60 ppm, 100 ppm, 150 ppm and 200 ppm) at 350°C operation temperature and at three different relative humidity levels: 25%, 50% and 75%.

The sensor response for both sensors are very similar, which means that the PDMS-based transfer method could be used for reproducible sensor fabrication. The commercial platform allows for very precise and repeatable measurements. The repeatability of the measurements was also demonstrated 2 years after the first measurement for sensor 1A, and then compared with the previous results (see Fig. 3.51 and Fig. 3.52). The sensor was stored in ambient air and exhibits a very similar response characteristic both in 2018 as well as and in 2020. Obviously the sensing activity is not significantly changed in time, which might be due to the fact that single crystalline nanowires have a higher stability as compared to their polycrystalline counterparts. The cross-sensitivity towards water is higher after 2 years storage. The increase in cross-sensitivity to water in a metal oxide gas sensor after a long time storage is probably due to a combination of surface

degradation, structural changes in the metal oxide, electrical property alterations (i.e. microheater ageing), and overall sensor ageing.
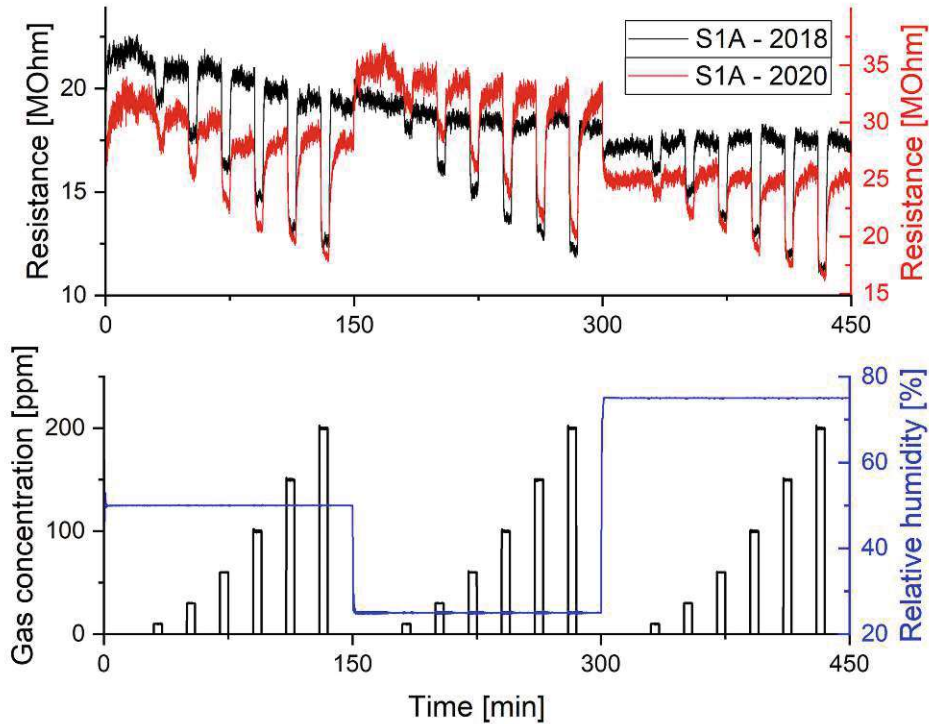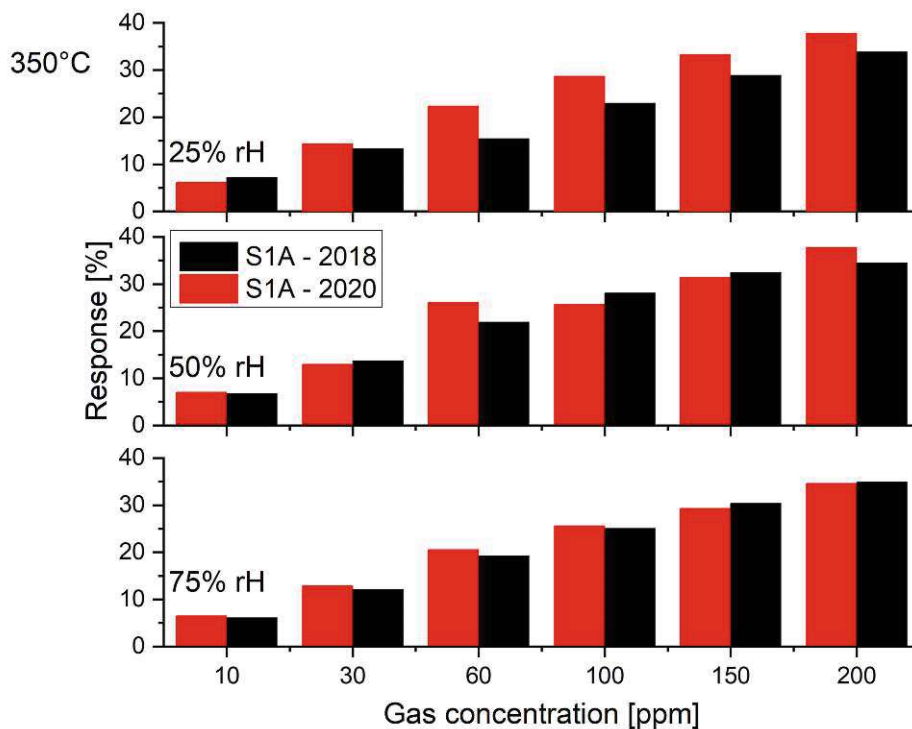

Figure 3.51: Resistance of APPS gas sensor based on SnO_2 nanowires towards CO (10 ppm, 30 ppm, 60 ppm, 100 ppm, 150 ppm and 200 ppm) at 350°C operation temperature and at three different relative humidity levels: 25%, 50% and 75%. The black curve was measured in 2018, the red curve 2 years later in 2020.

Two APPS sensors (sensor 2A and sensor 2C) were produced on basis of SnO_2 nanowires (transferred with a bonder) and were measured simultaneously in GMS2 (Chapter 3.3.2) towards CO at 350°C (Fig. 3.53). One APPS sensor with SnO_2 nanowires transferred manually (1A) was measured with sensors 2A and 2C (the same measurement as in Fig. 3.51). The resistance decreases in the presence of the testing gas, which shows that both sensors (2A and 2C) are sensitive towards CO in a typical manner for an n-type semiconductor like SnO_2. The base resistance changes with the humidity level. For sensor 2A, the base resistance is 85 MΩ at 25% relative humidity, 84 MΩ at 50% relative humidity, and 92 MΩ at 75% relative humidity.

Figure 3.52: Response of APPS gas sensor based on SnO$_2$ nanowires towards CO (10 ppm, 30 ppm, 60 ppm, 100 ppm, 150 ppm and 200 ppm) at 350°C operation temperature and at three different relative humidity levels: 25%, 50% and 75% with time difference of 2 years.

For sensor 2C, the base resistance is 66 MΩ at 25% relative humidity, 66 MΩ at 50% relative humidity, and 70 MΩ at 75% relative humidity. The difference between base resistances for all humidity levels is similar for the manually transferred and for the bonder-transferred nanowires: 9-15% for manual transfer and 6-9% for transfer with a bonder. The higher base resistance observed in the bonder-transferred-nanowires devices (2A and 2C) compared to the manually-transferred-nanowires device is likely due to the lower number of nanowires transferred onto the IDE structure of the APPS chips using the bonder.

The sensor response is shown in Fig. 3.54: towards 10 ppm CO and at 25% RH sensor 2A and sensor 2C show the highest response of 2%, and 3%. The response increases linearly with increasing concentration up to 16%, and 24% for 200 ppm CO, respectively. The response towards CO is similar for all humidity levels, for example for sensor 2C the response towards 200ppm CO at 25%, 50%, and 75% RH is 24%, 23%, and 25%, respectively. This implies a low cross-sensitivity towards water, which was already observed for manually-transferred-nanowire devices. The sensor response for both sensors are similar, which means that the PDMS-based transfer method with a bonder could be

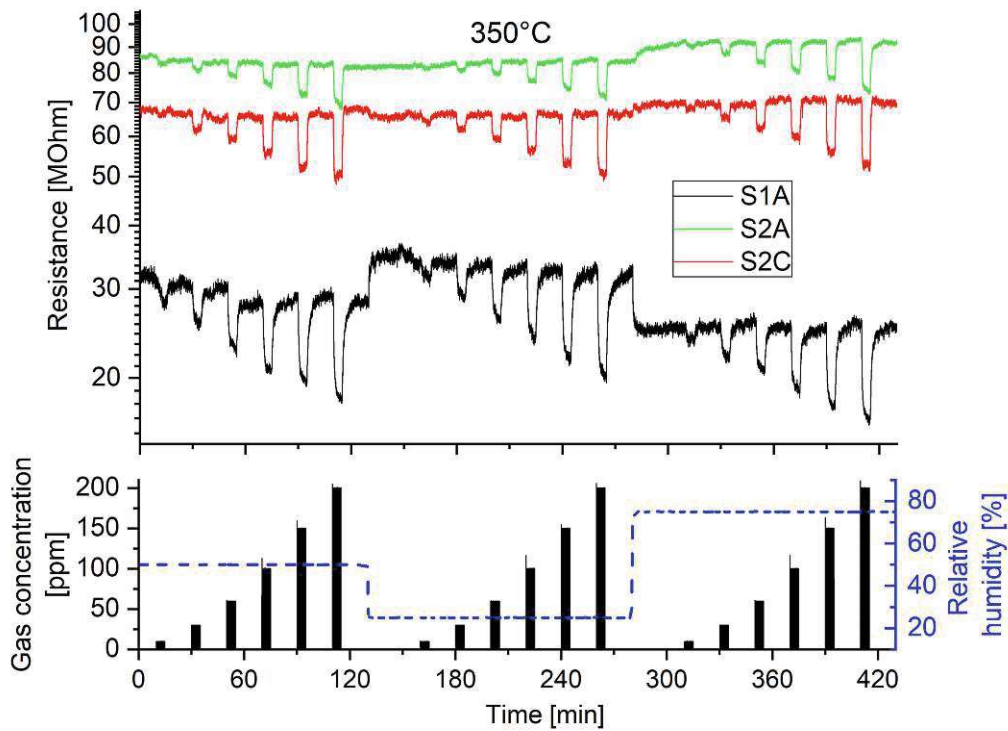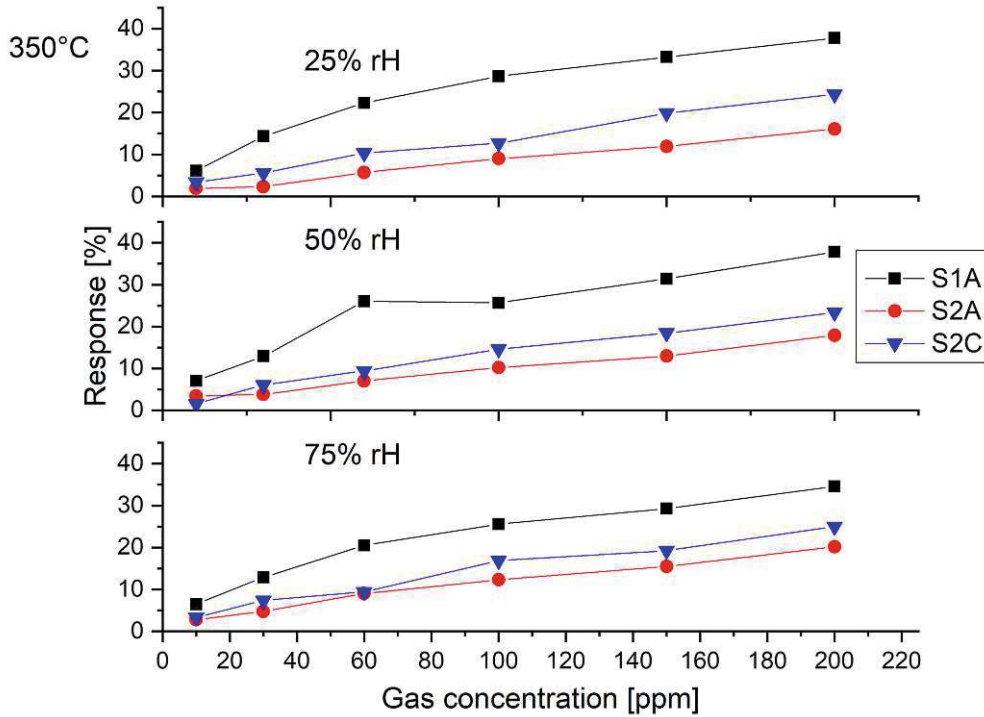used for reproducible sensor fabrication.

Figure 3.53: Resistance of APPS gas sensors based on SnO$_2$ nanowires transferred manually (S1A) and transferred with a bonder (S2A and S2C) towards CO (10 ppm, 30 ppm, 60 ppm, 100 ppm, 150 ppm and 200 ppm) at 350°C operation temperature and at three different relative humidity levels: 25%, 50% and 75%.

HCMix measurements

The response towards HCMix was measured for SnO$_2$-based, manually transferred nanowires sensors - the same sensors which were characterized for CO-response. The protocol of the measurement is as follows:

- HCMix concentrations: 0.5 ppm, 1 ppm, 5 ppm, 10 ppm, 50 ppm and 100 ppm

- Relative humidity levels: 25%, 50%, 75%

- Temperature: 350°C

- Constant current mode - 10 nA

Two APPS sensors (sensor 1A and sensor 1B) were produced on basis of SnO_2 nanowires by manual transfer, and were measured simultaneously in GMS2 (check 3.3.2) towards HCMix at 350°C operation temperature (Fig. 3.55).

Figure 3.54: Response of APPS gas sensor based on SnO_2 nanowires transferred manually (S1A) and transferred with a bonder (S2A and S2C) towards CO (10 ppm, 30 ppm, 60 ppm, 100 ppm, 150 ppm and 200 ppm) at 350°C operation temperature and at three different relative humidity levels: 25%, 50% and 75%.

The resistance decreases in the presence of the testing gas, which shows that both sensors are sensitive towards HCMix in a typical manner for an n-type semiconductor like SnO_2. The base resistance changes with the humidity level. For sensor 1A, the base resistance is 21 MΩ at 25% relative humidity, 21 MΩ at 50% relative humidity, and 19 MΩ at 75% relative humidity. For sensor 1B, the base resistance is 30 MΩ at 25% relative humidity, 31 MΩ at 50% relative humidity, and 29 MΩ at 75% relative humidity. The base resistance of both sensor is similar to the base resistance measured during CO measurement (Fig. 3.49), which indicates high stability of the multi-nanowire devices.

The sensor response is shown in Fig. 3.56: towards 0.5 ppm HCMix and at 25% RH, sensor 1A and sensor 1B show the highest response of 2%, and 1%. The response increases with increasing concentration up to 28%, and 44% for 100 ppm HCMix, respectively. The response towards HCMix is similar for all humidity levels, for example for sensor 1A

the response towards 100 ppm HCMix at 25%, 50%, and 75% RH is 28%, 27%, and 26%, respectively. This implies a low cross-sensitivity of SnO_2 nanowires towards water.
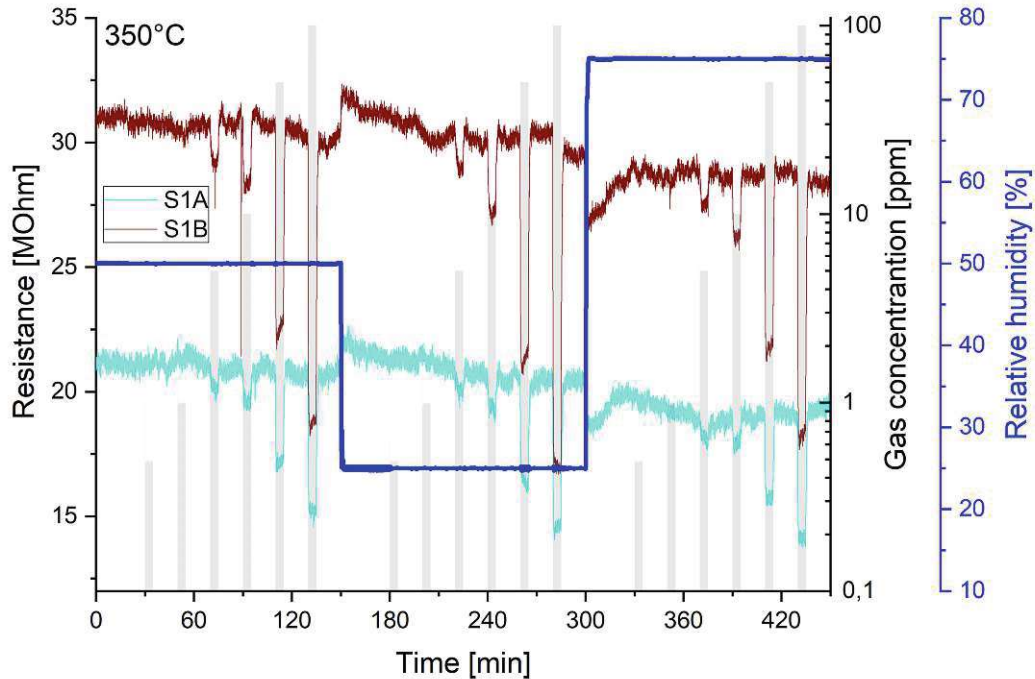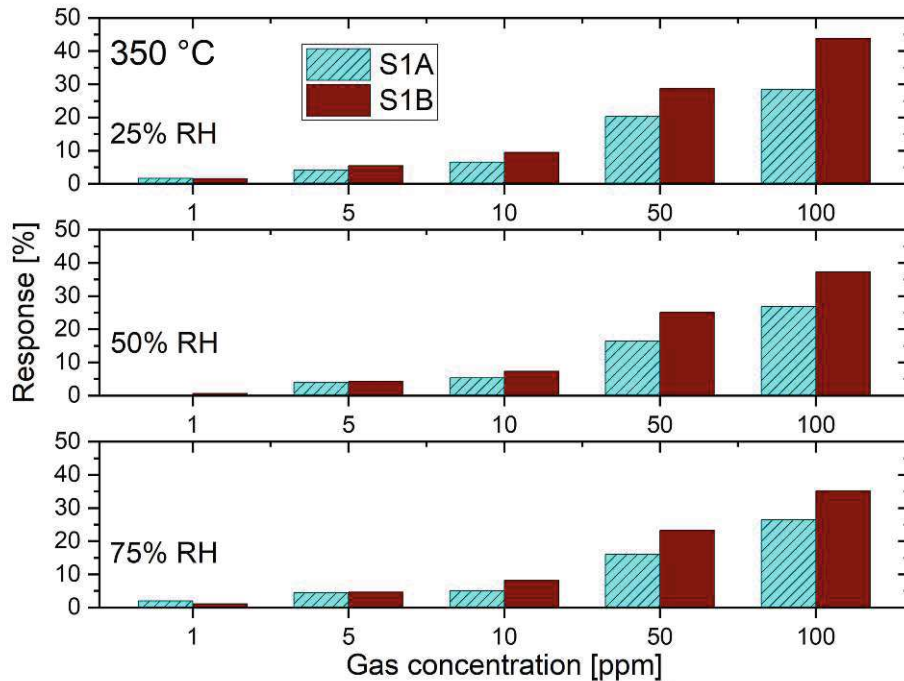

Figure 3.55: Resistance of two APPS gas sensors based on SnO_2 nanowires towards HCMix (0.5 ppm, 1 ppm, 5 ppm, 10 ppm, 50 ppm and 100 ppm) at 350°C operation temperature and at three different relative humidity levels: 25%, 50% and 75%.

Toluene measurements

The response towards toluene was measured for SnO_2-based, manually transferred nanowires sensors - the same sensors were used for measurements towards CO and HCMix. The protocol of the measurement is as follows:

- Toluene concentrations: 0.5 ppm, 1 ppm, 5 ppm

- Relative humidity levels: 25%, 50%, 75%

- Temperature: 350°C

- Constant current mode - 10 nA

Two APPS sensors (sensor 1A and sensor 1B) were measured simultaneously in GMS2 (check 3.3.2) towards toluene at 350°C operation temperature (Fig. 3.57). The resistance

decreases in the presence of the testing gas, which shows that both sensors are sensitive towards toluene in a typical manner for an n-type semiconductor like SnO_2.

Figure 3.56: Response of two APPS gas sensors based on SnO_2 nanowires towards HCMix (0.5 ppm, 1 ppm, 5 ppm, 10 ppm, 50 ppm and 100 ppm) at 350°C operation temperature and at three different relative humidity levels: 25%, 50% and 75%.

The base resistance changes with the humidity level. For sensor 1A, the base resistance is 29 MΩ at 25% relative humidity, 27 MΩ at 50% relative humidity, and 26 MΩ at 75% relative humidity. For sensor 1B, the base resistance is 37 MΩ at 25% relative humidity, 35 MΩ at 50% relative humidity, and 35 MΩ at 75% relative humidity. The base resistance of both sensor is higher as the base resistance measured during CO and HCMix measurements (the measurements are presented in the same order as they were taken, so CO, HCMix, toluene, H_2S). The sensor's baseline resistance may drift due to continuous exposure of the sensor to high temperature or humidity. This drift frequently results in an increase in base resistance. Long-term exposure to humidity can introduce hydroxyl groups on the MOx surface, which can increase the base resistance.

The sensor response is shown in Fig. 3.58: towards 0.5 ppm toluene and at 25% RH sensor 1A and sensor 1B show the highest response of 1%, and 2%. The response increases with increasing concentration up to 9%, and 11% for 5 ppm toluene, respectively. Response towards toluene is similar for all humidity levels, for example for sensor 1A the response

towards 5 ppm toluene at 25%, 50%, and 75% RH is 9%, 9%, and 8%, respectively. This indicates again a low cross-sensitivity of SnO_2 nanowires towards water.
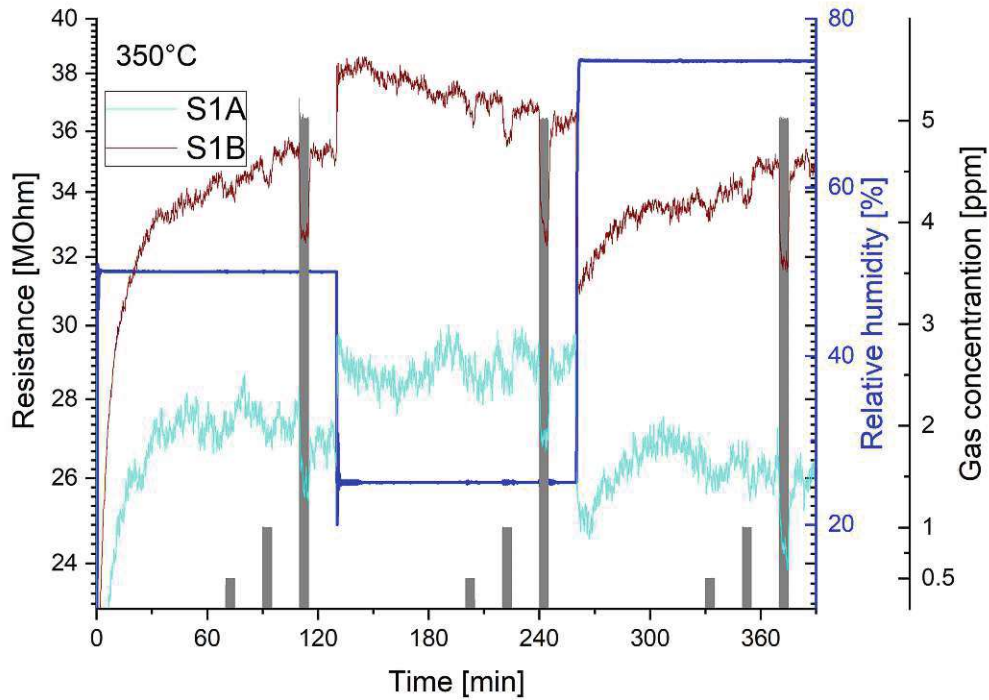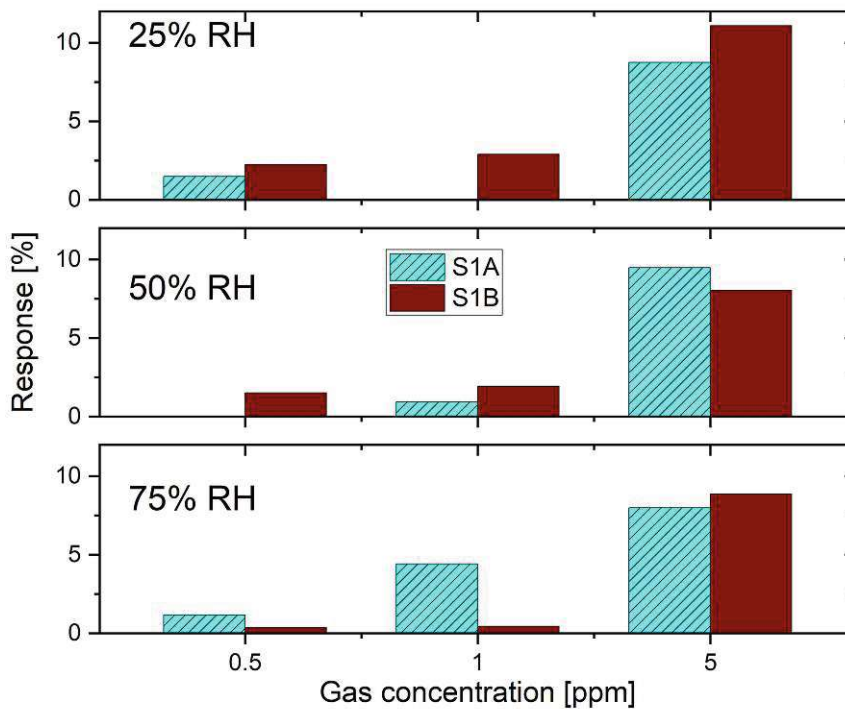

Figure 3.57: Resistance of two APPS gas sensors based on SnO_2 nanowires towards toluene (0.5 ppm, 1 ppm, 5 ppm) at 350°C operation temperature and at three different relative humidity levels: 25%, 50% and 75%.

H_2S measurements

The response towards H_2S was measured for SnO_2-based, manually transferred nanowires sensors - the same sensors were used for measurements towards CO, HCMix and toluene. The protocol of the measurement is as follows:

- H_2S concentrations: 0.5 ppm, 1 ppm, 5 ppm

- Relative humidity levels: 25%, 50%, 75%

- Temperature: 350°C
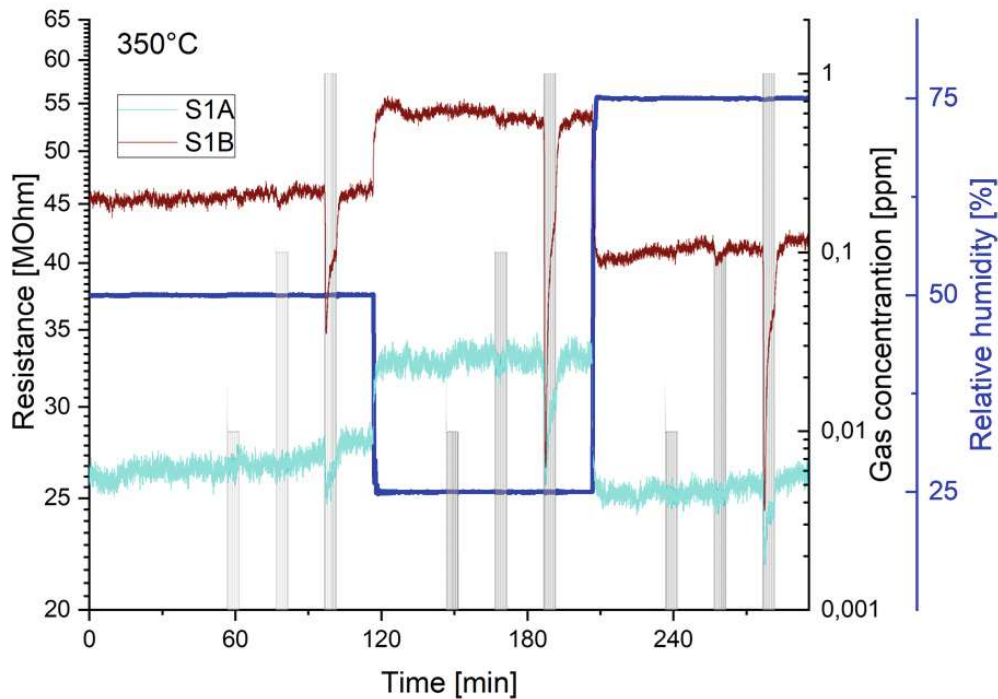
- Constant current mode - 10 nA

101

Figure 3.58: Response of two APPS gas sensors based on SnO_2 nanowires towards toluene (0.5 ppm, 1 ppm, 5 ppm) at 350°C operation temperature and at three different relative humidity levels: 25%, 50% and 75%.

Two APPS sensors (sensor 1A and sensor 1B) were measured simultaneously in GMS2 (check 3.3.2) towards H_2S at 350°C (Fig. 3.59). The resistance decreases in the presence of the testing gas, which shows that both sensors are sensitive towards H_2S in a typical manner for an n-type semiconductor like SnO_2. The base resistance changes with the humidity level. For sensor 1A, the base resistance is 33 MΩ at 25% relative humidity, 27 MΩ at 50% relative humidity, and 26 MΩ at 75% relative humidity. For sensor 1B, the base resistance is 54 MΩ at 25% relative humidity, 46 MΩ at 50% relative humidity, and 41 MΩ at 75% relative humidity. The cross-sensitivity towards water is higher with each measurement - which indicates higher amount of hydroxyl groups on the MOx surface, and subsequently an increase in the base resistance (for sensor 1B, CO measurement, 25% RH it was 32 MΩ, now for H_2S, 25% RH - 54 MΩ).

The resistance curves of the SnO_2-nanowire based sensors towards H_2S show very specific features: for 1 ppm there is a significant "overshoot" in the resistance decrease (the same as for the 100 ppb H_2S for SB sensors with SnO_2 nanowires). This feature is repeatable for other temperatures (300°C and 400°C, not included in this thesis), so most probably it appears due to the overload of the chemical reaction between H_2S and the MOx surface.

The sensor response is shown in Fig. 3.60: towards 10 ppb and 100 ppb H_2S sensor 1A and sensor 1B show negligible response. The response towards 1 ppm H_2S at 25% RH is 7%, and 18%, respectively. Both sensors (1A and 1B) show a similar behaviour concerning relative humidity level - the highest response is achieved by the lowest relative humidity level of 25%, which means that the sensor is cross-sensitive towards water. The SB sensors with SnO_2 nanowires is much more sensitive towards H_2S(5-9% at 25% RH, 10 ppb; 24-37% for 1 ppm), but less sensitive towards CO (SB: 12-18% at 25% RH, 200 ppm, APPS: 34%, same conditions), which indicates that the sensing platform has a significant influence on the MOx sensing behaviour. This might have to do also with the type of electrodes, which are used for contacting the nanowires. In case of the APPS-based sensor platform, Pt-electrodes are employed, while the SB sensors use Au-electrodes. Similar, as Pt- and Au-NPs, the electrode material might trigger some chemical reaction.

Figure 3.59: Resistance of two APPS gas sensors based on SnO_2 nanowires towards H_2S (10 ppb, 100 ppb and 1 ppm) at 350°C operation temperature and at three different relative humidity levels: 25%, 50% and 75%.
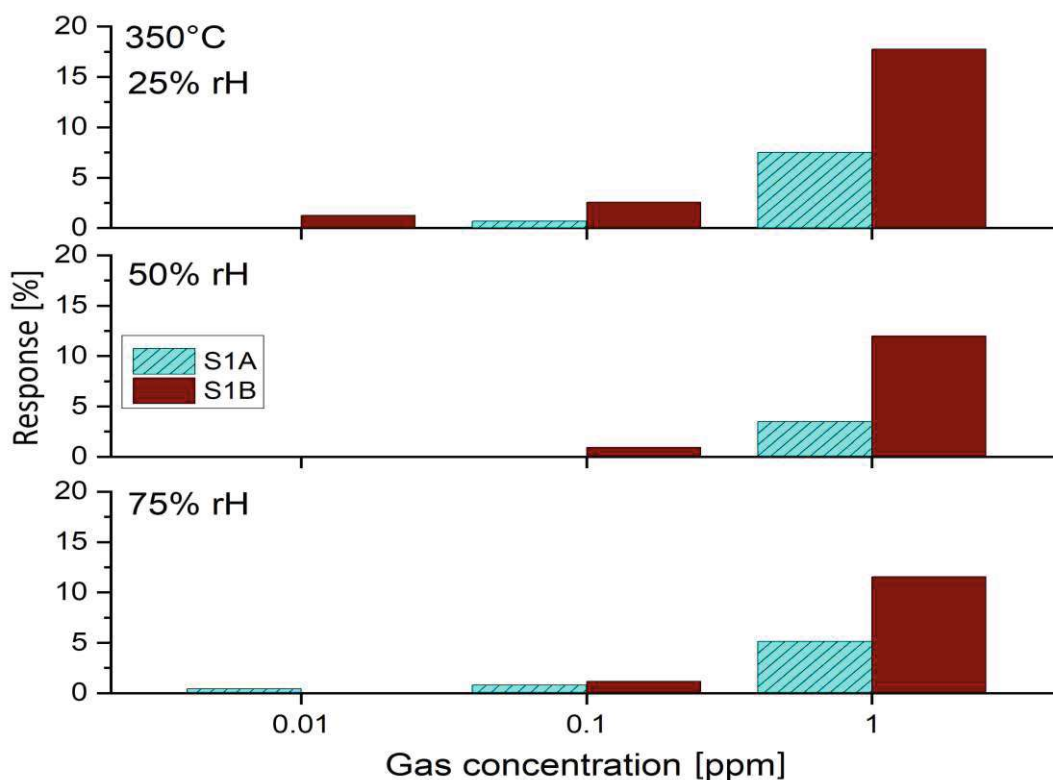
Figure 3.60: Response of two APPS gas sensors based on SnO_2 nanowires towards H_2S (10 ppb, 100 ppb and 1 ppm) at 350°C operation temperature and at three different relative humidity levels: 25%, 50% and 75%.

3.3.6 Result for MPW4 sensor

CO measurement

The response towards carbon monoxide was measured for two different microhotplates with SnO_2 nanowires transferred with a bond tester, and a flat PDMS stamp. The assembly process was described in Chapter 3.3.1 and the transfer in Chapter 3.2.5). The gas measurement methodology was described in Chapter 3.3.3. The protocol of the measurement is as follows:

- CO concentration: 50 ppm

- Relative humidity levels: 25%, 50%
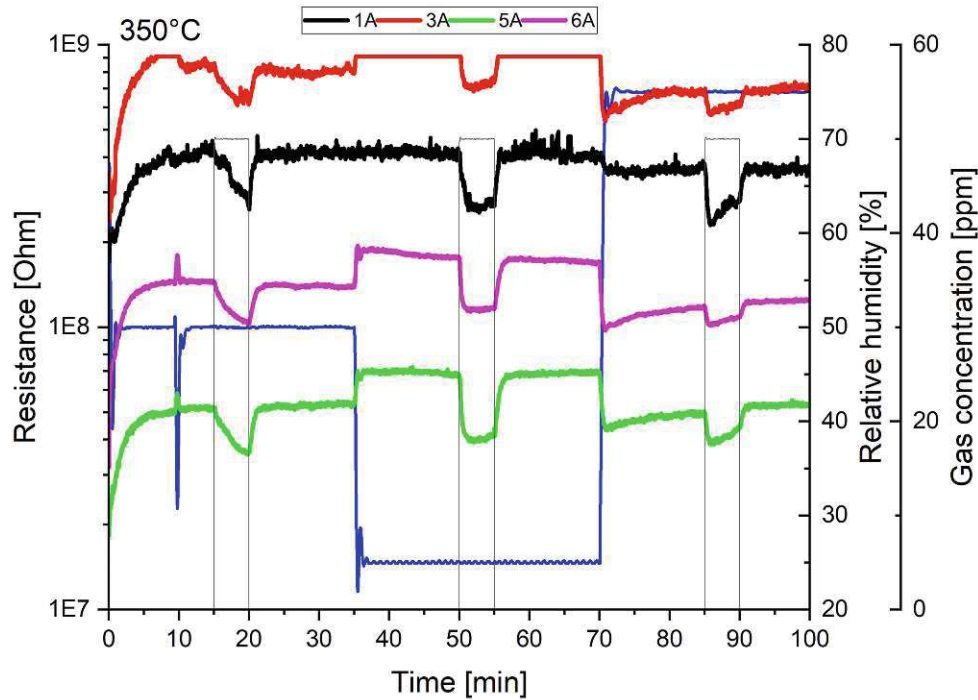
- Temperature: 350°C

- Constant current mode - 10 nA

The resistance values are in a very high range (hundreds of MOhms) hence we conclude that only a few nanowires were transferred onto the IDE structure on the µhp. The resistance exhibits a very noise behaviour, however, still the response to CO can be detected. There is a decrease of resistance in the presence of CO, which shows that both sensors (on µhp 3 and µhp 7) are sensitive towards CO in a typical manner for an n-type semiconductor like SnO_2. Both sensors show also a change of resistance baseline when changing from 50% relative humidity to 25% - which means that the sensor is cross-sensitive towards water. For µhp 3, the base resistance is 210 MΩ at 50% relative humidity, and 280 MΩ at 25% relative humidity. For µhp 7, the base resistance is 400 MΩ at 50% relative humidity, and 460 MΩ at 25% relative humidity.
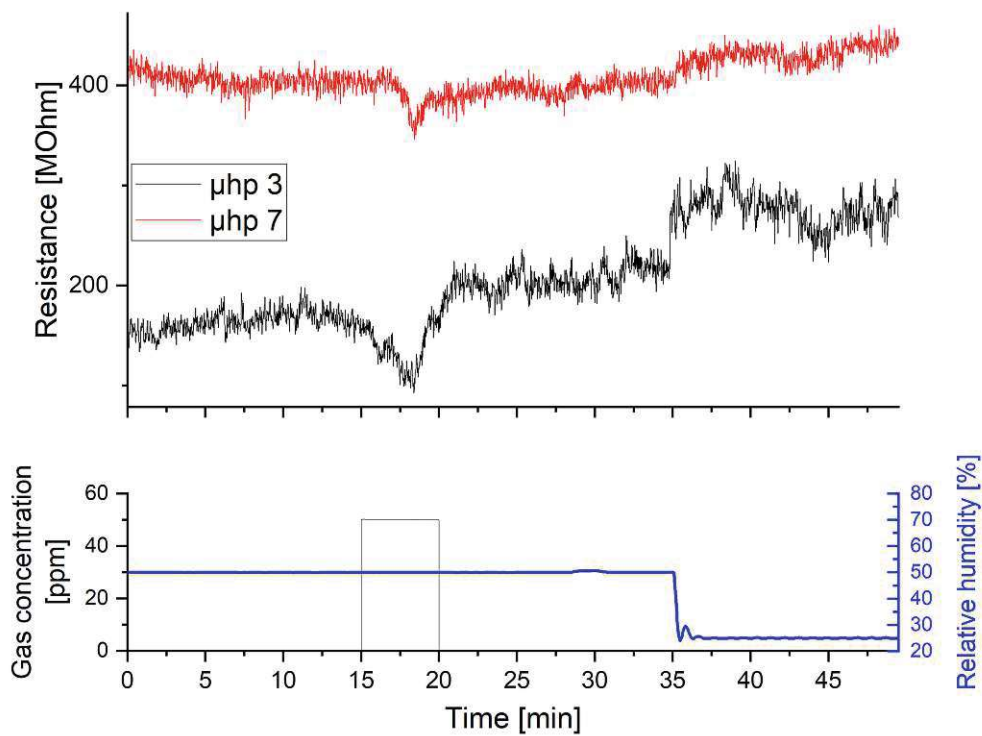
Figure 3.61: Resistance of two microhotplates on MPW4 chip (transfer with flat PDMS), based on SnO_2 nanowires towards 50 ppm CO at 350°C operation temperature and at two different relative humidity levels: 25% and 50%.

The response towards CO was also measured for four other microhotplates with SnO_2 nanowires transferred with the bond tester, but with the structured stamp (see Chapter 3.2.5). The protocol of the measurement is as follows:

- CO concentration: 50 ppm

- Relative humidity levels: 50%, 25%, 75%

- Temperature: 350°C

- Constant current mode - 10 nA

Figure 3.62: Resistance of four microhotplates on MPW4 chip (transfer with structured PDMS), based on SnO_2 nanowires towards 50 ppm CO at 350°C operation temperature and at three different relative humidity levels: 50%, 25%, and 75%.

The resistance values are in a range of hundreds of MOhms, which again means that only a few nanowires were transferred onto the IDE structure. The resistance of nanowires on microhotplate 3 is in such high range, that it cannot be measured with the equipment used in the measurement setup (compliance). The resistance decreases in the presence of CO, which shows that all sensors are reacting in a typical manner for an n-type semiconductor like SnO_2. The base resistance changes with the humidity level. For sensor 1A, the base resistance is 415 MΩ at 25% relative humidity, 415 MΩ at 50% relative humidity, and 350 MΩ at 75% relative humidity. For sensor 3A, the base resistance is in compliance level (not measurable) at 25% relative humidity, 800 MΩ at 50% relative

humidity, and 700 MΩ at 75% relative humidity. For sensor 5A, the base resistance is 68 MΩ at 25% relative humidity, 53 MΩ at 50% relative humidity, and 53 MΩ at 75% relative humidity. For sensor 6A, the base resistance is 170 MΩ at 25% relative humidity, 140 MΩ at 50% relative humidity, and 120 MΩ at 75% relative humidity. All sensors show also a change of resistance base level when changing relative humidity levels - which means that the sensors are cross-sensitive towards water.

The sensor response is shown in Fig. 3.63: towards 50 ppm CO at 25% RH the sensor responses are 34%, 17% (but here the base resistance is in compliance regime, so the response is certainly even higher), 39%, and 34% for sensors 1A, 3A, 5A, and 6A, respectively. All sensors show a similar behaviour concerning relative humidity level - the highest response is achieved by the lowest relative humidity level of 25%, which proves again the cross-sensitivity towards water.
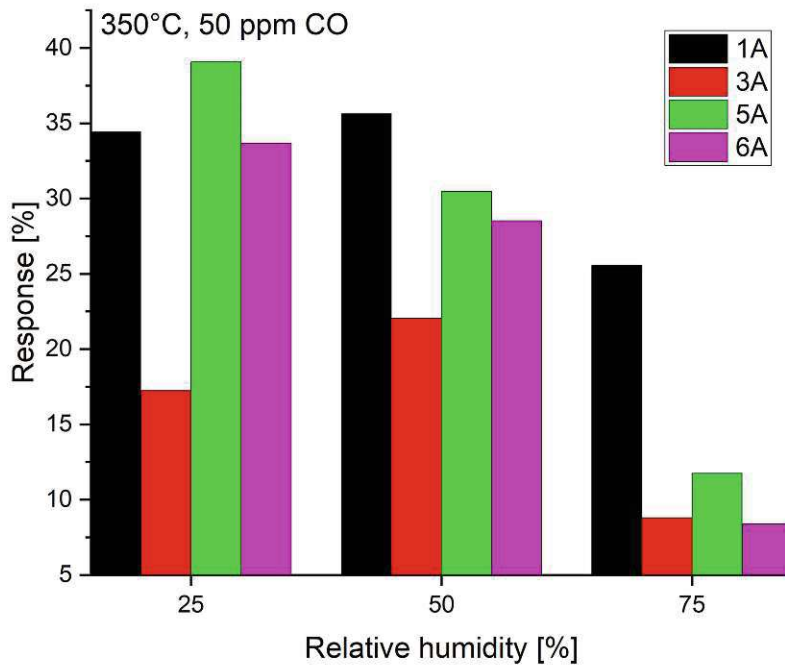

Figure 3.63: Response of four microhotplate-based sensors on MPW4 chip (transfer with structured PDMS), based on SnO_2 nanowires towards 50 ppm CO at 350°C operation temperature and at three different relative humidity levels: 50%, 25%, and 75%.

HCMix measurement

The response towards HCMix was also measured for four different microhotplates with SnO_2 nanowires transferred with a bond tester with a structured stamp (Fig. 3.64).. The

107

protocol of the measurement is as follows:

- HCMix concentration: 10 ppm

- Relative humidity levels: 50%, 25%, 75%

- Temperature: 350°C
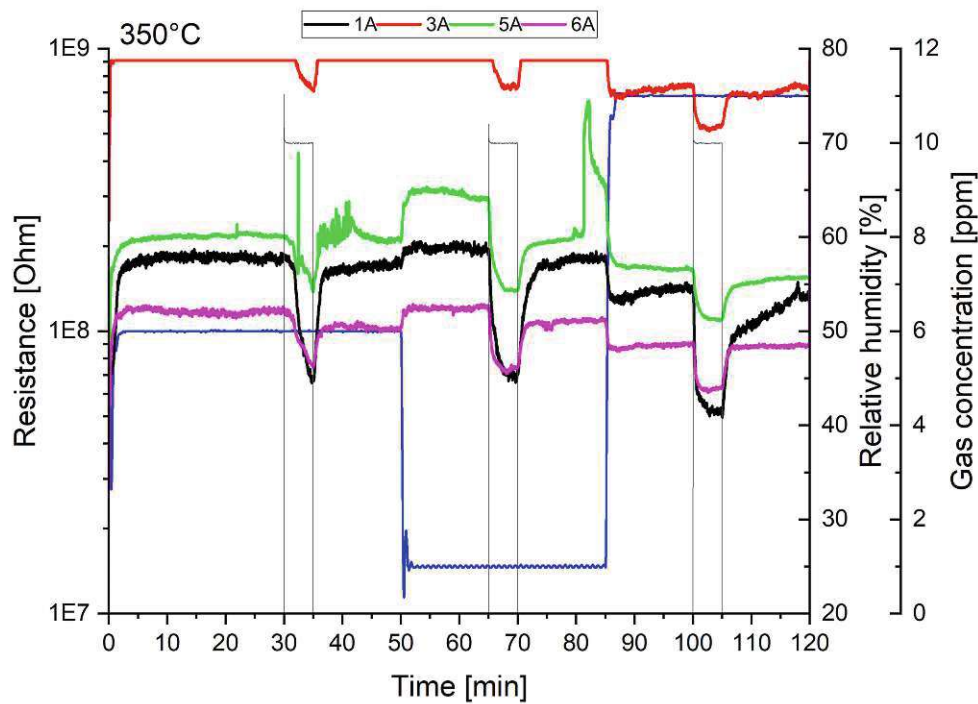
- Constant current mode - 10 nA

Figure 3.64: Resistance of four microhotplate-based sensors on the MPW4 chip (transferred with structured PDMS), based on SnO_2 nanowires towards 10 ppm HCMix at 350°C operation temperature and at three different relative humidity levels: 50%, 25%, and 75%.

The resistance of the nanowires on microhotplate 3 is again in compliance regime (not measurable), so the response values are not reliable. The resistance decreases in the presence of HCMix, which shows that all sensors are reacting in a typical manner for an n-type semiconductor like SnO_2. The base resistance changes with the humidity level. For sensor 1A, the base resistance is 180 MΩ at 25% relative humidity, 170 MΩ at 50% relative humidity, and 130 MΩ at 75% relative humidity. For sensor 3A, the

base resistance is in compliance level at 25% and 50% relative humidity, and 740 MΩ at 75% relative humidity. For sensor 5A, the base resistance is 300 MΩ at 25% relative humidity, 220 MΩ at 50% relative humidity, and 160 MΩ at 75% relative humidity. For sensor 6A, the base resistance is 115X MΩ at 25% relative humidity, 110 MΩ at 50% relative humidity, and 87 MΩ at 75% relative humidity. All sensors show also a change of resistance base level when changing relative humidity levels - which means that the sensors are cross-sensitive towards water.

The sensor response is shown in Fig. 3.65: towards 10 ppm HCMix at 25% RH the sensor responses are 65%, 19% (but here the base resistance is in compliance regime, so it is probably larger), 52%, and 39% for sensors 1A, 3A, 5A, and 6A, respectively. All sensors (except 3A, due to the compliance regime) show a similar behaviour concerning relative humidity level - the highest response is achieved by the lowest relative humidity level of 25%, which proves again the cross-sensitivity towards water. The differences between responses towards HCMix at different humidity levels are much lower than for CO - which can be used for selectivity evaluation of the sensors.
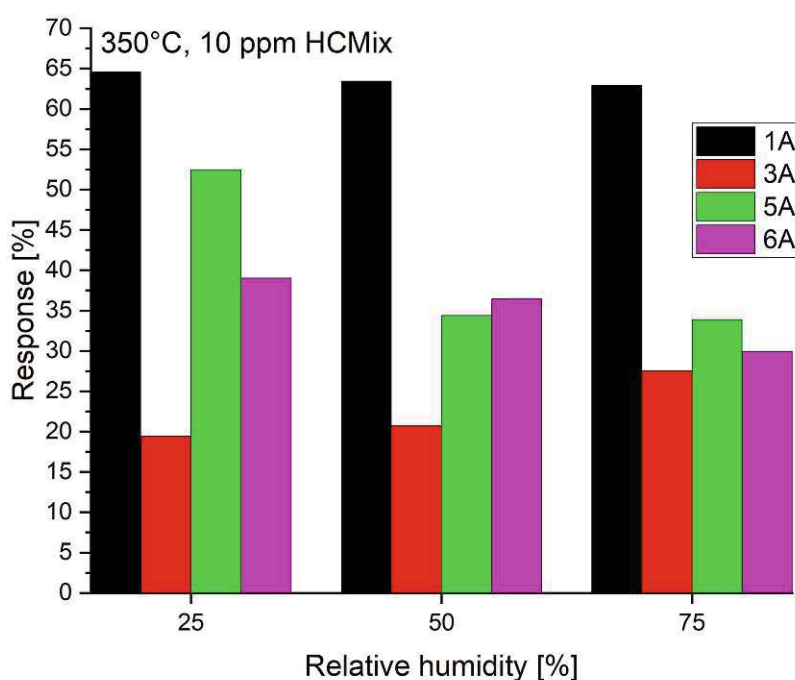

Figure 3.65: Response of four microhotplate-based sensors on the MPW4 chip (transferred with structured PDMS), based on SnO_2 nanowires towards 10 ppm HCMix at 350°C operation temperature and at three different relative humidity levels: 50%, 25%, and 75%.

Summary

The goal of this thesis was to explore new methods for the integration of metal oxide nanowires into electrode structures to enable exploitation of nanowire-based gas sensing devices. The most important metal oxide nanowires growth methods were presented, in particular three different growth methodologies were used to grow three different metal oxides:

- Thermal oxidation for CuO nanowires

- Spray pyrolysis and annealing for SnO_2 nanowires

- Hydrothermal synthesis for WO_3 nanowires.

In principle, all of those methods can be used for large scale production of nanowires. The metal oxide nanowires were also investigated by different characterisation methods - in-situ during growth (CuO nanowires) and after the growth (SEM, TEM, Raman analysis). All three types of metal oxide nanowires were transferred with four different media by transfer printing technology. For CuO and SnO_2 nanowires the PDMS stamp based method was the most successful one; for WO_3 nanowires the Blue Low Tack Tape was found to be the best option to transfer the nanowires.

After nanowire transfer the samples were investigated by SEM and AFM. Experiments with PDMS stamp demonstrated also that the geometrical structure of nanowires grown on the donor substrate is transferred onto the final substrate, which is of high importance to effectively integrate nanowires on very specific electrode and sensor structures.

To achieve better control over the transfer process, a bond tester was also applied. This machine can precisely move in X, Y, Z directions and also measures the force of pressing the stamp to pick up the nanowires and to transfer them onto the final substrate. This allowed for precise transfer of nanowires onto the MEMS-based chips with a SiN-based

microhotplate (APPS) and even on a CMOS-based microhotplate chip (MPW4, ams AG). The APPS microhotplate is a fragile 900 nm thin SiN membrane - but it is strong enough to withstand the mechanical pressing (manual and by bonder) of a stamp or tape. Also the 8 µm thick CMOS integrated microhotplate on a MPW4 chip, which is fully suspended in air, could withstand the transfer process.

The gas sensing performance was measured towards a variety of target gases relevant for air quality monitoring: CO, H_2S, HCMix and toluene. The responses were also calculated for each of the measurement and were presented, response times and recovery times were also calculated (see Appendix A). The following sensor devices were successfully fabricated and characterized:

- 2 SB gas sensors based on SnO_2 nanowires (manual transfer) towards CO at 300° - Table A.1

- 2 SB gas sensors based on WO_3 nanowires (manual transfer) towards CO at 250°C - Table A.2

- 3 SB gas sensors based on SnO_2 nanowires (manual transfer) towards H_2S at 350°C - Table A.3

- 1 SB gas sensor based on WO_3 nanowires (manual transfer) towards H_2S at 400°C - Table A.4

- 2 APPS gas sensors based on SnO_2 nanowires (manual transfer - S1A and S1B) towards CO at 350° - Table A.5

- 1 APPS gas sensor based on SnO_2 nanowires (manual transfer - S1A) towards CO at 350° with time difference of 2 years - Table A.6

- 3 APPS gas sensors (transferred manually - S1A and transferred with a bonder - S2A and S2C) based on SnO_2 nanowires towards CO at 350° - Table A.7

- 2 APPS gas sensors based on SnO_2 nanowires (manual transfer - S1A and S1B) towards HCMix at 350° - Table A.8

- 2 APPS gas sensors based on SnO_2 nanowires (manual transfer - S1A and S1B) towards toluene at 350° - Table A.9

- 2 APPS gas sensors based on SnO_2 nanowires (manual transfer - S1A and S1B) towards H_2S at 350° - Table A.10

- 3 MPW4 gas sensors based on SnO_2 nanowires (bonder-based transfer with a structured PDMS stamp) towards CO and HCMix at 350° - Table A.11

The gas response towards CO was measured for SnO_2 nanowires and WO_3 nanowires based SB gas sensors. Sensors show a similar behaviour concerning relative humidity

level - the highest response is achieved for the lowest relative humidity level of 25%, this means that the sensors obtain a cross-sensitivity towards humidity. The response times and recovery times for both metal oxides are mostly increasing with CO concentrations. The resistance plots show that the resistance during the gas pulse does not stabilize and decreases until the end of the gas pulse. This might be due to the fact that the reaction with the analysed gas does not achieve an equilibrium yet and the response could be potentially higher for longer gas pulse duration. For CO concentrations closer to the maximum allowed concentration at the workplace - 30 ppm the SnO_2 nanowires based gas sensors have lower response times. This type of metal oxide nanowires requires less time to achieve equilibrium with humidity - resistance level stabilizes quicker than for WO_3nanowires. This is potentially related to a lower operational temperature (for WO_3nanowires). The electrical resistance of WO_3nanowire based gas sensors is by a factor of 10 higher than for SnO_2 nanowires. This is most probably due to the fact that less nanowires interconnect the electrodes and that the nanowire resistance is higher due to the lower diameter of the WO_3 nanowires (10-30 nm for WO_3 nanowires and 70-250 nm for SnO_2 nanowires).

The gas response towards H_2S was measured for SnO_2 nanowires and WO_3 nanowires based SB gas sensors. The highest response is achieved for the lowest relative humidity level of 25% but it is not linearly dependent from the relative humidity level. It could be related with the possibility of creating water molecules during H_2S reaction with pre-adsorbed oxygen molecules (see Eq. 2.14) and adsorption of those water molecules as hydroxyl groups to the metal oxide again. Response times of 8-11s for gas concentration of 100 ppb (maximum allowed concentration at the workplace is 5 ppm) for all relative humidity levels were achieved for sensors based on SnO_2 nanowire. This fast sensor response is very important and enables early warning in case of high H_2S concentrations. The gas response is approximately 2 times higher for WO_3 nanowires based SB gas sensor than for SnO_2 nanowires based ones (70% vs 25-35% towards 1 ppm of H_2S). This can be explained by higher material sensitivity of WO_3 towards H_2S and higher operating temperature (400°C vs 350°C). Comparing resistance plots for SnO_2 nanowires based SB gas sensors for CO (300°C) and H_2S (350°C) the equilibrium for relative humidity level is achieved faster for the higher temperature. This is consistent with expectations: the reaction times are lower at higher temperatures, which results in fast achievement of a stable "base resistance line".

The gas response towards CO was measured for SnO_2 nanowires based APPS gas sensors. The sensors response in different relative humidity levels show very small humidity dependence - which means that the measurement platform choice is crucial for gas sensing activity. In this case the Pt-base electrodes might be responsible for this behaviour. The response and recovery times for 30 ppm of CO for both APPS sensors with manually transferred nanowires are similar (17-24s response time for S1A and S1B, 19-40s recovery times, at all humidity levels, see Table A.5), responses of both sensors towards all CO concentrations are similar. This implicates a successful transfer process and reasonable repeatability in terms of different devices.

The repeatability and sensor stability were also proven by repeating a CO measurement 2 years after the first measurement. This experiment showed a slight shift towards higher resistances of the sensor, but the sensor responses are very similar.

The sensors realized by the nanowire transfer method employing the bond tester were also characterised. For 30 ppm of CO their response and recovery times are similar. The response times for S2A and S2C are 18s and 16s for 25% rH, 20s and 12s for 50% rH, and 25s and 25s for 75% rH, respectively. The recovery times for S2A and S2C are 28s and 25s for 25% rH, 49s and 24s for 50% rH, 39s and 22s for 75% rH, respectively. The sensor response towards CO of the two sensors are almost equal, which proves that the transfer processes with use of PDMS stamp and a bond tester were successful and repeatable.

The sensor response towards HCMix and toluene was measured for SnO_2 nanowires based APPS gas sensors. The sensors show a similar behaviour concerning relative humidity level - the highest response (for both gases) is achieved for the lowest relative humidity level of 25%, hence the sensors exhibit a cross-sensitivity towards humidity. For a higher HCMix concentrations (50 ppm and 100 ppm) the sensors have fast response times around 20s. Usually, TVOC amount in the buildings mostly do not exceed 6 ppm [232] - the response towards HCMix in this region of gas concentrations is too small to use it in a commercial device (a few percent). The response towards toluene below 5 ppm cannot be considered - it is too much noise in the resistance signal, but for 5 ppm the response and recovery times are quite high - from 40s to even almost 270s - which is too slow for practical application.

The gas response towards H_2S was measured for SnO_2 nanowires based APPS sensors. Sensors show a similar behaviour concerning relative humidity level: the highest response is achieved for the lowest relative humidity level of 25%, hence the sensors exhibit a cross-sensitivity towards humidity (like for HCMix and toluene). For the highest H_2S concentration of 1 ppm the sensors show fast response times - all below 26s. There is also a specific shape of the resistance curve - the resistance drops at the beginning of the gas pulse 2-3 times lower than the calculated R_{gas} - which could be used as an indicator for this specific gas to improve gas selectivity.

The gas response towards CO was measured for SnO_2 nanowires based MPW4 gas sensors, where the nanowires were transferred with a flat and a structured PDMS stamp. For a flat PDMS stamp, as already mentioned in Sec. 3.3.6, the CO gas measurement was performed only as a proof-of-concept and showed that the PDMS stamp can transfer nanowires not only on Si-based structures, but also on membranes and even suspended μhps. For a higher precision a special form for a PDMS stamp was designed and applied for the nanowires transfer. The sensors have been then tested for gas sensitivity towards 50 ppm CO and 10 ppm HCMix. Comparing MPW4-based sensors to APPS-based (both operated at 350°C), the sensors response is higher for the MPW4-based sensors: for 25% rH and 60 ppm CO the APPS-based sensors have 20-22% response, the MPW4-based sensors have a response of 34-39% towards 50 ppm of CO, also at 25% rH. Towards 10 ppm HCMix (25% rH) the APPS-based sensors have a response of 7-10%, the MPW4-based sensors have a higher response of 39-65%, which indicates more successful transfer of

Table 4.1: SnO$_2$ NWs based gas sensors comparison.

Sensor description	Gas concentration [ppm]	Conditions	Response	Source
CARBON MONOXIDE				
this work, SnO$_2$ NWs on APPS (1A)	10	25% rH, 350°C	7% (1,09*)	
SnO$_2$ NWs spaghetti-like line 10x100µm	10	0% rH, 250°C	7%	[234]
SnO$_2$ NWs spaghetti-like, with Pd NPs	10	0% rH, 400°C	2,4*	[235]
multi-SnO$_2$ NW device (100µm between electrodes)	20	0% rH, 25°C	4*	[126]
HYDROGEN SULFIDE				
This work, SnO$_2$ NWs on APPS (1A)	1	25% rH, 350°C	7% (1,08*)	
single SnO$_2$ NW, 10µm long	4	0% rH, 25°C	15* no doping, 2* with Cu doping	[236]
single Sb $-$ SnO$_2$ nanoribbon	1	0% rH, 150°C	17*	[237]

* response was calculated with the formula: S $= \frac{R_{air}}{R_{gas}}$

nanowires with structured PDMS stamp. The recovery times for MPW4 sensors are high (mostly more than 300s), because the resistance does not fully recover after the gas pulse into its initial level, which indicates that the desorption of the reaction products (hydrocarbons, CO$_2$ or water) and re-adsorption of oxygen on the metal oxide surface are both slow processes. [233]

Table 4.1 shows a comparison of different gas sensing devices and their responses, all based on SnO$_2$ nanowires. In the literature the response is also calculated with a different formula, also included inside the table. All the examples presented in the table have measured the gas sensing without humidity (dry air), which has a great impact on the sensing performance. Single nanowire devises have a great potential due to their high response even at room temperature (self-heating effect), but unfortunately require high cost and time-consuming equipment for electrical contact deposition (i.e. E-BEAM lithography) and are not suitable for practical applications. The Pd-NPs have increased the sensing response and are one of the ways to optimize the nanowire-based devices in

the future, which is discussed below.

In summary the results demonstrate the high potential of nanowire based gas sensors. Further optimization will include the following experiments:

- More detailed experiments for precisely adjusting the force of the bond tester for picking up the nanowires from the donor substrate would certainly lead to better performance of the transfer and, simultaneously, to a better gas sensing performance. Moreover, different metal oxides nanowires could be transferred on each of the microhotplate to realize a multi-gas sensor device, which would improve the selectivity of the whole device.

- Improvement of the sensitivity and selectivity of the specific metal oxides nanowires by functionalization with metallic nanoparticles. This has been already demonstrated in our group at Materials Center Leoben Forschung GmbH in case of MOx thin films and could be also employed for the nanowire-based devices. [14, 238]

- Employment of a structured PDMS stamp to enhance the local transfer of nanowires. In this case the geometry, where the nanowires are grown on the donor substrate, can be exactly matched to the requirements of the sensor chips. In this case also the number of finally transferred nanowires would be optimized to increase the sensitivity of the final sensor devices. This could be even performed on a full wafer scale by using tools dedicated to nanoimprint lithography.

List of Figures

117

121

Bibliography

[1] Siemens AG. "Clean buildings along with resource efficiency enhancement using appropriate materials and technology". In: *CLEAR-UP FP7 Project, Grant agreement ID: 211948* (2011).

[2] The European Parliament and of the Council. "Directive (EU) 2016/2284 of the European Parliament and of the Council of 14 December 2016 on the reduction of national emissions of certain atmospheric pollutants, amending Directive 2003/35/EC and repealing Directive 2001/81/EC". In: *Official Journal of the European Union* L 334/1 (14th Dec. 2016).

[3] Geneva: World Health Organization. "World Health Organization (WHO) Global Air Quality Guidelines. Particulate matter (PM2.5 and PM10), ozone, nitrogen dioxide, sulfur dioxide and carbon monoxide". In: *Licence: CCBY-NC-SA 3.0 IGO* (2021).

[4] Briefing no. 06/2024. "Europe's air quality status 2024". In: *ISBN: 978-92-9480-650-5* (2024).

[5] "U.S. Environmental Protection Agency. 1989. Report to Congress on indoor air quality: Volume 2". In: *EPA/400/1-89/001C* ().

[6] Energieeinsatz der Haushalte. *Austria, Statistik*. URL: https://www.statistik.at/statistiken/energie-und-umwelt/energie/energieeinsatz-der-haushalte (visited on 01/11/2024).

[7] R. J. Martín-Palma, F. Agulló-Rueda and J. Martínez-Duart. *Nanotechnology for microelectronics and optoelectronics*. Elsevier, 2006.

[8] G. Korotcenkov. "Gas response control through structural and chemical modification of metal oxide films: state of the art and approaches". In: *Sensors and Actuators B: Chemical* 107.1 (2005), pp. 209–232. DOI: 10.1016/j.snb.2004.10.006.

[9] N. Barsan, D. Koziej and U. Weimar. "Metal oxide-based gas sensor research: How to?" In: *Sensors and Actuators B: Chemical* 121.1 (2007), pp. 18–35. DOI: 10.1016/j.snb.2006.09.047.

[10] M. Fleischer and M. Lehmann. *Solid State Gas Sensors-Industrial Application*. Vol. 11. Springer Science & Business Media, 2012.

[11] C. Gamauf, M. Siegele, A. Nemecek, G. C. Mutinati et al. "Fully integrated System-On Chip gas sensor in CMOS technology". In: *SENSORS, 2013 IEEE*. IEEE. 2013, pp. 1–4. DOI: 10.1109/ICSENS.2013.6688155.

[12] A. Köck, M. Deluca, F. Sosada-Ludwikowska, G. Maier et al. "Heterogeneous Integration of Metal Oxides - Towards a CMOS Based Multi Gas Sensor Device". In: *Proceedings*. Vol. 14. 1. MDPI. 2019, p. 5. DOI: 10.3390/proceedings201 9014005.

[13] E. Brunet, T. Maier, G. C. Mutinati, S. Steinhauer et al. "Comparison of the gas sensing performance of SnO2 thin film and SnO2 nanowire sensors". In: *Sensors and Actuators B: Chemical* 165.1 (2012), pp. 110–118. DOI: 10.1016/j.snb.2 012.02.025.

[14] S. Steinhauer, E. Lackner, F. Sosada-Ludwikowska, V. Singh et al. "Atomic-scale structure and chemical sensing application of ultrasmall size-selected Pt nanoparticles supported on SnO2". In: *Materials Advances* 1.9 (2020), pp. 3200–3207. DOI: 10.1039/D0MA00244E.

[15] G. Heiland. "Zum Einfluß von adsorbiertem Sauerstoff auf die elektrische Leit-fähigkeit von Zinkoxydkristallen". In: *Zeitschrift für Physik* 138.3-4 (1954), pp. 459–464. DOI: 10.1007/BF01340692.

[16] N. Taguchi. *Gas-detecting device*. US Patent 3,631,436. 28th Dec. 1971.

[17] G. Korotcenkov and J. R. Stetter. "Comparative study of SnO2-and In2O3-based ozone sensors". In: *ECS Transactions* 6.20 (2008), p. 29. DOI: 10.1149/1.2831 341.

[18] K. Grossmann, U. Weimar and N. Barsan. "Semiconducting Metal Oxides Based Gas Sensors". In: *Semiconductors and Semimetals* 88 (2013), pp. 261–280. DOI: 10.1016/B978-0-12-396489-2.00008-4.

[19] Dr Luyun Jiang. *Environmental Gas Sensors 2020-2030. Technologies, manu-facturers, forecasts*. URL: https://www.idtechex.com/en/research-report/environmental-gas-sensors-2020-2030/718 (visited on 01/11/2024).

[20] W. Y. Yi, K. M. Lo, T. Mak, K. S. Leung et al. "A survey of wireless sensor network based air pollution monitoring systems". In: *Sensors* 15.12 (2015), pp. 31392–31427. DOI: 10.3390/s151229859.

[21] B. Szulczyński and J. Gębicki. "Currently commercially available chemical sensors employed for detection of volatile organic compounds in outdoor and indoor air". In: *Environments* 4.1 (2017), p. 21. DOI: 10.3390/environments4010021.

[22] *Operating principle of electrochemical gas sensor*. URL: https://www.figaro.c o.jp/en/technicalinfo/principle/electrochemical-type.html (visited on 01/11/2024).

[23] *Operating principle of catalytic gas sensor*. URL: https://www.figaro.co.jp/en/technicalinfo/principle/catalytic-type.html (visited on 01/11/2024).

[24] *Operating principle of NDIR gas sensor*. URL: https://www.figaro.co.jp/en/technicalinfo/principle/ndir-type.html (visited on 01/11/2024).

[25] *How PID Gas Detectors Work*. URL: https://www.rcsystemsco.com/photoionization-detectors (visited on 01/11/2024).

[26] *Operating principle of MOS gas sensor*. URL: https://www.figaro.co.jp/en/technicalinfo/principle/mos-type.html (visited on 01/11/2024).

[27] G. W. Hunter, S. Akbar, S. Bhansali, M. Daniele et al. "Editors' choice - critical review - a critical review of solid state gas sensors". In: *Journal of The Electrochemical Society* 167.3 (2020), p. 037570. DOI: 10.1149/1945-7111/ab729c.

[28] D. Popa and F. Udrea. "Towards integrated mid-infrared gas sensors". In: *Sensors* 19.9 (2019), p. 2076. DOI: 10.3390/s19092076.

[29] G. C. Rezende, S. Le Calvé, J. J. Brandner and D. Newport. "Micro photoionization detectors". In: *Sensors and Actuators B: Chemical* 287 (2019), pp. 86–94. DOI: 10.1016/j.snb.2019.01.072.

[30] R. K. Sharma, P. C. Chan, Z. Tang, G. Yan et al. "Sensitive, selective and stable tin dioxide thin-films for carbon monoxide and hydrogen sensing in integrated gas sensor array applications". In: *Sensors and Actuators B: Chemical* 72.2 (2001), pp. 160–166. DOI: 10.1016/S0925-4005(00)00646-8.

[31] The European Parliament and of the Council. "Directive 2010/75/EU of the European Parliament and of the Council of 24 November 2010 on industrial emissions (integrated pollution prevention and control)". In: *Official Journal of the European Union* L 334/17 (24th Nov. 2010).

[32] *CARBON MONOXIDE SENSORS*. URL: http://www.ddscientific.com/co-sensors.html (visited on 01/11/2024).

[33] *Alphasense 5,000ppm Carbon Monoxide Smart EC Sensor*. URL: https://www.co2meter.com/products/0-500ppm-carbon-monoxide-sensor (visited on 01/11/2024).

[34] *CO - Carbon Monoxide Sensor 1000 ppm*. URL: https://www.spec-sensors.com/product/carbon-monoxide-sensor-1000-ppm/ (visited on 01/11/2024).

[35] *TGS5141 [Carbon Monoxide Sensor]*. URL: https://www.figarosensor.com/product/entry/tgs5141-p00.html (visited on 01/11/2024).

[36] *Sensorix CO 500 Satellix*. URL: https://www.gfgsafety.com/int/sensors/satellix-sensors-by-sensorix/co/ (visited on 01/11/2024).

[37] *Draeger XXS Sensors, H2S-LC/CO-LC Dual Sensor*. URL: https://www.skcinc.com/products/draeger-xxs-sensors-h2s-lc-co-lc-dual-sensor (visited on 01/11/2024).

[38]   *Carbon Monoxide Detector 0-1000ppm*. URL: https://www.aeroqual.com/product/carbon-monoxide-sensor-0-1000ppm (visited on 01/11/2024).

[39]   *TGS3870 [Methane/Carbon Monoxide Sensor]*. URL: https://www.figarosensor.com/product/entry/tgs3870.html (visited on 01/11/2024).

[40]   *Carbon Monoxide Sensor MQ-7B*. URL: http://www.winsensor.com/ctbdt/MQ_7Byyhtcgq_12.html (visited on 01/11/2024).

[41]   *Alphasense CO-D4X*. URL: https://www.alphasense.com/products/carbon-monoxide-sensors/ (visited on 01/11/2024).

[42]   *Catalytic Flammable Gas Sensor*. URL: https://www.winsen-sensor.com/sensors/combustible-sensor/mc227d-catalytic-flammable-gas-sensor.html (visited on 01/11/2024).

[43]   *INFRARED CO CARBON MONOXIDE GASSENSE NDIR SENSOR*. URL: https://euro-gasman.com/product/carbon-monoxide-co-gassense-infrared-co-gas-sensor-with-analogue-transmitter/ (visited on 01/11/2024).

[44]   *Indoor Air Quality Module iAQ-2000*. URL: https://www.sensor-test.de/ausstellerbereich/upload/mnpdf/de/APS_iAQ2000_0809.pdf (visited on 01/11/2024).

[45]   *AS-MLV-P2 Air Quality Sensor*. URL: https://www.sciosense.com/wp-content/uploads/documents/AS-MLV-P2-Datasheet.pdf (visited on 01/11/2024).

[46]   *CCS801 Cambridge CMOS Sensors*. URL: http://www1.futureelectronics.com/doc/CAMBRIDGE%5C%20CMOS%5C%20SENSORS/CCS801B-COPS.pdf (visited on 01/11/2024).

[47]   *MiCS-5524*. URL: https://www.sgxsensortech.com/content/uploads/2014/07/1084_Datasheet-MiCS-5524-rev-8.pdf (visited on 01/11/2024).

[48]   *VOC-TRAQ II piD-TEC*. URL: https://www.ametekmocon.com/products/vocdetectors/voctraqiitoxicgasdetector (visited on 01/11/2024).

[49]   *PID AR-sensors*. URL: https://www.alphasense.com/pid-sensors/ (visited on 01/11/2024).

[50]   *VOC-A4*. URL: https://www.alphasense.com/wp-content/uploads/2022/09/Alphasense_VOC-A4_datasheet.pdf (visited on 01/11/2024).

[51]   *VOC-P31 p-type Metal Oxide*. URL: https://www.alphasense.com/wp-content/uploads/2022/09/Alphasense_MMO-VOC_datasheet.pdf (visited on 01/11/2024).

[52]   *4R-PID Winsen*. URL: https://www.winsen-sensor.com/sensors/air-quality-sensor/4r-pid.html (visited on 01/11/2024).

[53] *TGS2620 Figaro*. URL: https://www.figaro.co.jp/en/product/docs/tgs2620_product%5C%20information%5C%28en%5C%29_rev03.pdf (visited on 01/11/2024).

[54] *GGS 10530 T Umweltsensortechnik*. URL: https://www.umweltsensortechnik.de/fileadmin/assets/downloads/gassensoren/single/DataSheet-GGS-10530-T_Rev2203.pdf (visited on 01/11/2024).

[55] *VOC Gas Sensor VM-1001*. URL: https://en.gassensor.com.cn/VOCSensor/info_itemid_278.html%5C#box1 (visited on 01/11/2024).

[56] *SENS-IT UNITEC*. URL: http://www.unitec-srl.com/site/wp-content/uploads/2015/04/SENS-IT-Datasheet.pdf (visited on 01/11/2024).

[57] *P/N 707 Synkera*. URL: https://www.pmt-fl.com/uploads/2018/02/precision-measurement-synkera-datasheet-voc.pdf (visited on 01/11/2024).

[58] S. Dimitroulopoulou, M. R. Dudzińska, L. Gunnarsen, L. Hägerhed et al. "Indoor air quality guidelines from across the world: An appraisal considering energy saving, health, productivity, and comfort". In: *Environment International* 178 (2023), p. 108127. DOI: 10.1016/j.envint.2023.108127.

[59] Deutsche Forschungsgemeinschaft. "List of MAK and BAT Values 2023 (Maximum Concentrations and Biological Tolerance Values at the Workplace)". In: Report 59 (2023).

[60] M. Ye, P. J. Chien, K. Toma, T. Arakawa et al. "An acetone bio-sniffer (gas phase biosensor) enabling assessment of lipid metabolism from exhaled breath". In: *Biosensors and Bioelectronics* 73 (2015), pp. 208–213. DOI: 10.1016/j.bios.2015.04.023.

[61] J. van den Broek, P. Mochalski, K. Königstein, W. C. Ting et al. "Selective monitoring of breath isoprene by a portable detector during exercise and at rest". In: *Sensors and Actuators B: Chemical* 357 (2022), p. 131444. DOI: 10.1016/j.snb.2022.131444.

[62] K. Mitsubayashi, H. Matsunaga, G. Nishio, S. Toda et al. "Bioelectronic sniffers for ethanol and acetaldehyde in breath air after drinking". In: *Biosensors and Bioelectronics* 20.8 (2005), pp. 1573–1579. DOI: 10.1016/j.bios.2004.08.007.

[63] R. P. Huebener. *Conductors, Semiconductors, Superconductors*. Springer, 2019, pp. 43–49.

[64] C. Wang, L. Yin, L. Zhang, D. Xiang et al. "Metal oxide gas sensors: sensitivity and influencing factors". In: *sensors* 10.3 (2010), pp. 2088–2106. DOI: 10.3390/s100302088.

[65] M. Dou and C. Persson. "Comparative study of rutile and anatase SnO2 and TiO2: Band-edge structures, dielectric functions, and polaron effects". In: *Journal of Applied Physics* 113.8 (2013), p. 083703. DOI: 10.1063/1.4793273.

[66] T. Wolkenstein. *Electronic processes on semiconductor surfaces during chemisorption.* New York, USA: Plenum Publishing Corporation, 199.

[67] H. Lüth. *Solid surfaces, interfaces and thin films.* Vol. 4. Springer, 2001.

[68] N. Barsan and U. Weimar. "Conduction model of metal oxide gas sensors". In: *Journal of electroceramics* 7.3 (2001), pp. 143–167. DOI: 10.1023/A:10144058 11371.

[69] J. Vetelino and A. Reghu. *Introduction to sensors.* CRC press, 2017, pp. 37–41.

[70] M. J. Madou and S. R. Morrison. *Chemical sensing with solid state devices.* Elsevier, 2012.

[71] N. Barsan, C. Simion, T. Heine, S. Pokhrel et al. "Modeling of sensing and transduction for p-type semiconducting metal oxide based gas sensors". In: *Journal of electroceramics* 25.1 (2010), pp. 11–19. DOI: 10.1007/s10832-009-9583-x.

[72] S. M. Sze, Y. Li and K. K. Ng. *Physics of semiconductor devices.* John wiley & sons, 2021.

[73] M. E. Franke, T. J. Koplin and U. Simon. "Metal and metal oxide nanoparticles in chemiresistors: does the nanoscale matter?" In: *small* 2.1 (2006), pp. 36–50. DOI: 10.1002/smll.200500261.

[74] H. J. Kim and J.-H. Lee. "Highly sensitive and selective gas sensors using p-type oxide semiconductors: Overview". In: *Sensors and Actuators B* 192 (2014), pp. 607–627. DOI: 10.1016/j.snb.2013.11.005.

[75] N. Chowdhury and B. Bhowmik. "Micro/nanostructured gas sensors: the physics behind the nanostructure growth, sensing and selectivity mechanisms". In: *Nanoscale Advances* 3.1 (2021), pp. 73–93. DOI: 10.1039/D0NA00552E.

[76] E. Comini and G. Sberveglieri. "Metal oxide nanowires as chemical sensors". In: *Materials Today* 13.7-8 (2010), pp. 36–44. DOI: 10.1016/S1369-7021(10)70 126-7.

[77] N. Caicedo, R. Leturcq, J.-P. Raskin, D. Flandre et al. "Detection mechanism in highly sensitive ZnO nanowires network gas sensors". In: *Sensors and Actuators B: Chemical* 297 (2019), p. 126602. DOI: 10.1016/j.snb.2019.05.079.

[78] F. Hernandez-Ramirez, J. D. Prades, A. Tarancon, S. Barth et al. "Insight into the role of oxygen diffusion in the sensing mechanisms of SnO2 nanowires". In: *Advanced Functional Materials* 18.19 (2008), pp. 2990–2994. DOI: 10.1002/adf m.200701191.

[79] *Engineering ToolBox, (2003). Air - Composition and Molecular Weight.* URL: htt ps://www.engineeringtoolbox.com/air-composition-d_212.html (visited on 01/11/2024).

[80] P. Shankar and J. B. B. Rayappan. "Gas sensing mechanism of metal oxides: The role of ambient atmosphere, type of semiconductor and gases-A review". In: *Sci. Lett. J* 4.4 (2015), p. 126.

[81] D. Kohl. "Surface processes in the detection of reducing gases with SnO2-based devices". In: *Sensors and actuators* 18.1 (1989), pp. 71–113. DOI: `10.1016/0250-6874(89)87026-X`.

[82] C. Mattiuzzi and G. Lippi. "Worldwide epidemiology of carbon monoxide poisoning". In: *Human & experimental toxicology* 39.4 (2020), pp. 387–392. DOI: `10.1177/0960327119891214`.

[83] A. Fort, M. Mugnaini, S. Rocchi, V. Vignoli et al. "Metal-oxide nanowire sensors for CO detection: Characterization and modeling". In: *Sensors and Actuators B: Chemical* 148.1 (2010), pp. 283–291. DOI: `10.1016/j.snb.2010.04.034`.

[84] S. Hahn, N. Barsan, U. Weimar, S. Ejakov et al. "CO sensing with SnO2 thick film sensors: role of oxygen and water vapour". In: *Thin Solid Films* 436.1 (2003), pp. 17–24. DOI: `10.1016/S0040-6090(03)00520-0`.

[85] National Institute for Occupational Safety and Health (NIOSH). *Hydrogen Sulfide*. URL: `https://www.cdc.gov/niosh/topics/hydrogensulfide/default.html`.

[86] D. Glass. "A review of the health effects of hydrogen sulphide exposure". In: *The Annals of occupational hygiene* 34.3 (1990), pp. 323–327. DOI: `10.1093/annhyg/34.3.323`.

[87] G. E. Patil, D. Kajale, D. Chavan, N. Pawar et al. "Synthesis, characterization and gas sensing performance of SnO2 thin films prepared by spray pyrolysis". In: *Bulletin of Materials Science* 34.1 (2011), pp. 1–9. DOI: `10.1007/s12034-011-0045-0`.

[88] The European Parliament and of the Council of the European Union. "Directive 2004/42/CE of the European Parliament and of the Council of 21 April 2004 on the limitation of emissions of volatile organic compounds due to the use of organic solvents in certain paints and varnishes and vehicle refinishing products and amending Directive 1999/13/EC". In: *Official Journal* L 143 (21st Apr. 2004), pp. 0087–0096.

[89] A. Guenther, C. Hewitt, D. Erickson, R. Fall et al. "A global model of natural volatile organic compound emissions". In: *J. Geophys. Res* 100.5 (), p. 8873. DOI: `10.1029/94JD02950`.

[90] O. B. Radu, M. van den Berg, Z. Klimont, S. Deetman et al. "Exploring synergies between climate and air quality policies using long-term global and regional emission scenarios". In: *Atmospheric Environment* 140 (2016), pp. 577–591. DOI: `10.1016/j.atmosenv.2016.05.021`.

[91] K. Rumchev, H. Brown and J. Spickett. "Volatile organic compounds: do they present a risk to our health?" In: *Reviews on environmental health* 22.1 (2007), pp. 39–56. DOI: `10.1515/REVEH.2007.22.1.39`.

[92]   "Sensirion Datasheet SGP40". In: `https://sensirion.com/media/docum
        ents/296373BB/6203C5DF/Sensirion_Gas_Sensors_Datasheet_SGP
        40.pdf`.

[93]   "Membrapor Volatile Organic Compounds Gas Sensor VOC/M-20 Specification
        Sheet". In: `https://www.membrapor.ch/sheet/Volatile-Organic-Co
        mpound-Gas-Sensor-VOC-M-20.pdf`.

[94]   C. A. Gärtner, A. C. van Veen and J. A. Lercher. "Oxidative dehydrogenation
        of ethane: common principles and mechanistic aspects". In: *ChemCatChem* 5.11
        (2013), pp. 3196–3217. DOI: `10.1002/cctc.201200966`.

[95]   S. Peng, W. Chen, L. Jin, L. Xu et al. "Pt-doped SnO2 nanoflower gas sensor
        detection characteristic for hydrocarbon gases dissolved in transformer oil". In:
        *2016 IEEE International Conference on High Voltage Engineering and Application
        (ICHVE)*. IEEE. 2016, pp. 1–4. DOI: `10.1109/ICHVE.2016.7800893`.

[96]   M. Carotta, V. Guidi, G. Martinelli, M. Nagliati et al. "Sensing of volatile alkanes
        by metal-oxide semiconductors". In: *Sensors and Actuators B: Chemical* 130.1
        (2008), pp. 497–501. DOI: `10.1016/j.snb.2007.09.053`.

[97]   X. Wang, M. Zhao, F. Liu, J. Jia et al. "C2H2 gas sensor based on Ni-doped ZnO
        electrospun nanofibers". In: *Ceramics International* 39.3 (2013), pp. 2883–2887.
        DOI: `10.1016/j.ceramint.2012.09.062`.

[98]   D. X. Ho, K. H. Kim, J. Ryeul Sohn, Y. Hee Oh et al. "Emission rates of volatile
        organic compounds released from newly produced household furniture products
        using a large-scale chamber testing method". In: *The Scientific World Journal*
        11.1 (2011), pp. 1597–1622. DOI: `10.1100/2011/650624`.

[99]   The National Institute for Occupational Safety and Health (NIOSH). *Toluene.*
        URL: `https://www.cdc.gov/niosh/topics/toluene/default.html`.

[100]   N. L. W. Septiani, B. Yuliarto and H. K. Dipojono. "Multiwalled carbon nanotubes–
        zinc oxide nanocomposites as low temperature toluene gas sensor". In: *Applied
        Physics A* 123 (2017), pp. 1–9. DOI: `10.1007/s00339-017-0803-y`.

[101]   X. Liu, X. Duan, C. Zhang, P. Hou et al. "Improvement toluene detection of
        gas sensors based on flower-like porous indium oxide nanosheets". In: *Journal of
        Alloys and Compounds* 897 (2022), p. 163222. DOI: `10.1016/j.jallcom.202
        1.163222`.

[102]   S. S. David, S. Veeralakshmi, J. Sandhya, S. Nehru et al. "Room temperature
        operatable high sensitive toluene gas sensor using chemiresistive Ag/Bi2O3 nano-
        composite". In: *Sensors and Actuators B: Chemical* 320 (2020), p. 128410. DOI:
        `10.1016/j.snb.2020.128410`.

[103]   K. Karuppasamy, B. Sharma, D. Vikraman, E.-B. Jo et al. "Switchable pn gas
        response for 3D-hierarchical NiFe2O4 porous microspheres for highly selective and
        sensitive toluene gas sensors". In: *Journal of Alloys and Compounds* 886 (2021),
        p. 161281. DOI: `10.1016/j.jallcom.2021.161281`.

[104]   A. Kolmakov. "Some recent trends in the fabrication, functionalisation and characterisation of metal oxide nanowire gas sensors". In: *International journal of nanotechnology* 5.4-5 (2008), pp. 450–474. DOI: `10.1504/IJNT.2008.017447`.

[105]   E. Comini. "Metal oxides nanowires chemical/gas sensors: recent advances". In: *Materials Today Advances* 7 (2020), p. 100099. DOI: `10.1016/j.mtadv.2020.100099`.

[106]   R. G. Hobbs, N. Petkov and J. D. Holmes. "Semiconductor nanowire fabrication by bottom-up and top-down paradigms". In: *Chemistry of Materials* 24.11 (2012), pp. 1975–1991. DOI: `10.1021/cm300570n`.

[107]   N. Ramgir, N. Datta, M. Kaur, S. Kailasaganapathi et al. "Metal oxide nanowires for chemiresistive gas sensors: Issues, challenges and prospects". In: *Colloids and Surfaces A: Physicochemical and Engineering Aspects* 439 (2013), pp. 101–116. DOI: `10.1016/j.colsurfa.2013.02.029`.

[108]   E. Comini, C. Baratto, G. Faglia, M. Ferroni et al. "Quasi-one dimensional metal oxide semiconductors: Preparation, characterization and application as chemical sensors". In: *Progress in Materials Science* 54.1 (2009), pp. 1–67. DOI: `10.1016/j.pmatsci.2008.06.003`.

[109]   C. Soldano, E. Comini, C. Baratto, M. Ferroni et al. "Metal Oxides Mono-Dimensional Nanostructures for Gas Sensing and Light Emission". In: *Journal of the American Ceramic Society* 95.3 (2012), pp. 831–850. DOI: `10.1111/j.1551-2916.2011.05056.x`.

[110]   H. Dang, J. Wang and S. Fan. "The synthesis of metal oxide nanowires by directly heating metal samples in appropriate oxygen atmospheres". In: *Nanotechnology* 14.7 (2003), p. 738. DOI: `10.1088/0957-4484/14/7/308`.

[111]   C. Xu, C. H. Woo and S. Shi. "Formation of CuO nanowires on Cu foil". In: *Chemical Physics Letters* 399.1-3 (2004), pp. 62–66. DOI: `10.1016/j.cplett.2004.10.005`.

[112]   S. Steinhauer, E. Brunet, T. Maier, G. Mutinati et al. "Suspended CuO nanowires for ppb level H2S sensing in dry and humid atmosphere". In: *Sensors and Actuators B: Chemical* 186 (2013), pp. 550–556. DOI: `10.1016/j.snb.2013.06.044`.

[113]   D. Malwal and G. Packirisamy. "Synthesis of Inorganic Nanomaterials, Advances and Key Technologies". In: Elsevier, 2018. Chap. Chapter 10 - Recent advances in the synthesis of metal oxide (MO) nanostructures, pp. 255–281. DOI: `10.1016/B978-0-08-101975-7.00010-5`.

[114]   E. Comini, G. Faglia, M. Ferroni, A. Ponzoni et al. "Metal oxide nanowires: Preparation and application in gas sensing". In: *Journal of Molecular Catalysis A: Chemical* 305.1-2 (2009), pp. 170–177. DOI: `10.1016/j.molcata.2009.01.009`.

[115] Z. R. Dai, Z. W. Pan and Z. Wang. "Novel nanostructures of functional oxides synthesized by thermal evaporation". In: *Advanced Functional Materials* 13.1 (2003), pp. 9–24. DOI: `10.1002/adfm.200390013`.

[116] M. Mozetič, U. Cvelbar, M. K. Sunkara and S. Vaddiraju. "A method for the rapid synthesis of large quantities of metal oxide nanowires at low temperatures". In: *Advanced Materials* 17.17 (2005), pp. 2138–2142. DOI: `10.1002/adma.2005 00728`.

[117] P. Nguyen, H. T. Ng, T. Yamada, M. K. Smith et al. "Direct integration of metal oxide nanowire in vertical field-effect transistor". In: *Nano Letters* 4.4 (2004), pp. 651–657. DOI: `10.1021/nl0498536`.

[118] W. Han, P. Kohler-Redlich, F. Ernst and M. Rühle. "Growth and microstructure of Ga2O3 nanorods". In: *Solid state communications* 115.10 (2000), pp. 527–529. DOI: `10.1016/S0038-1098(00)00238-6`.

[119] L. Liu, Y. Zhao, H. Liu, H. Z. Kou et al. "Directed growth of TiO2 nanorods into microspheres". In: *Nanotechnology* 17.20 (2006), p. 5046. DOI: `10.1088/0957-4484/17/20/003`.

[120] Y. Li, G. Meng, L. Zhang and F. Phillipp. "Ordered semiconductor ZnO nanowire arrays and their photoluminescence properties". In: *Applied Physics Letters* 76.15 (2000), pp. 2011–2013. DOI: `10.1063/1.126238`.

[121] Y. Dongliang, G. Chuannan and D. Youwei. "Preparation and characterization of CuO nanowire arrays". In: *Journal of Semiconductors* 30.7 (2009), p. 072003. DOI: `10.1088/1674-4926/30/7/072003`.

[122] H. Cao, X. Qiu, Y. Liang, M. Zhao et al. "Sol-gel synthesis and photoluminescence of p-type semiconductor Cr2O3 nanowires". In: *Applied physics letters* 88.24 (2006), p. 241112. DOI: `10.1063/1.2213204`.

[123] G. Shen, P. C. Chen, K. Ryu and C. Zhou. "Devices and chemical sensing applications of metal oxide nanowires". In: *Journal of Materials Chemistry* 19.7 (2009), pp. 828–839. DOI: `10.1039/B816543B`.

[124] Y. Hu, M. Gu, X. Liu, J. Zhang et al. "Sol-gel template synthesis and characterization of Lu2O3: Eu3+ nanowire arrays". In: *Micromachines* 9.11 (2018), p. 601. DOI: `10.3390/mi9110601`.

[125] G. Du and G. Van Tendeloo. "Cu (OH) 2 nanowires, CuO nanowires and CuO nanobelts". In: *Chemical Physics Letters* 393.1-3 (2004), pp. 64–69. DOI: `10.101 6/j.cplett.2004.06.017`.

[126] Y. Wang, X. Jiang and Y. Xia. "A solution-phase, precursor route to polycrystalline SnO2 nanowires that can be used for gas sensing under ambient conditions". In: *Journal of the American Chemical Society* 125.52 (2003), pp. 16176–16177. DOI: `10.1021/ja037743f`.

[127]   X. C. Song, Y. F. Zheng, E. Yang and Y. Wang. "Large-scale hydrothermal synthesis of WO3 nanowires in the presence of K2SO4". In: *Materials Letters* 61.18 (2007), pp. 3904–3908. DOI: 10.1016/j.matlet.2006.12.055.

[128]   Roditi International. "Hydrothermal Growth". In: http://www.roditi.com/SingleCrystal/Quartz/Hydrothermal_Growth.html.

[129]   G. Sun, M. Cao, Y. Wang, C. Hu et al. "Anionic surfactant-assisted hydrothermal synthesis of high-aspect-ratio ZnO nanowires and their photoluminescence property". In: *Materials Letters* 60.21 (2006), pp. 2777–2782. DOI: 10.1016/j.matlet.2006.01.088.

[130]   T. Peng, D. Ke, J. Xiao, L. Wang et al. "Hexagonal phase WO3 nanorods: Hydrothermal preparation, formation mechanism and its photocatalytic O2 production under visible-light irradiation". In: *Journal of Solid State Chemistry* 194 (2012), pp. 250–256. DOI: 10.1016/j.jssc.2012.05.016.

[131]   T. Ishizaki, N. Saito and O. Takai. "Surfactant-assisted fabrication of tin oxide nanowires through one-step electrochemically induced chemical deposition". In: *Journal of the Electrochemical Society* 156.10 (2009), p. D413. DOI: 10.1149/1.3190161.

[132]   A. M. Tantray and M. Shah. "Photo electrochemical ability of dense and aligned ZnO nanowire arrays fabricated through electrochemical anodization". In: *Chemical Physics Letters* 747 (2020), p. 137346. DOI: 10.1016/j.cplett.2020.137346.

[133]   J. Miao, M. Miyauchi, T. J. Simmons, J. S. Dordick et al. "Electrospinning of nanomaterials and applications in electronic components and devices". In: *Journal of nanoscience and nanotechnology* 10.9 (2010), pp. 5507–5519. DOI: 10.1166/jnn.2010.3073.

[134]   S. Chuangchote, T. Sagawa and S. Yoshikawa. "Electrospun TiO2 nanowires for hybrid photovoltaic cells". In: *Journal of Materials Research* 26.17 (2011), pp. 2316–2321. DOI: 10.1557/jmr.2011.167.

[135]   D. Li, Y. Wang and Y. Xia. "Electrospinning of polymeric and ceramic nanofibers as uniaxially aligned arrays". In: *Nano letters* 3.8 (2003), pp. 1167–1171. DOI: 10.1021/nl0344256.

[136]   M. Kwiat, S. Cohen, A. Pevzner and F. Patolsky. "Large-scale ordered 1D-nanomaterials arrays: Assembly or not?" In: *Nano Today* 8.6 (2013), pp. 677–694. DOI: 10.1016/j.nantod.2013.12.001.

[137]   Y. Xia, J. A. Rogers, K. E. Paul and G. M. Whitesides. "Unconventional methods for fabricating and patterning nanostructures". In: *Chemical reviews* 99.7 (1999), pp. 1823–1848. DOI: 10.1021/cr980002q.

[138]   B. Su, Y. Wu and L. Jiang. "The art of aligning one-dimensional (1D) nanostructures". In: *Chemical Society Reviews* 41.23 (2012), pp. 7832–7856. DOI: 10.1039/C2CS35187K.

[139] C. Jia, Z. Lin, Y. Huang and X. Duan. "Nanowire electronics: from nanoscale to macroscale". In: *Chemical reviews* 119.15 (2019), pp. 9074–9135. DOI: 10.1021/acs.chemrev.9b00164.

[140] M. Liu, Z. Wu, W. M. Lau and J. Yang. "Recent advances in directed assembly of nanowires or nanotubes". In: *Nano-Micro Letters* 4.3 (2012), pp. 142–153. DOI: 10.1007/BF03353705.

[141] Y. Shan and S. J. Fonash. "Self-assembling silicon nanowires for device applications using the nanochannel-guided "grow-in-place" approach". In: *ACS nano* 2.3 (2008), pp. 429–434. DOI: 10.1021/nn700232q.

[142] Y. Qin, R. Yang and Z. L. Wang. "Growth of horizonatal ZnO nanowire arrays on any substrate". In: *The Journal of Physical Chemistry C* 112.48 (2008), pp. 18734–18736. DOI: 10.1021/jp808869j.

[143] D. Tsivion, M. Schvartzman, R. Popovitz-Biro and E. Joselevich. "Guided growth of horizontal ZnO nanowires with controlled orientations on flat and faceted sapphire surfaces". In: *ACS nano* 6.7 (2012), pp. 6433–6445. DOI: 10.1021/nn3020695.

[144] M. Schvartzman, D. Tsivion, D. Mahalu, O. Raslin et al. "Self-integration of nanowires into circuits via guided growth". In: *Proceedings of the National Academy of Sciences* 110.38 (2013), pp. 15195–15200. DOI: 10.1073/pnas.1306426110.

[145] S. H. Choi, G. Ankonina, D. Y. Youn, S. G. Oh et al. "Hollow ZnO nanofibers fabricated using electrospun polymer templates and their electronic transport properties". In: *ACS nano* 3.9 (2009), pp. 2623–2631. DOI: 10.1021/nn900126k.

[146] S. J. Choi, L. Persano, A. Camposeo, J. S. Jang et al. "Electrospun nanostructures for high performance chemiresistive and optical sensors". In: *Macromolecular Materials and Engineering* 302.8 (2017), p. 1600569. DOI: 10.1002/mame.201600569.

[147] I. S. Hwang, Y. S. Kim, S. J. Kim, B. K. Ju et al. "A facile fabrication of semiconductor nanowires gas sensor using PDMS patterning and solution deposition". In: *Sensors and Actuators B: Chemical* 136.1 (2009), pp. 224–229. DOI: 10.1016/j.snb.2008.10.042.

[148] S. Papazoglou, Y. Raptis, S. Chatzandroulis and I. Zergioti. "A study on the pulsed laser printing of liquid-phase exfoliated graphene for organic electronics". In: *Applied Physics A* 117.1 (2014), pp. 301–306. DOI: 10.1007/s00339-014-8260-3.

[149] S. Papazoglou, V. Tsouti, S. Chatzandroulis and I. Zergioti. "Direct laser printing of graphene oxide for resistive chemosensors". In: *Optics & Laser Technology* 82 (2016), pp. 163–169. DOI: 10.1016/j.optlastec.2016.03.009.

[150] T. Tokuno, M. Nogi, M. Karakawa, J. Jiu et al. "Fabrication of silver nanowire transparent electrodes at room temperature". In: *Nano research* 4.12 (2011), pp. 1215–1222. DOI: 10.1007/s12274-011-0172-3.

[151] I. Pasternak, A. Krajewska, K. Grodecki, I. Jozwik-Biala et al. "Graphene films transfer using marker-frame method". In: *Aip Advances* 4.9 (2014), p. 097133. DOI: `10.1063/1.4896411`.

[152] J. J. Dumond, K. A. Mahabadi, Y. S. Yee, C. Tan et al. "High resolution UV roll-to-roll nanoimprinting of resin moulds and subsequent replication via thermal nanoimprint lithography". In: *Nanotechnology* 23.48 (2012), p. 485310. DOI: `10.1088/0957-4484/23/48/485310`.

[153] E. Menard, R. G. Nuzzo and J. A. Rogers. "Bendable single crystal silicon thin film transistors formed by printing on plastic substrates". In: *Applied Physics Letters* 86.9 (2005), p. 093507. DOI: `10.1063/1.1866637`.

[154] R. S. Dahiya, A. Adami, C. Collini and L. Lorenzelli. "Fabrication of single crystal silicon micro-/nanostructures and transferring them to flexible substrates". In: *Microelectronic Engineering* 98 (2012), pp. 502–507. DOI: `10.1016/j.mee.2012.07.084`.

[155] S. Khan, R. S. Dahiya and L. Lorenzelli. "Flexible thermoelectric generator based on transfer printed Si microwires". In: *2014 44th European Solid State Device Research Conference (ESSDERC)*. IEEE. 2014, pp. 86–89. DOI: `10.1109/ESSDERC.2014.6948764`.

[156] V. Logeeswaran, A. M. Katzenmeyer and M. S. Islam. "Harvesting and transferring vertical pillar arrays of single-crystal semiconductor devices to arbitrary substrates". In: *IEEE Transactions on Electron Devices* 57.8 (2010), pp. 1856–1864. DOI: `10.1109/TED.2010.2051195`.

[157] M. C. McAlpine, H. Ahmad, D. Wang and J. R. Heath. "Highly ordered nanowire arrays on plastic substrates for ultrasensitive flexible chemical sensors". In: *Nature materials* 6.5 (2007), pp. 379–384. DOI: `10.1038/nmat1891`.

[158] L. Liao, J. Bai, Y. C. Lin, Y. Qu et al. "High-Performance Top-Gated Graphene-Nanoribbon Transistors Using Zirconium Oxide Nanowires as High-Dielectric-Constant Gate Dielectrics". In: *Advanced Materials* 22.17 (2010), pp. 1941–1945. DOI: `10.1002/adma.200904415`.

[159] B. Rezania, M. Dorn, N. Severin and J. Rabe. "Influence of graphene exfoliation on the properties of water-containing adlayers visualized by graphenes and scanning force microscopy". In: *Journal of colloid and interface science* 407 (2013), pp. 500–504. DOI: `10.1016/j.jcis.2013.06.034`.

[160] J. D. Caldwell, T. J. Anderson, J. C. Culbertson, G. G. Jernigan et al. "Technique for the dry transfer of epitaxial graphene onto arbitrary substrates". In: *ACS nano* 4.2 (2010), pp. 1108–1114. DOI: `10.1021/nn901585p`.

[161] R. Dahiya, G. Gottardi and N. Laidani. "PDMS residues-free micro/macrostructures on flexible substrates". In: *Microelectronic Engineering* 136 (2015), pp. 57–62. DOI: `10.1016/j.mee.2015.04.037`.

134

[162] K. N. Lee, S. W. Jung, W. H. Kim, M. H. Lee et al. "Well controlled assembly of silicon nanowires by nanowire transfer method". In: *Nanotechnology* 18.44 (2007), p. 445302. DOI: 10.1088/0957-4484/18/44/445302.

[163] X. Li, Y. Zhu, W. Cai, M. Borysiak et al. "Transfer of large-area graphene films for high-performance transparent conductive electrodes". In: *Nano letters* 9.12 (2009), pp. 4359–4363. DOI: 10.1021/nl902623y.

[164] J. Lee, P. Lee, H. Lee, D. Lee et al. "Very long Ag nanowire synthesis and its application in a highly transparent, conductive and flexible metal electrode touch panel". In: *Nanoscale* 4.20 (2012), pp. 6408–6414. DOI: 10.1039/C2NR31254A.

[165] A. R. Madaria, A. Kumar, F. N. Ishikawa and C. Zhou. "Uniform, highly conductive, and patterned transparent films of a percolating silver nanowire network on rigid and flexible substrates using a dry transfer technique". In: *Nano Research* 3.8 (2010), pp. 564–573. DOI: 10.1007/s12274-010-0017-5.

[166] H. Li, J. Wu, X. Huang, Z. Yin et al. "A universal, rapid method for clean transfer of nanostructures onto various substrates". In: *ACS nano* 8.7 (2014), pp. 6563–6570. DOI: 10.1021/nn501779y.

[167] M. E. Reimer, G. Bulgarini, N. Akopian, M. Hocevar et al. "Bright single-photon sources in bottom-up tailored nanowires". In: *Nature communications* 3.1 (2012), pp. 1–6. DOI: 10.1038/ncomms1746.

[168] J. W. Suk, A. Kitt, C. W. Magnuson, Y. Hao et al. "Transfer of CVD-grown monolayer graphene onto arbitrary substrates". In: *ACS nano* 5.9 (2011), pp. 6916–6924. DOI: 10.1021/nn201207c.

[169] J. K. Hwang, S. Cho, J. M. Dang, E. B. Kwak et al. "Direct nanoprinting by liquid-bridge-mediated nanotransfer moulding". In: *Nature nanotechnology* 5.10 (2010), p. 742. DOI: 10.1038/nnano.2010.175.

[170] I. N. Kholmanov, C. W. Magnuson, A. E. Aliev, H. Li et al. "Improved electrical conductivity of graphene films integrated with metal nanowires". In: *Nano letters* 12.11 (2012), pp. 5679–5683. DOI: 10.1021/nl302870x.

[171] D. Lee, H. Lee, Y. Ahn, Y. Jeong et al. "Highly stable and flexible silver nanowire–graphene hybrid transparent conducting electrodes for emerging optoelectronic devices". In: *Nanoscale* 5.17 (2013), pp. 7750–7755. DOI: 10.1039/C3NR02320F.

[172] K. Du, I. Wathuthanthri, W. Mao, W. Xu et al. "Large-area pattern transfer of metallic nanostructures on glass substrates via interference lithography". In: *Nanotechnology* 22.28 (2011), p. 285306. DOI: 10.1088/0957-4484/22/28/285306.

[173] S. Bae, H. Kim, Y. Lee, X. Xu et al. "Roll-to-roll production of 30-inch graphene films for transparent electrodes". In: *Nature nanotechnology* 5.8 (2010), pp. 574–578. DOI: 10.1038/nnano.2010.132.

[174] H. W. Kang, J. Yeo, J. O. Hwang, S. Hong et al. "Simple ZnO nanowires patterned growth by microcontact printing for high performance field emission device". In: *The Journal of Physical Chemistry C* 115.23 (2011), pp. 11435–11441. DOI: 10.1 021/jp2019044.

[175] D. Qin, Y. Xia and G. M. Whitesides. "Soft lithography for micro-and nanoscale patterning". In: *Nature protocols* 5.3 (2010), pp. 491–502. DOI: 10.1038/nprot .2009.234.

[176] D. G. Choi, K. J. Lee and J. Y. Kim. "Nanotransfer molding of free-standing nanowire and porous nanomembranes suspended on microtrenches". In: *ACS applied materials & interfaces* 5.2 (2013), pp. 418–424. DOI: 10.1021/am30249 3x.

[177] Z. Fan, J. C. Ho, Z. A. Jacobson, R. Yerushalmi et al. "Wafer-scale assembly of highly ordered semiconductor nanowire arrays by contact printing". In: *Nano letters* 8.1 (2008), pp. 20–25. DOI: 10.1021/nl071626r.

[178] X. Liang, B. A. Sperling, I. Calizo, G. Cheng et al. "Toward clean and crackless transfer of graphene". In: *ACS nano* 5.11 (2011), pp. 9144–9153. DOI: 10.1021 /nn203377t.

[179] S. Xiao, J. Tang, T. Beetz, X. Guo et al. "Transferring self-assembled, nanoscale cables into electrical devices". In: *Journal of the American Chemical Society* 128.33 (2006), pp. 10700–10701. DOI: 10.1021/ja0642360.

[180] N. A. Melosh, A. Boukai, F. Diana, B. Gerardot et al. "Ultrahigh-density nanowire lattices and circuits". In: *Science* 300.5616 (2003), pp. 112–115. DOI: 10.1126/s cience.1081940.

[181] J. Krainer, M. Deluca, E. Lackner, R. Wimmer-Teubenbacher et al. "CMOS integrated tungsten oxide nanowire networks for ppb-level H2S sensing". In: *Procedia Engineering* 168 (2016), pp. 272–275. DOI: 10.1016/j.proeng.2016 .11.189.

[182] J. Choi, Y. J. Kim, S. U. Son, Y. M. Kim et al. "Electrostatic Induced Inkjet Printing System for Micro Patterning and Drop-On-Demand Jetting Characteristics". In: 2008.

[183] D. Wang, R. Zhu, Z. Zhou and X. Ye. "Controlled assembly of zinc oxide nanowires using dielectrophoresis". In: *Applied physics letters* 90.10 (2007), p. 103110. DOI: 10.1063/1.2711756.

[184] Y. Huang, X. Duan, Q. Wei and C. M. Lieber. "Directed Assembly of One-Dimensional Nanostructures into Functional Networks". In: *Science* 291.5504 (2001), pp. 630–633. DOI: 10.1126/science.291.5504.630.

[185] G. Yu, A. Cao and C. M. Lieber. "Large-area blown bubble films of aligned nanowires and carbon nanotubes". In: *Nature nanotechnology* 2.6 (2007), pp. 372–377. DOI: 10.1038/nnano.2007.150.

[186] S. Wu, K. Huang, E. Shi, W. Xu et al. "Soluble polymer-based, blown bubble assembly of single-and double-layer nanowires with shape control". In: *Acs Nano* 8.4 (2014), pp. 3522–3530. DOI: 10.1021/nn406610d.

[187] D. Whang, S. Jin, Y. Wu and C. M. Lieber. "Large-scale hierarchical organization of nanowire arrays for integrated nanosystems". In: *Nano letters* 3.9 (2003), pp. 1255–1259. DOI: 10.1021/nl0345062.

[188] C. Baratto, V. Golovanova, G. Faglia, H. Hakola et al. "On the alignment of ZnO nanowires by Langmuir–Blodgett technique for sensing application". In: *Applied Surface Science* 528 (2020), p. 146959. DOI: 10.1016/j.apsusc.2020.146959.

[189] Y. Wang, X. Wu, Y. Li and Z. Zhou. "Mesostructured SnO2 as sensing material for gas sensors". In: *Solid-State Electronics* 48.5 (2004), pp. 627–632. DOI: 10.1016/j.sse.2003.09.015.

[190] K. S. Novoselov, A. K. Geim, S. V. Morozov, D.-e. Jiang et al. "Electric field effect in atomically thin carbon films". In: *science* 306.5696 (2004), pp. 666–669. DOI: 10.1126/science.1102896.

[191] A. Javey, S. Nam, R. S. Friedman, H. Yan et al. "Layer-by-layer assembly of nanowires for three-dimensional, multifunctional electronics". In: *Nano letters* 7.3 (2007), pp. 773–777. DOI: 10.1021/nl063056l.

[192] J. Yao, H. Yan and C. M. Lieber. "A nanoscale combing technique for the large-scale assembly of highly aligned nanowires". In: *Nature nanotechnology* 8.5 (2013), pp. 329–335. DOI: 10.1038/nnano.2013.55.

[193] R. Yerushalmi, Z. A. Jacobson, J. C. Ho, Z. Fan et al. "Large scale, highly ordered assembly of nanowire parallel arrays by differential roll printing". In: *Applied Physics Letters* 91.20 (2007), p. 203104. DOI: 10.1063/1.2813618.

[194] A. S. Zoolfakar, R. A. Rani, A. J. Morfa, A. P. O'Mullane et al. "Nanostructured copper oxide semiconductors: a perspective on materials, synthesis methods and applications". In: *journal of materials chemistry c* 2.27 (2014), pp. 5247–5270. DOI: 10.1039/C4TC00345D.

[195] Q. Zhang, K. Zhang, D. Xu, G. Yang et al. "CuO nanostructures: synthesis, characterization, growth mechanisms, fundamental properties, and applications". In: *Progress in Materials Science* 60 (2014), pp. 208–337. DOI: 10.1016/j.pmatsci.2013.09.003.

[196] C. Yang, X. Su, F. Xiao, J. Jian et al. "Gas sensing properties of CuO nanorods synthesized by a microwave-assisted hydrothermal method". In: *Sensors and Actuators B: Chemical* 158.1 (2011), pp. 299–303. DOI: 10.1016/j.snb.2011.06.024.

[197] N. Ekthammathat, T. Thongtem and S. Thongtem. "Antimicrobial activities of CuO films deposited on Cu foils by solution chemistry". In: *Applied Surface Science* 277 (2013), pp. 211–217. DOI: 10.1016/j.apsusc.2013.04.027.

137

[198] J. C. Park, J. Kim, H. Kwon and H. Song. "Gram-scale synthesis of Cu2O nanocubes and subsequent oxidation to CuO hollow nanostructures for lithium-ion battery anode materials". In: *Advanced Materials* 21.7 (2009), pp. 803–807. DOI: 10.1002/adma.200800596.

[199] S. Anandan, X. Wen and S. Yang. "Room temperature growth of CuO nanorod arrays on copper and their application as a cathode in dye-sensitized solar cells". In: *Materials Chemistry and Physics* 93.1 (2005), pp. 35–40. DOI: 10.1016/j.matchemphys.2005.02.002.

[200] M. P. Neupane, Y. K. Kim, I. S. Park, K. A. Kim et al. "Temperature driven morphological changes of hydrothermally prepared copper oxide nanoparticles". In: *Surface and Interface Analysis: An International Journal devoted to the development and application of techniques for the analysis of surfaces, interfaces and thin films* 41.3 (2009), pp. 259–263. DOI: 10.1002/sia.3009.

[201] M. Cao, C. Hu, Y. Wang, Y. Guo et al. "A controllable synthetic route to Cu, Cu 2 O, and CuO nanotubes and nanorods". In: *Chemical Communications* 15 (2003), pp. 1884–1885. DOI: 10.1039/B304505F.

[202] M. Dar, Y. Kim, W. Kim, J. Sohn et al. "Structural and magnetic properties of CuO nanoneedles synthesized by hydrothermal method". In: *Applied Surface Science* 254.22 (2008), pp. 7477–7481. DOI: 10.1016/j.apsusc.2008.06.004.

[203] R. Srivastava, M. A. Prathap and R. Kore. "Morphologically controlled synthesis of copper oxides and their catalytic applications in the synthesis of propargylamine and oxidative degradation of methylene blue". In: *Colloids and Surfaces A: Physicochemical and Engineering Aspects* 392.1 (2011), pp. 271–282. DOI: 10.1016/j.colsurfa.2011.10.004.

[204] G. Filipič and U. Cvelbar. "Copper oxide nanowires: a review of growth". In: *Nanotechnology* 23 (2012), p. 194001. DOI: 10.1088/0957-4484/23/19/194001.

[205] X. Jiang, T. Herricks and Y. Xia. "CuO nanowires can be synthesized by heating copper substrates in air". In: *Nano letters* 2.12 (2002), pp. 1333–1338. DOI: 10.1021/nl0257519.

[206] B. Ganga, M. R. Varma and P. Santhosh. "Evidence of reduced antiferromagnetic transition in mesocrystals of CuO synthesized by a surfactant-free solution phase method". In: *CrystEngComm* 17.37 (2015), pp. 7086–7093. DOI: 10.1039/C5CE00928F.

[207] P. H. Shih, C. L. Cheng and S. Y. Wu. "Short-range spin-phonon coupling in in-plane CuO nanowires: a low-temperature Raman investigation". In: *Nanoscale Research Letters* 8.1 (2013), pp. 1–6. DOI: 10.1186/1556-276X-8-398.

[208] Y. Kong, Y. Li, X. Cui, L. Su et al. "SnO2 nanostructured materials used as gas sensors for the detection of hazardous and flammable gases: a review". In: *Nano Materials Science* (2021). DOI: 10.1016/j.nanoms.2021.05.006.

138

[209] L. V. Thong, L. T. N. Loan and N. V. Hieu. "Comparative study of gas sensor performance of SnO2 nanowires and their hierarchical nanostructures". In: *Sensors and Actuators B: Chemical* 150.1 (2010), pp. 112–119. DOI: 10.1016/j.snb.2010.07.033.

[210] S. Ding, J. S. Chen and X. W. Lou. "One-Dimensional Hierarchical Structures Composed of Novel Metal Oxide Nanosheets on a Carbon Nanotube Backbone and Their Lithium-Storage Properties". In: *Advanced Functional Materials* 21.21 (2011), pp. 4120–4125. DOI: 10.1002/adfm.201100781.

[211] S. Gubbala, V. Chakrapani, V. Kumar and M. K. Sunkara. "Band-edge engineered hybrid structures for dye-sensitized solar cells based on SnO2 nanowires". In: *Advanced Functional Materials* 18.16 (2008), pp. 2411–2418. DOI: 10.1002/adfm.200800099.

[212] Y. Han, X. Wu, Y. Ma, L. Gong et al. "Porous SnO 2 nanowire bundles for photocatalyst and Li ion battery applications". In: *CrystEngComm* 13.10 (2011), pp. 3506–3510. DOI: 10.1039/C1CE05171G.

[213] H. Wang and A. L. Rogach. "Hierarchical SnO2 nanostructures: recent advances in design, synthesis, and applications". In: *Chemistry of Materials* 26.1 (2014), pp. 123–133. DOI: 10.1021/cm4018248.

[214] D. F. Zhang, L. D. Sun, J. L. Yin and C. H. Yan. "Low-temperature fabrication of highly crystalline SnO2 nanorods". In: *Advanced materials* 15.12 (2003), pp. 1022–1025. DOI: 10.1002/adma.200304899.

[215] Z. W. Pan, Z. R. Dai and Z. L. Wang. "Nanobelts of semiconducting oxides". In: *Science* 291.5510 (2001), pp. 1947–1949. DOI: 10.1126/science.1058120.

[216] Y. Wang, H. C. Zeng and J. Y. Lee. "Highly reversible lithium storage in porous SnO2 nanotubes with coaxially grown carbon nanotube overlayers". In: *Advanced Materials* 18.5 (2006), pp. 645–649. DOI: 10.1002/adma.200501883.

[217] D. Bullett. "Bulk and surface electron states in WO3 and tungsten bronzes". In: *Journal of Physics C: Solid State Physics* 16.11 (1983), p. 2197. DOI: 10.1088/0022-3719/16/11/022.

[218] G. D. Rieck. "Tungsten oxides". In: *Tungsten and its compounds*. Pergamon Press, 1967, pp. 93–97.

[219] A. Ponzoni, E. Comini, M. Ferroni and G. Sberveglieri. "Nanostructured WO3 deposited by modified thermal evaporation for gas-sensing applications". In: *Thin Solid Films* 490.1 (2005), pp. 81–85. DOI: 10.1016/j.tsf.2005.04.031.

[220] J. Liu, M. Zhong, J. Li, A. Pan et al. "Few-layer WO3 nanosheets for high-performance UV - photodetectors". In: *Materials Letters* 148 (2015), pp. 184–187. DOI: 10.1016/j.matlet.2015.02.088.

[221] R. M. Fernández-Domene, R. Sánchez-Tovar, B. Lucas-Granados, G. Roselló-Márquez et al. "A simple method to fabricate high-performance nanostructured WO3 photocatalysts with adjusted morphology in the presence of complexing agents". In: *Materials & Design* 116 (2017), pp. 160–170. DOI: 10.1016/j.matdes.2016.12.016.

[222] Z. Jiao, X. W. Sun, J. Wang, L. Ke et al. "Hydrothermally grown nanostructured WO3 films and their electrochromic characteristics". In: *Journal of Physics D: Applied Physics* 43.28 (2010), p. 285501. DOI: 10.1088/0022-3727/43/28/285501.

[223] Z. Gu, T. Zhai, B. Gao, X. Sheng et al. "Controllable assembly of WO3 nanorods/nanowires into hierarchical nanostructures". In: *The Journal of Physical Chemistry B* 110.47 (2006), pp. 23829–23836. DOI: 10.1021/jp065170y.

[224] K. Huang, Q. Pan, F. Yang, S. Ni et al. "Controllable synthesis of hexagonal WO3 nanostructures and their application in lithium batteries". In: *Journal of Physics D: Applied Physics* 41.15 (2008), p. 155417. DOI: 10.1088/0022-3727/41/15/155417.

[225] M. Farhadian, P. Sangpour and G. Hosseinzadeh. "Morphology dependent photocatalytic activity of WO3 nanostructures". In: *Journal of Energy Chemistry* 24.2 (2015), pp. 171–177. DOI: 10.1016/S2095-4956(15)60297-2.

[226] DI J. Krainer. "Fabrication of CMOS Integrated Gas Sensor Devices Based on Tungsten Oxide Nanowires". PhD thesis. Technischen Universität Graz, 2017.

[227] W. S. Hanoosh and E. M. Abdelrazaq. "Polydimethyl siloxane toughened epoxy resins: tensile strength and dynamic mechanical analysis". In: *Malaysian Polymer Journal* 4.2 (2009), pp. 52–61.

[228] F. Sosada-Ludwikowska, R. Wimmer-Teubenbacher, M. Sagmeister and A. Köck. "Transfer Printing Technology as a Straightforward Method to Fabricate Chemical Sensors Based on Tin Dioxide Nanowires". In: *Sensors* 19.14 (2019), p. 3049. DOI: 10.3390/s19143049.

[229] V. Leitgeb, K. Fladischer, F. Hitzel, F. Sosada-Ludwikowska et al. "SPM-SEM Investigations of Semiconductor Nanowires for Integrated Metal Oxide Gas Sensors". In: *Multidisciplinary Digital Publishing Institute Proceedings* 2.13 (2018), p. 701. DOI: 10.3390/proceedings2130701.

[230] A. Köck, R. Wimmer-Teubenbacher, F. Sosada-Ludwikovska, K. Rohracher et al. "3D-integrated multi-sensor demonstrator system for environmental monitoring". In: *2019 20th International Conference on Solid-State Sensors, Actuators and Microsystems & Eurosensors XXXIII (TRANSDUCERS & EUROSENSORS XXXIII)*. IEEE. 2019, pp. 1136–1139. DOI: 10.1109/TRANSDUCERS.2019.8808418.

[231] C. J. Belle and U. Simon. "Combinatorial approaches for synthesis of metal oxides: processing and sensing application". In: *Metal oxide nanomaterials for chemical sensors*. Ed. by M. A. Carpenter, S. Mathur and A. Kolmakov. Springer, 2012, pp. 117–166.

[232] S. Batterman and C. Peng. "TVOC and CO2 concentrations as indicators in indoor air quality studies". In: *American Industrial Hygiene Association Journal* 56.1 (1995), pp. 55–65. DOI: 10.1080/15428119591017321.

[233] T. Kida, T. Kuroiwa, M. Yuasa, K. Shimanoe et al. "Study on the response and recovery properties of semiconductor gas sensors using a high-speed gas-switching system". In: *Sensors and Actuators B: Chemical* 134.2 (2008), pp. 928–933. DOI: 10.1016/j.snb.2008.06.044.

[234] G. Domènech-Gil, J. Samà, C. Fàbrega, I. Gràcia et al. "Highly sensitive SnO2 nanowire network gas sensors". In: *Sensors and Actuators B: Chemical* 383 (2023), p. 133545. DOI: 10.1016/j.snb.2023.133545.

[235] N. D. Hoa, P. Van Tong, N. Van Duy, T. Dao et al. "Effective decoration of Pd nanoparticles on the surface of SnO2 nanowires for enhancement of CO gas-sensing performance". In: *Journal of hazardous materials* 265 (2014), pp. 124–132. DOI: 10.1016/j.jhazmat.2013.11.054.

[236] V. Kumar, S. Sen, K. Muthe, N. Gaur et al. "Copper doped SnO2 nanowires as highly sensitive H2S gas sensor". In: *Sensors and Actuators B: Chemical* 138.2 (2009), pp. 587–590. DOI: 10.1016/j.snb.2009.02.053.

[237] J. Ma, Y. Liu, H. Zhang, P. Ai et al. "Room temperature ppb level H2S detection of a single Sb-doped SnO2 nanoribbon device". In: *Sensors and Actuators B: Chemical* 216 (2015), pp. 72–79. DOI: 10.1016/j.snb.2015.04.025.

[238] R. Wimmer-Teubenbacher, F. Sosada-Ludwikowska, B. Zaragoza Travieso, S. Defregger et al. "CuO thin films functionalized with gold nanoparticles for conductometric carbon dioxide gas sensing". In: *Chemosensors* 6.4 (2018), p. 56. DOI: 10.3390/chemosensors6040056.

APPENDIX A

Response and recovery times

The response times and recovery times were calculated for the following sensors:

- 2 SB gas sensors based on SnO_2 nanowires (manual transfer) towards CO at 300° - Table A.1

- 2 SB gas sensors based on WO_3 nanowires (manual transfer) towards CO at 250°C - Table A.2

- 3 SB gas sensors based on SnO_2 nanowires (manual transfer) towards H_2S at 350°C - Table A.3

- 1 SB gas sensor based on WO_3 nanowires (manual transfer) towards H_2S at 400°C - Table A.4

- 2 APPS gas sensors based on SnO_2 nanowires (manual transfer) towards CO at 350° - Table A.5

- 1 APPS gas sensor 1A based on SnO_2 nanowires (manual transfer) towards CO at 350° with time difference of 2 years - Table A.6

- 3 APPS gas sensors (transferred manually - S1A and transferred with a bonder - S2A and S2C) based on SnO_2 nanowires towards CO at 350° - Table A.7

- 2 APPS gas sensors based on SnO_2 nanowires (manual transfer) towards HCMix at 350° - Table A.8

- 2 APPS gas sensors based on SnO_2 nanowires (manual transfer) towards toluene at 350° - Table A.9

- 2 APPS gas sensors based on SnO_2 nanowires (manual transfer) towards H_2S at 350° - Table A.10

- 3 MPW4 gas sensors based on SnO_2 nanowires (bonder-based transfer with a structured PDMS stamp) towards CO and HCMix at 350° - Table A.11

gas concentration [ppm]	50% rH						25% rH		
	10	30	60	100	150	200	10	30	60
S1 response time [s]	-	11	23	14	151	62	23	35	59
S1 recovery time [s]	-	65	120	141	140	152	36	116	111
S2 response time [s]	-	14	18	23	153	137	26	45	75
S2 recovery time [s]	-	17	97	145	121	186	27	105	169

gas concentration [ppm]	25% rH			75% rH					
	100	150	200	10	30	60	100	150	200
S1 response time [s]	74	72	100	-	21	42	23	24	48
S1 recovery time [s]	175	234	229	-	18	89	70	157	93
S2 response time [s]	104	175	164	-	10	15	23	27	201
S2 recovery time [s]	255	290	415	-	18	43	185	230	328

Table A.1: Response and recovery times for two SB gas sensors based on SnO_2 nanowires towards CO at 300°.

gas concentration [ppm]	50% rH						25% rH		
	10	30	60	100	150	200	10	30	60
S1 response time [s]	263	108	156	113	235	179	-	249	70
S1 recovery time [s]	8	321	164	368	340	326	-	11	372
S2 response time [s]	11	5	10	11	21	25	-	10	18
S2 recovery time [s]	60	9	18	27	44	46	-	52	47

gas concentration [ppm]	25% rH			75% rH					
	100	150	200	10	30	60	100	150	200
S1 response time [s]	188	82	182	8	137	115	116	166	168
S1 recovery time [s]	52	65	205	28	87	97	201	235	155
S2 response time [s]	29	62	92	-	6	8	8	13	22
S2 recovery time [s]	91	62	155	-	6	19	22	28	39

Table A.2: Response and recovery times for two SB gas sensors based on WO_3 nanowires towards CO at 250°C.

	50% rH			25% rH			75% rH		
gas concentration [ppb]	10	100	1000	10	100	1000	10	100	1000
S1 - D1 response time [s]	25	8	9	24	9	19	22	8	33
S1 - D1 recovery time [s]	42	32	216	34	32	114	60	31	378
S2 - E1 response time [s]	36	10	10	34	11	14	38	11	27
S2 - E1 recovery time [s]	53	49	390	53	58	187	58	79	180
S3 - E2 response time [s]	27	9	30	27	11	260	22	11	275
S3 - E2 recovery time [s]	40	46	173	35	60	136	40	59	61

Table A.3: Response and recovery times for three SB gas sensors based on SnO_2 nanowires towards H_2S at 350°C.

	50% rH			25% rH			75% rH		
gas concentration [ppb]	200	500	1000	200	500	1000	200	500	1000
S1 response time [s]	266	69	21	255	68	24	252	65	23
S1 recovery time [s]	425	234	229	292	229	234	279	222	220

Table A.4: Response and recovery times for SB gas sensor based on WO_3 nanowires towards H_2S at 400°C.

	50% rH						25% rH		
gas concentration [ppm]	10	30	60	100	150	200	10	30	60
S1A response time [s]	29	17	17	18	27	14	42	24	14
S1A recovery time [s]	20	37	69	53	50	43	134	39	29
S1B response time [s]	45	16	16	14	14	17	37	23	18
S1B recovery time [s]	73	36	49	55	46	48	26	40	34

	25% rH			75% rH					
gas concentration [ppm]	100	150	200	10	30	60	100	150	200
S1A response time [s]	20	22	21	17	20	6	8	13	11
S1A recovery time [s]	45	53	49	11	19	33	36	47	41
S1B response time [s]	15	22	22	15	10	17	12	13	15
S1B recovery time [s]	44	52	55	6	25	39	37	47	45

Table A.5: Response and recovery times for two APPS gas sensors based on SnO_2 nanowires towards CO at 350°.

	50% rH						25% rH		
gas concentration [ppm]	10	30	60	100	150	200	10	30	60
S1A - 2018 response time [s]	29	17	17	18	27	14	42	24	14
S1A - 2018 recovery time [s]	20	37	69	53	50	43	134	39	29
S1A - 2020 response time [s]	108	44	74	68	63	71	69	47	74
S1A - 2020 recovery time [s]	58	85	359	127	187	261	26	137	205

	25% rH			75% rH					
gas concentration [ppm]	100	150	200	10	30	60	100	150	200
S1A - 2018 response time [s]	20	22	21	17	20	6	8	13	11
S1A - 2018 recovery time [s]	45	53	49	11	19	33	36	47	41
S1A - 2020 response time [s]	68	67	71	46	60	71	107	77	59
S1A - 2020 recovery time [s]	193	186	249	34	78	206	131	111	198

Table A.6: Response and recovery times for APPS gas sensor 1A based on SnO_2 nanowires towards CO at 350° with time difference of 2 years.

	50% rH						25% rH		
gas concentration [ppm]	10	30	60	100	150	200	10	30	60
S1A response time [s]	108	44	74	68	63	71	69	47	74
S1A recovery time [s]	58	85	359	127	187	261	26	137	205
S2A response time [s]	26	20	38	117	43	69	27	18	25
S2A recovery time [s]	234	49	49	49	45	54	24	28	42
S2C response time [s]	3	12	15	20	15	19	33	16	37
S2C recovery time [s]	2	24	25	43	31	23	50	25	27

	25% rH			75% rH					
gas concentration [ppm]	100	150	200	10	30	60	100	150	200
S1A response time [s]	68	67	71	46	60	71	107	77	59
S1A recovery time [s]	193	186	249	34	78	206	131	111	198
S2A response time [s]	47	32	51	73	25	50	39	38	42
S2A recovery time [s]	49	58	51	79	39	66	59	59	120
S2C response time [s]	13	27	34	19	25	19	39	18	25
S2C recovery time [s]	26	32	36	20	22	21	36	22	34

Table A.7: Response and recovery times for three APPS gas sensors (transferred manually - S1A and transferred with a bonder - S2A and S2C) based on SnO_2 nanowires towards CO at 350°.

	50% rH					25% rH				
gas concentration [ppm]	1	5	10	50	100	1	5	10	50	100
S1A response time [s]	-	26	31	17	26	36	85	56	48	23
S1A recovery time [s]	-	30	29	44	62	22	33	27	54	55
S1B response time [s]	50	37	24	15	19	78	74	44	19	23
S1B recovery time [s]	27	19	25	44	55	51	31	37	46	71

	75% rH				
gas concentration [ppm]	1	5	10	50	100
S1A response time [s]	17	52	21	20	21
S1A recovery time [s]	12	89	21	30	50
S1B response time [s]	13	50	35	16	18
S1B recovery time [s]	10	33	23	37	48

Table A.8: Response and recovery times for two APPS gas sensors based on SnO_2 nanowires towards HCMix at 350°.

	50% rH			25% rH			75% rH		
gas concentration [ppm]	0.5	1	5	0.5	1	5	0.5	1	5
S1A response time [s]	-	10	108	13	-	44	15	128	89
S1A recovery time [s]	-	18	267	7	-	80	44	223	146
S1B response time [s]	7	19	32	42	27	87	5	4	42
S1B recovery time [s]	13	29	54	43	49	84	10	17	56

Table A.9: Response and recovery times for two APPS gas sensors based on SnO_2 nanowires towards toluene at 350°.

	50% rH			25% rH			75% rH		
gas concentration [ppm]	0.01	0.1	1	0.01	0.1	1	0.01	0.1	1
S1A response time [s]	-	-	13	-	4	25	2	4	23
S1A recovery time [s]	-	-	23	-	55	61	5	5	20
S1B response time [s]	-	8	22	47	44	23	-	2	21
S1B recovery time [s]	-	2	102	7	>300	96	-	17	57

Table A.10: Response and recovery times for two APPS gas sensors based on SnO_2 nanowires towards H_2S at 350°.

50 ppm CO	50% rH	25% rH	75% rH
S1A response time [s]	230	55	21
S1A recovery time [s]	72	41	46
S5B response time [s]	191	34	15
S5B recovery time [s]	61	81	26
S6B response time [s]	187	31	15
S6B recovery time [s]	128	87	29

10 ppm HCMix	50% rH	25% rH	75% rH
S1A	230	103	41
S1A	267	>300	>300
S5B	270	99	90
S5B	51	>300	>300
S6B	245	72	46
S6B	>300	>300	>300

Table A.11: Response and recovery times for three MPW4 gas sensors based on SnO_2 nanowires towards 50 ppm CO and 10 ppm HCMix at 350°.

Florentyna Lidia Sosada-Ludwikowska

✉ **Email:** florentyna.sosada-ludwikowska@mcl.at

Nationality: Polish

WORK EXPERIENCE

[01/09/2015 – Current] **PhD student**

Materials Center Leoben Forschung GmbH

City: Leoben | **Country:** Austria

Work on the implementation of metal oxide nanowires on CMOS-based micro-hotplate chips

Parental leave July 2021-January 2023

[15/07/2014 – 31/07/2014] **Intern in "Nanochemistry" group**

Max Planck Institut für Festkörperforschung

City: Stuttgart | **Country:** Germany

Nanochemistry group - prof. Bettina V. Lotsch

[11/2012 – 01/2013] **Internship**

Institute of Physics, Polish Academy of Sciences

City: Warsaw | **Country:** Poland

Group of MBE Growth of Nitride Nanostructures - prof. Żytkiewicz

[09/2011 – 10/2011] **Chemistry Laboratorian**

Faculty of Chemistry University of Warsaw

Country: Poland

Laboratory of Stereocontrolled Organic Synthesis - dr Piotr Kwiatkowski

EDUCATION AND TRAINING

[03/2016 – Current] **PhD studies, Faculty of Electrical Engineering and IT**

TU Wien

Country: Austria |

[04/2014 – 07/2014] **Exchange semester abroad - ERASMUS**

Ludwig-Maximilians-Universität München

Country: Germany |

[10/2013 – 08/2015] **Master degree, Nanostructure Engineering**

University of Warsaw, Faculty of Physics & Faculty of Chemistry

Country: Poland |

[10/2010 – 09/2013] **Bachelor degree, Nanostructure engineering**

University of Warsaw, Faculty of Physics & Faculty of Chemistry

Country: Poland |

PUBLICATIONS

[2024]

Development of a Screening Platform for Optimizing Chemical Nanosensor Materials

Reference: Sensors, 24(17), 5565

Egger, L., Reiner, L., Sosada-Ludwikowska, F., Köck, A., Schlicke, H., Becker, S., ... & Tscherner, M.

OT5. 156-Novel chemical sensor device enabled by simultaneous thermal-optical excitation

Reference: Lectures, 121-122

Sosada-Ludwikowska, F., Egger, L., Köck, A., Casals, O., & Prades, D. J.

Adjusting surface coverage of Pt nanocatalyst decoration for selectivity control in CMOS-integrated SnO2 thin film gas sensors

Reference: Nanoscale Advances, 6(4), 1127-1134

Sosada-Ludwikowska, F., Reiner, L., Egger, L., Lackner, E., Krainer, J., Wimmer-Teubenbacher, R., ... & Koeck, A.

[2022]

Efficient Screening of Hybrid Nanomaterials for Optimizing Chemical Sensor Devices

Reference: Engineering Proceedings, 21(1), 30

Egger, L., Reiner, L., Sosada-Ludwikowska, F., Köck, A., Niehaus, J. S., Becker, S., ... & Tscherner, M.

[2021]

AlN FBAR particle sensor with a thermophoretic sampling mechanism

Reference: IEEE Sensors Journal, 21(17), 19427-19435

Specht, J. P., Esfahani, S., Tan, T. H., Sosada-Ludwikowska, F., Wimmer-Teubenbacher, R., Köck, A., Cole, M., & Gardner, J. W.

Optimization of SnO2-Based CMOS-integrated gas sensors by mono-, bi-and trimetallic nanoparticles

Reference: Multidisciplinary Digital Publishing Institute Proceedings, 56(1), 43

Wimmer-Teubenbacher, R., Sosada-Ludwikowska, F., Köck, A., Steinhauer, S., Sowwan, M., & Singh, V.

Controllable Transfer of MOx Nanowires on Microhotplate-Based Gas Sensing Devices

Reference: Electrochemical Society Meeting Abstracts 239 (No. 56, pp. 1466-1466)

Sosada-Ludwikowska, F., Wimmer-Teubenbacher, R., & Köck, A.

[2020]

Atomic-scale structure and chemical sensing application of ultrasmall size-selected Pt nanoparticles supported on SnO2

Reference: Materials Advances, 1(9), 3200-3207

Steinhauer, S., Lackner, E., Sosada-Ludwikowska, F., Singh, V., Krainer, J., Wimmer-Teubenbacher, R., ... & Sowwan, M.

[2019]

Transfer Printing Technology as a Straightforward Method to Fabricate Chemical Sensors Based on Tin Dioxide Nanowires

Reference: Sensors (Basel, Switzerland), 19(14), 3049. doi:10.3390/s19143049

Sosada-Ludwikowska, F., Wimmer-Teubenbacher, R., Sagmeister, M., & Köck, A.

Heterogeneous Integration of Metal Oxides—Towards a CMOS Based Multi Gas Sensor Device

Reference: Multidisciplinary Digital Publishing Institute Proceedings, 14(1), 5

Köck, A., Deluca, M., Sosada-Ludwikowska, F., Maier, G., Teubenbacher, R. W., Sagmeister, M., ... & Tscherner, M.

Study of CuO nanowire growth on different copper surfaces

Reference: Scientific reports, 9(1), 1-13

Fritz-Popovski, G., Sosada-Ludwikowska, F., Köck, A., Keckes, J., & Maier, G. A.

[2018]   **A new device for high-temperature in situ GISAXS measurements**

Reference: Review of Scientific Instruments, 89(3), 035103

Fritz-Popovski, G., Bodner, S. C., Sosada-Ludwikowska, F., Maier, G. A., Morak, R., Chitu, L., ... & Paris, O.

CuO thin films functionalized with gold nanoparticles for conductometric carbon dioxide gas sensing

Reference: Chemosensors, 6(4), 56

Wimmer-Teubenbacher, R., Sosada-Ludwikowska, F., Zaragoza Travieso, B., Defregger, S., Tokmak, O., Niehaus, J. S., Deluca, M., & Köck, A.

Reflectance and fast polarization dynamics of a GaN/Si nanowire ensemble

Reference: Journal of Physics: Condensed Matter, 30(31), 315301

Korona, K. P., Zytkiewicz, Z. R., Sobanska, M., Sosada, F. E., Dróżdż, P. A., Klosek, K., & Tchutchulashvili, G.

SPM—SEM Investigations of Semiconductor Nanowires for Integrated Metal Oxide Gas Sensors

Reference: Multidisciplinary Digital Publishing Institute Proceedings, 2(13), 701

Leitgeb, V., Fladischer, K., Hitzel, F., Sosada-Ludwikowska, F., Krainer, J., Wimmer-Teubenbacher, R., & Köck, A.

Multifunctional Nanoparticles-Key for Optimizing Chemical Nanosensors

Reference: 2018 12th International Conference on ASDAM (pp. 1-5). IEEE

Kock, A., Deluca, M., Sosada-Ludwikowska, F., Wimmer-Teubenbacher, R., Lackner, E., Rohracher, K., ... & Singh, V

Transfer Printing Technology for Fabricating Chemical Sensors Based on Tin Dioxide Nanowires

Reference: Multidisciplinary Digital Publishing Institute Proceedings, 2(13), 1076

Sosada-Ludwikowska, F., Wimmer-Teubenbacher, R., & Köck, A.

Dry transfer print process of SnO2 nanowires for gas sensor manufacturing

Reference: Proceedings IMCS 2018, 647-648

Sosada-Ludwikowska, F., Wimmer-Teubenbacher, R., & Köck, A.